REPAIR/STRENGTHENING OF STEEL ANGLES USING THERMAL SPRAY METALLIZING

by

CHUEN SHIONG LEONG

A Thesis
Submitted to the Faculty of Graduate Studies
In Partial Fulfillment of the
Requirements for the Degree of

MASTER OF SCIENCE

Structural Engineering Division
Department of Civil & Geological Engineering
University of Manitoba
Winnipeg, Manitoba
Canada

THE UNIVERSITY OF MANITOBA

FACULTY OF GRADUATE STUDIES

*****

COPYRIGHT PERMISSION PAGE

Repair/Strengthening of Steel Angles Using Thermal Spray Metallizing

BY

Chuen Shiong Leong

A Thesis/Practicum submitted to the Faculty of Graduate Studies of The University of Manitoba in partial fulfillment of the requirements of the degree of Master of Science

ABSTRACT

Corrosion of steel structures has been a serious problem in civil engineering for years. Repairing such structures is becoming increasingly important to maintain the integrity of corroded structures for public safety. In recent years, many studies have been conducted on the use of thermal spray metallizing coatings on metallic substrates. This technique is widely used for corrosion and wearing protection. In this research program, the effectiveness of the thermal spray metallizing technique was examined as a means of repairing corroded steel structures. The spray material used to replace the corroded material on steel sections was produced through the thermal spray process.

Determining the mechanical properties of thick spray coatings was a fundamental prerequisite in evaluating the effectiveness of this technique. Spray materials included Zinc, Aluminum, $Zn^{85}Al^{15}$ alloy, 10-carbon steel (CSA standard W48.4-1978, class E70s-6) and 40-carbon steel applied on a series of specimens which were tested under static tension and compression. Based on the results from these tests, 10-carbon steel and 40-carbon steel were selected as the repair materials for defective steel angles. Two sets of seven L76x76x4.8 steel angle specimens were repaired and tested under static compression. In addition, seven steel plate specimens repaired with 10-carbon steel were tested in tension. The 10-carbon steel performed better and improved the strength of repaired specimens in compression compared to 40-carbon steel. Although the repair material exhibited low tensile and bond strengths, they improved the compressive

buckling strength of repaired specimens by 89% to 97%. However, steel plates repaired with 10-carbon steel showed no improvement in strength under tension. In addition, to the experimental work, extensive theoretical analysis using the finite element program ANSYS was also conducted. The finite element results agreed well with the experimental results.

ACKNOWLEDGEMENTS

The author would like to express his sincere and profound gratitude to his supervisor Dr. Dimos Polyzois for his valuable support, encouragement, advice and excellent guidance throughout this project. Technical support was provided by Q-Concepts Incorporated. Funding was provided through an NSERC operating grant.

The author also wishes to acknowledge the support provided by Dr. Sherif Hassan, a Post-Doctoral Fellow. Further, the author would like to express his appreciation to Dr. John Frye and Dr. John Cahoon for serving as his examining committee. Special thanks go to Mr. Scott Sparrow and Mr. Moray McVey for their technical assistance during the experimental work.

The author wishes to express his sincerest gratitude to his fiancee Chang Xiang and his family for their love, understanding, support, and devotion during the course of the study.

TABLE OF CONTENTS

CHAPTER 4: TEST RESULTS

CHAPTER 5: FINITE ELEMENT MODELING

LIST OF TABLES

CHAPTER 3

CHAPTER 4

CHAPTER 5

LIST OF FIGURES

CHAPTER 2

CHAPTER 3

CHAPTER 4

CHAPTER 5

CHAPTER 1

INTRODUCTION

1.1 General

Corrosion of steel structures has been a serious problem in civil engineering for years. Repairing such structures is becoming increasingly important to maintain the integrity of steel structures for public safety. In recent years, many studies have been conducted on the use of thermal spray metallizing coatings, mainly, for corrosion protection and machinery repair. No studies have been conducted on the use of thick thermal sprayed material for the repair of steel members.

This thesis reports the results from an investigation at the University of Manitoba, Canada, to determine the applicability of this technique in repairing steel structural members that have been extensively corroded. A series of tests was carried out on both coated and uncoated specimens tested under static loading. The wire-arc-spray technique was used for all thermal metallizing applications in this research program. This technique generally produces higher bond strength and denser spray material than other techniques [2]. The spray coating applied on all test specimens was prepared by Q-Concepts Incorporated of Winnipeg, Manitoba.

1.2 Objectives and Scope

The main objective of this research program was to determine if thermal spray metallizing technique can be used to repair corroded steel members. An experimental program was carried out to investigate the strength improvement of repaired steel angle sections which had been artificially damaged to simulate mass loss due to corrosion. The specimens were repaired using the thermal spray metallizing technique.

The specific objectives were to:

1) Select appropriate spray materials by testing a series of standard tension and compression coupons.

2) Investigate the performance of repaired steel angles under static compression and repaired steel plates under static tension.

3) Develop a finite element model using the ANSYS software program to predict the strength capacity of repaired sections.

This thesis is divided into six chapters. The first chapter covers the introduction and the objectives of the research program. An overview of the history and application of thermal spray metallizing in engineering systems is given in Chapter 2. The formation of thermal spray coatings, the characteristics of thin spray coatings, and the techniques and processes used in thermal spraying are also presented in this chapter. The details of the

experimental program, including coupon testing and testing of steel specimens under static loading are given in Chapter 3. Test results and the analysis of the repaired materials are presented in Chapter 4. A finite element model developed using the ANSYS program is given in Chapter 5. This analysis is based on the material properties obtained in the testing of standard coupons. Finally, a summary of the research program along with a set of conclusions resulting from the experimental and analytical work and a number of recommendations for further research are provided in Chapter 6.

CHAPTER 2

LITERATURE REVIEW

2.1 History of the Thermal Spray Metallizing Technique

Dr. M. U. Schoop of Zurich, Switzerland developed the Thermal Spray Metallizing technique in 1910. He started by feeding molten metallic material into a high-pressured gas stream to form a spraying mechanism. Later, he developed the flame spray using the heat produced from flame combustion to melt the metallic powder materials and sprayed it with the compressed air. At that time, this technique was not popular for coating applications because the method of generating the required heat as well as the compressed air were not convenient using the conventional technology of the day. Two years later, he developed the first flame spray equipment that was able to spray both powder and wire materials to produce a spray coating. This process was called the "Schoop Process" for many years after the development of the technique.

Schoop and his partners sold the patent for thermal spray metallizing to Germany where the first commercial spray equipment was manufactured. The patent was later sold to France. In the early 1920s, thermal spray equipment units were sold to most of the

countries in Europe and to the United States. In the early years after the development of the flame spray system, the thermal spray metallizing technique was not widely practiced in the industry. Many thermal spray coatings were produced for the primary purpose of experimental studies. The advantages of thermal spray coatings were not well understood and were limited in industrial application. In the mid-1930s, there were approximately 30 metallizing companies throughout North America which aggressively promoted the advantages of thermal spray coating [1].

2.2 Thermal Spray Process

The thermal spray is a process of producing a metallic coating developed from the deposition of molten material on a prepared substrate. The schematic diagram of the general thermal spray process is shown in Figure 2-1 [2]. Two types of feedstock are available for use in the thermal spray process, powder and wire. All spray materials whether in powder or wire form can be sprayed as long as the material has a lower melting temperature than the temperature produced in a spray system, and its properties do not change in the molten state. Feedstock in the thermal spray process is melted by high temperatures that are generated either from organic fuel combustion or from an electric arc inside the spray equipment. Molten particles are propelled through the nozzle by high-pressured gas streams in the spray gun towards the substrate. The great impact of force transforms the molten particles, which are in liquid state, to thin platelets on the substrate, as shown in Figure 2-2.

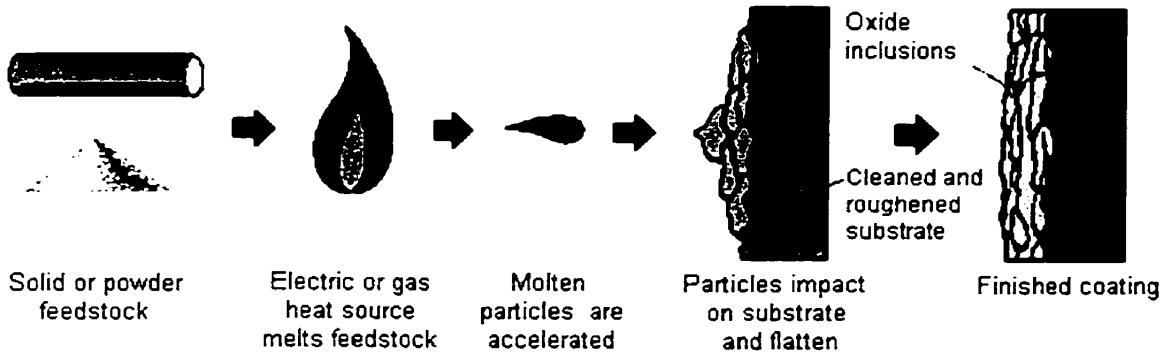

Figure 2-1: Schematic diagram of general thermal spray process [2]

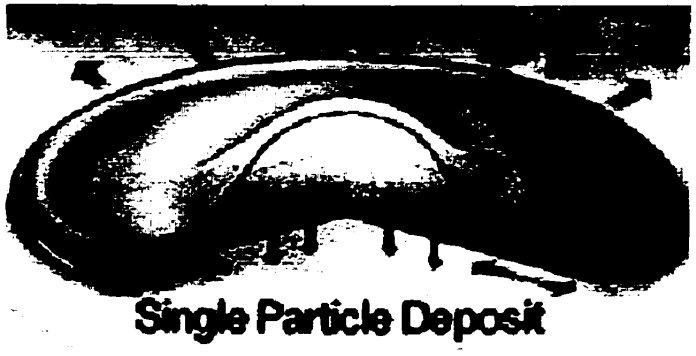

Figure 2-2 : Formation of thin platelet from molten particle due to great impact of force [3]

As the molten droplets impact the surface they deform into a platelet which solidify quickly due to rapid heat dissipation into the substrate. Successive deposition of these platelets results in a thin surface coating. The combination of flow pattern and irregular arrangement of the droplets produce an interlocking mechanism and form the bonding between the particles. In thermal spraying, the coating formation is usually accompanied by residual impurities in the material structures. The spray coating usually consists of four major elements: air voids, oxide inclusions, molten particles, and unmelted particles. The arrangement of typical particles and impurities are shown in Figure 2-3.

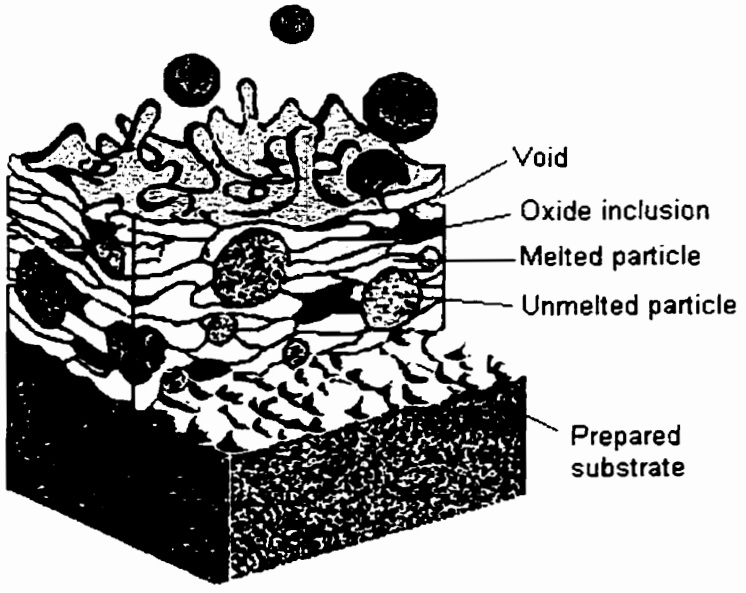

Figure 2-3: Schematic diagram of particle arrangements in thermal spray coating [3]

2.3 Thermal Spray Systems for Coatings

The operation range of temperature and spray velocity from the spray system are two important factors which affect the characteristics of spray coatings [4]. The portability of the spray system is also a crucial issue when considering where the thermal spray work is to be carried out, whether onsite or indoors. The choice of the thermal spray system is usually based on the following factors: (a) the spray area coverage in one pass; (b) the cost effectiveness of the process; (c) the portability of thermal spray system; (d) the mechanical properties of the spray coating; (e) the environmental constraints; and (f) the labor safety [5-6]. Several spray systems are currently available for producing spray coatings according to application requirements. Four of the most popular thermal spray systems are discussed below.

2.3.1 Flame Spray System

Flame spray is the earliest technology that was developed for producing thermal spray coatings and is still one of the most popular spray techniques today. The schematic diagram of the flame spray system is shown in Figure 2-4. The spray material, either in powder or wire form, is fed through the spray gun and melted by high temperatures produced from organic fuel combustion. Fuel gasses such as acetylene, methyl-actylene-propadiene (MPAA), propane, propylene, and natural gas combined with oxygen, are the common gasses used in this system. The molten particles are propelled by the compressed air with great force resulting in an impact on the substrate. Any spray materials that possess melting temperature below 2480 ^{0}C (4500 ^{0}F) can be flame sprayed on a prepared substrate [2].

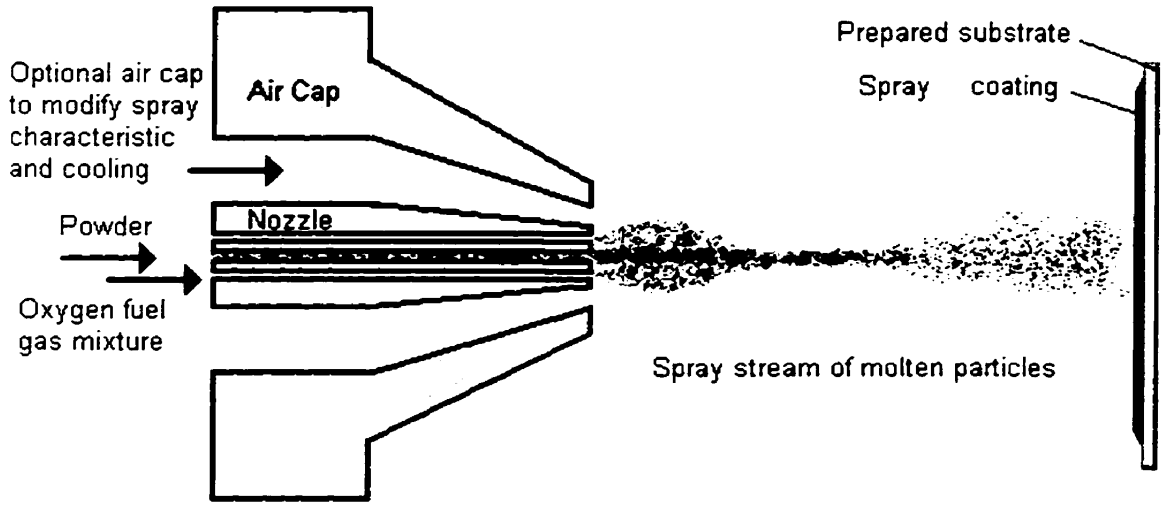

Figure 2-4: Schematic diagram of flame spray system [3]

Flame spray is widely used on site to spray steel members with Zinc, Aluminum, and Zinc-Aluminum alloy materials for corrosion protection coating [2]. In general, the flame spray produces a lower temperature and lower spray velocity compared to other spray systems. This method produces a spray coating with higher porosity and lower bond strength and results in higher heat transmission to the substrate. However, the deposition capability of the flame spray system on the substrate is excellent and is ideal for large spray coverage areas. Unlike the arc spray, the flame spray method can be used not only on metals but also on non-conductive materials. The disadvantages of this system are that the heat transformation is high and the temperature generated by the organic fuel to melt the spray materials is low.

2.3.2 Plasma Spray System

The plasma spray process is basically the same as the flame spray process except that the plasma spray uses electric potential to produce the high temperature required for melting the spray materials. The resistance heating from the electric arc provides an extremely high temperature to ionize gasses in the spray gun to form a plasma. The expanded gasses propel molten particles at a high velocity from the gun nozzle to the substrate. Spray powder is fed to the zone where the highest temperature is produced to melt the material into the liquid state, as shown in Figure 2-5. Inert gasses such as argon and nitrogen, sometimes with additions of hydrogen or helium, are used to control the temperature and velocity of the spray material. The plasma spray gun consists of two electrodes that are composed of tungsten (cathode) and copper (anode). Water that circulates inside the spray gun is used to lower the heat that is generated in the electrodes during the plasma process.

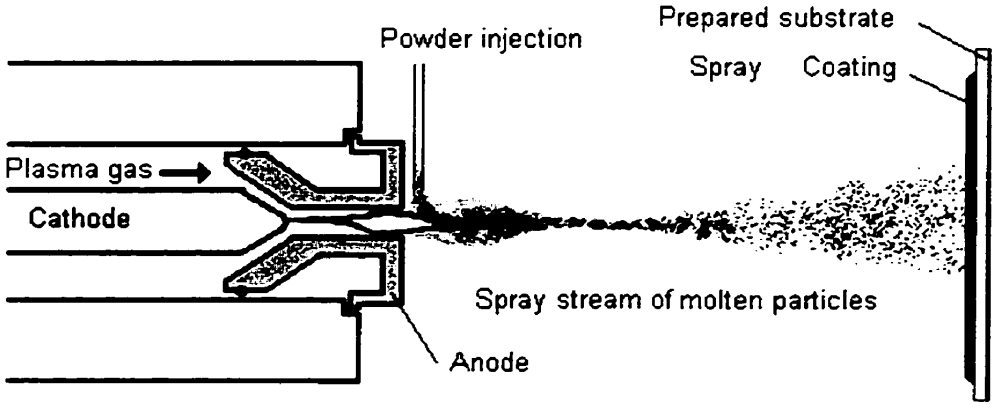

Figure 2-5: Schematic diagram of plasma spray system [3]

Plasma spray can operate in a wide range of spray materials, including metallic and non-metallic powder materials. High temperature (up to 19000 ^{0}C) can be achieved quickly which can melt most of the metallic materials including the refractory oxides and carbides that require temperatures much higher than the flame spray [7]. The plasma spray system provides a better quality coating and produces a dense, clean coating with lower porosity and higher bond strength. This is due to the combination of high velocity produced and the clean-high heat sources. From the aspect of the quality of the coating, the plasma spray is better than the flame spray. However, the feedstock of the plasma spray is restricted to powder form only. In addition, this system is generally more expensive to operate as it is more complex and has higher equipment and maintenance costs.

2.3.3 Wire Arc Spray System

Arc spray is a process that utilizes electric potential to produce enough heat to melt the metallic material in the spray gun. Two metallic wires are used as the electrodes to complete the electric arc, as shown in Figure 2-6. High temperatures (up to 8316 ^{0}C) can be produced by this system to melt most of the metallic materials [7]. The feeding controller is used to adjust the wire feeding rate which affects the thickness and deposition rate of the coating. Molten materials are atomized and propelled by compressed air. The velocity of the particles can reach up to 100m/s towards the substrate surface [7]. Molten particles are rapidly solidified and deposited on the substrate with high impact to form the arc spray coating.

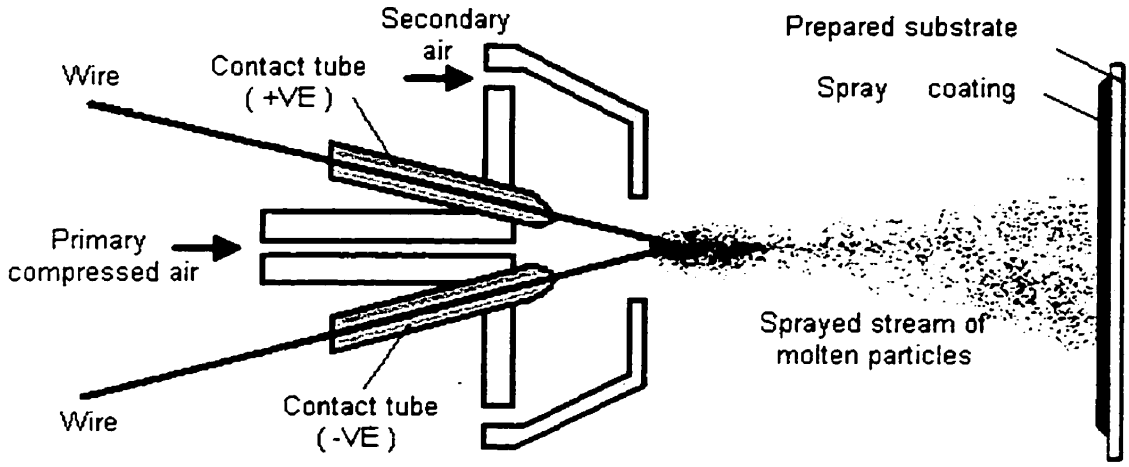

Figure 2-6: Schematic diagram of wire arc spray system [3]

The wire arc spray system is the least expensive system in the thermal spraying process. The low operation cost and the capability of large spray coverage area has made this system the most cost-effective among all the spray systems. Wire-arc-spray coating is generally denser, cleaner, and has a higher bond strength and a lower porosity compared to flame spray coating [8]. This system allows two different material wires to be sprayed together in order to produce an alloy coating. Arc spray provides the least transferred heat on the substrate since the compressed air, travelling with the molten particles, increases the heat dissipation of the molten particles and reduces the heat in the coating and the substrate. Therefore, it is suitable for spraying thick coatings, without any warpage or damage on the substrate material. High corrosion resistance materials such as Zinc, Aluminum, and Zinc-Aluminum alloys are often used for corrosion

protection of steel structures. This system is convenient to employ on site due to its portability. The disadvantage of this system is that the feedstock of the spray system must be electrically conductive and in wire form.

2.3.4 High Velocity Oxygen Fuel (HVOF) System

The high velocity oxygen fuel system is relatively a new system used by the thermal spray industry. This spray concept is similar to the flame spray system except that the heat temperature and velocity are much higher. The spray system has a combustion chamber and a long nozzle for the purpose of generating heat and velocity. Since the system involves flame combustion inside the spray gun, water is circulated between the electrodes in order to reduce the gun temperature. The schematic diagram of the HOVF system is shown in Figure 2-7. Organic fuels such as kerosene, acetylene, propylene and hydrogen are mixed with oxygen in the spray chamber. The gasses and spray powders are mixed and stored in the chamber under high-pressured conditions prior to ignition. Ignition is introduced in the chamber to produce the high temperature required for melting the spray powders. High velocity is achieved from gas expansion through a long and narrow nozzle to propel the molten particles. These conditions produce a spray coating that is extremely dense, and with high bond strength [7]. The powders in this system do not require a fully melted state in the spray process because even the particles that are partially melted have enough kinetic energy for impact to produce platelets on the substrate. This system is normally used when very high density and high bond strength of coating are required. However, a large amount of heat produced from the fuel combustion can be transferred to the substrate material compared

to other spray systems. Also, it is more expansive and more complicated to operate compared to the arc spray system, and it has a small spray coverage area.

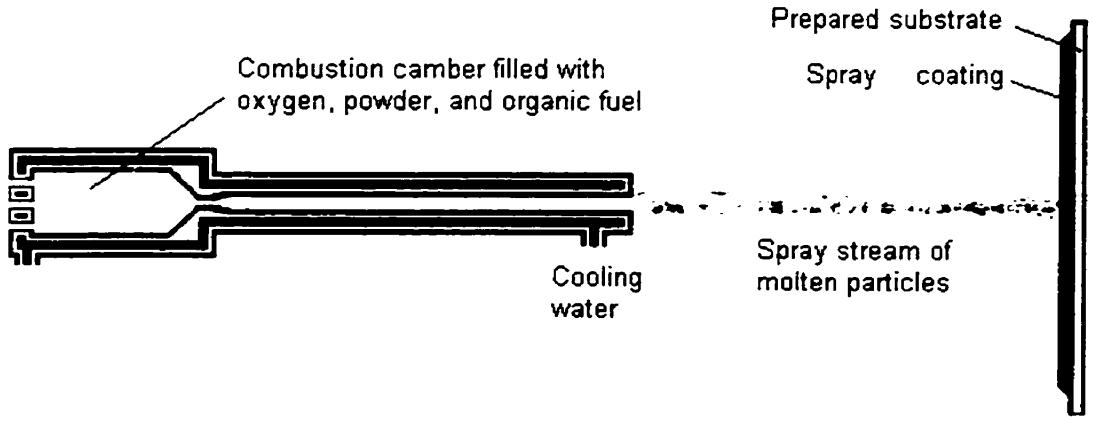

Figure 2-7: Schematic diagram of High Velocity Oxygen Fuel (HVOF) system [3]

2.4 Characteristics of Spray Coatings

Insufficient temperature and too much compressed air during the thermal spray process can lead to the production of unmelted particles. The lack of impact force produced by the spray system makes it difficult to produce plastic flow on molten particles to form the strong bonding between each particle. Molten metallic material, which has high chemical reactivity order, has the tendency to produce metal oxide with the presence of oxygen during the cooling process. The amount of oxide inclusion depends on the spray material properties and the cooling period in the spray process. It is usually formed when molten particles travel from the spray system to the substrate.

Porosity of the spray material is primary due to the air voids trapped inside the spray coating when the velocity of the propelled particles is not high enough to compact the molten particles. The porosity and oxide inclusions play an important role in forming the bond strength. Minimum porosity and oxide inclusion will provide the maximum bond strength in spray coatings.

The thermal spray process alters the particle arrangements within the material and changes the particles' original molecular bonding. The deposition of molten particles generated splat by splat with particles impacting on the previous solidified material, forms layers of coating structures that bond each particle through mechanical interaction (inter-locking) [9]. Therefore, the tensile strength of a spray coating is weaker than the original material. Many studies have been conducted to determine the mechanical properties, such as bond strength [10-11], hardness, and Young's modulus [12], of thin spray coatings. These studies have shown that the material properties of spray coatings are weaker than the original material due to the different molecular arrangement in the two materials. The original material has strong chemical bonding between molecules, whereas, the spray material has only the weak bonding produced primary from mechanical interlocking between the particles.

Residual stresses in the spray coating is an important property that must be considered during application. Bonding between the coating and the substrate can be seriously reduced by the residual stresses which are introduced during the cooling process [13]. Several researchers have pointed out that the residual stresses increase according to

the thickness of the spray material [14]. Shrinkage of molten particles produces compressive stresses in the substrate and tensile stresses in the spray coating. Thick spray coating have larger residual stress and therefore smaller bond strength than thin coatings. Figure 2-8 shows that the combination of compressive and tensile forces will cause warpage on the coating [3]. The free edge effect, where de-bonding of a coating starts from the edges, is produced when the tensile stress in the coating is larger than the bond strength [15]. Other factors that might affect the coating adhesion are the angle of spray, temperature, surface preparation, and deposition rate. Coatings applied at 45^0 have a lower adhesion strength to the surface [16]. The temperature used for melting the material should not be too high because this will increase the residual stresses and transfer large amounts of heat to the substrate. One of the primary advantages of this process is that the heat transferred from the spray system to the substrate material is minimal. Thus, this process is being referred to as the "cold process". This feature avoids the warpage and damage done on the substrate compared to welding and galvanization processes. The spray coating requires no curing period, and can be put into service right after the spraying process. Thermal spray provides better bonding between the coating and the worked piece, and also provides the rough surface for sealing the material.

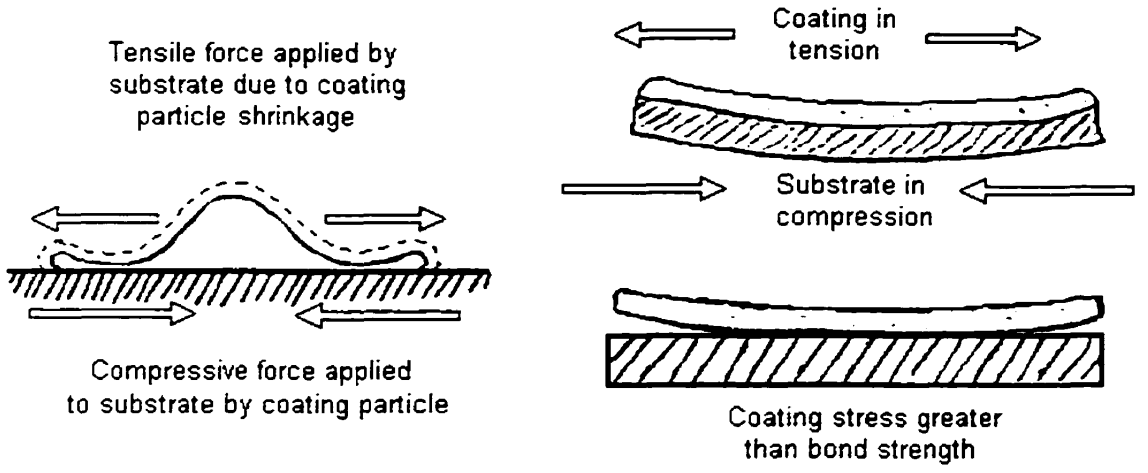

Figure 2-8: Formation of residual stresses on spray coating [3]

2.5 Preparation of Spray Surface

Proper surface preparation is the single most important factor required to produce a good bond between the coating and the substrate. The prepared surface provides the irregular rough surface necessary to develop the interlocking mechanism for the particles. A number of standards and specifications, such the CSA (G189-1966), METCO Flame Spray Handbook, and National Association of Corrosion Engineers (NACE), outline proper procedures for preparing the spray surface [17-19]. In general, there are several techniques that are currently practiced in the thermal spraying industry for surface preparation. They include degreasing, used to clean the substrate when the surface is contaminated by chemical substance, and grit blasting, used to remove the unwanted residual material such as the corroded material and to provide a rough surface for thermal

spraying. Grit blasting provides the best cost effective procedure because it is simple to operate and can be applied to large areas. Rough threading is used to enhance the prepared surface. It consists of machining a thread form pattern on the substrate area to be sprayed and it is frequently used in conjunction with grit blasting on cylindrical surfaces. Bond coat is used as an adhesive agent to produce high bond strength between the coating and the substrate. However, the thermal expansion behavior of bond coat between the spray coating and the substrate should be compatible. A technique called the preheating process is also used where the substrate is preheated before thermal spraying to reduce the shrink differential between the coating and the substrate and to minimize the formation of residual stresses in the coating.

2.6 Applications of the Thermal Spray Coating

Thermal spray metallizing is a popular technique used to produce a thin metallic coating on steel structures for corrosion protection [20]. Research to-date has focused on the performance of spray coatings as corrosion protection agents of steel structures subjected to various types of environmental conditions. Most of the applications of thermal spray metallizing involve offshore structures [21], steel bridges [22-23], commercial ships [24], and pressure vessels [25]. Some studies have also been reported on the use of metallizing for improving the wearing resistance [26], and for the repair of machinery components [27]. Recently, ceramic spray coatings have also been introduced as a thermal barrier coatings and as electric insulation materials.

Thermal spraying for corrosion protection of steel bridges has been practiced since the 1930s [28]. Spray materials such as Zinc, Aluminum, and Zinc-Aluminum alloy are very common for corrosion protection in Europe and North America. A 19-year study on the effect corrosion protection of aluminum and zinc coatings on low carbon steel was completed by the American Welding Society in 1974. The study showed that the life expectancy of the coatings is over 25-30 years if the coatings are applied correctly [29].

Traditionally, welding has been used in field repairs of steel structures. However, the temperature distribution produced during welding affects the material microstructure, hardness, mechanical properties and the residual stresses [30]. These temperatures can seriously deform a steel section and, in the case of loaded structures, can lead to the premature failure during the welding process. Structural distortion during welding has always been a concern to structural engineers. Thermal spray metallizing, on the other hand, produces much lower heat than welding, potentially making it a better repair technique. Furthermore, thermal spray metallizing is a simple process that can easily be adapted to field applications. This technique is especially suitable for the repair of hydroelectric transmission towers and bridges. However, most studies have been focused on the performance of thin spray coatings. Information on the performance of thick spray coatings required in the repair of steel structures is non existent. Also, the performance of steel sections repaired with thermal spray metallizing is still unknown and no analysis has been developed to-date for determining their ultimate strength. The intent of the research investigation reported in this thesis is to examine whether this technique can be

used to repair damaged steel members and eliminate the expensive alternative of member replacement.

CHAPTER 3

EXPERIMENTAL PROGRAM

3.1 Testing Program

The objectives of the testing program were: (a) to investigate the mechanical properties of the spray material, and (b) to investigate the performance of the repaired steel sections. This testing program was divided into four phases. In the first phase, tension tests on standardized specimens were conducted to investigate the tensile properties of thick thermal spray coatings. The second phase involved static compression tests performed to evaluate the compressive properties of thick thermal spray coatings. In the third and fourth phases, steel angle and steel plate specimens with artificial defects simulating mass loss due to corrosion and repaired using the thermal spray metallizing technique were tested in compression and tension respectively to investigate their performance. The details of the test specimens, the test set-up, and the test procedures used are given below.

3.2 Phase 1 - Static Tension Tests on Standard Coupons

A total of 15 standard specimens with and without spray coating were tested under static tension to investigate the tensile properties of the spray materials. Each tension specimen was assigned a specific label, as shown in Figure 3-1. The first term of the label denotes the type of specimen (S = standard coupon). The second term denotes the type of spray material (Zn = Zinc, Al = Aluminum, and $Zn^{85}Al^{15}$ = Zinc Aluminum alloy). The last term indicates the specimen number. Three similar specimens for each type were tested. Some specimens (e.g. S) had no spray coating while other (e.g. S-ZnZn) had no substrate material.

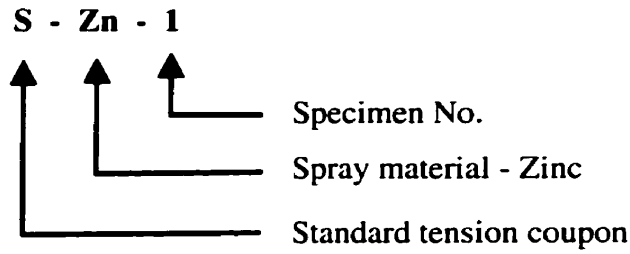

Figure 3-1 : Label of tension specimen

3.2.1 Standard Test Specimens

The specimens that formed the substrate in this phase were fabricated according to ASTM standard (E8M - 93) [31]. A thickness of 5 mm for the tension specimens was used in this phase. The overall specimen length was 220 mm with a gauge length of 50

mm. Figure 3-2 shows a tension specimen with detailed dimensions. The legends used in Figure 3-2 are listed in Table 3-1. The type of specimens in this phase are summarized in the Table 3-2.

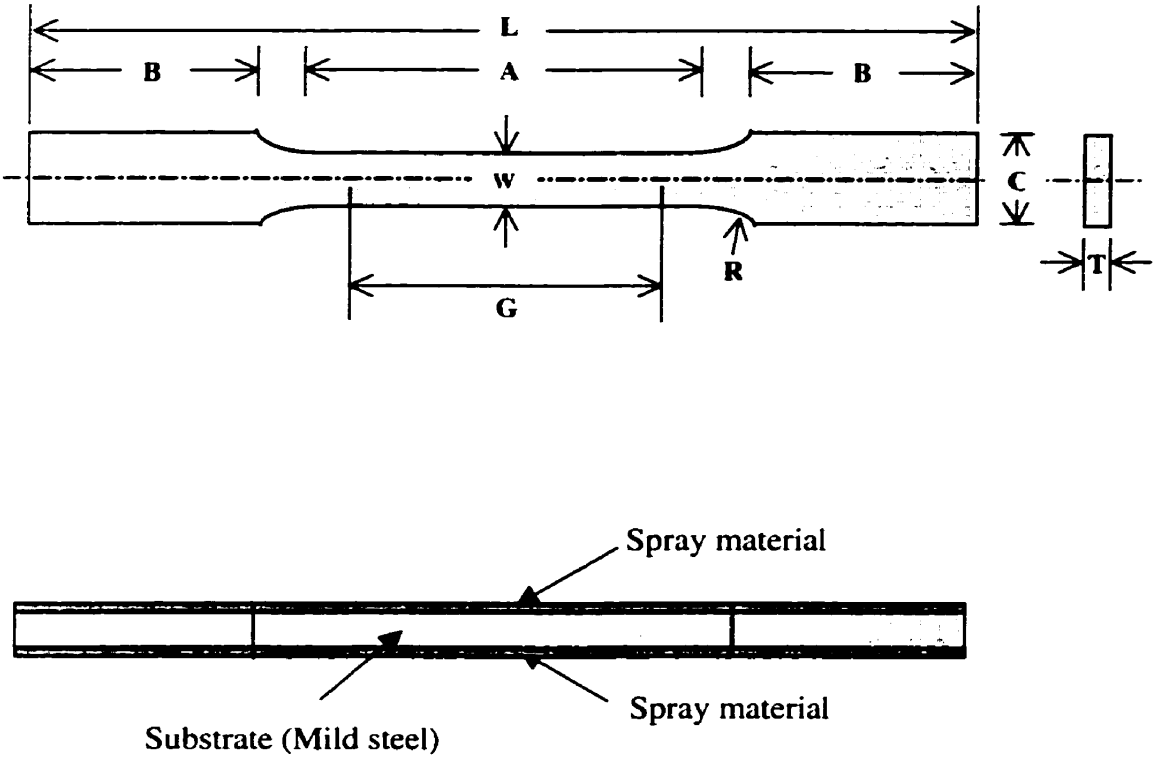

Figure 3-2: Dimensions of standard tension specimen

Legend	Description	Dimension (mm)
G	Gage length	50
W	Width	12.5
T	Thickness	5
R	Radius of fillet	20
L	Over-all length	220
A	Length of reduced section	60
B	Length of grip section	50
C	Width of grip section	20
t	Spray coating thickness	3.5

Table 3-1: Dimensions and legends of test specimens

Specimen Label	Number of Specimen	Substrate Material	Spray Material
S	3	Steel	None
S-ZnZn	3	None	Pure Zinc (99.5%)
S-Zn	3	Steel	Pure Zinc (99.5%)
S-Al	3	Steel	Pure Aluminum (99.5%)
S-ZnAl	3	Steel	$Zinc^{85}Aluminum^{15}$ alloy (Zn-85%, Al-15%)

Table 3-2: Tested specimens in Phase 1

3.2.2 Fabrication of Test Specimens

Three identical specimens of each type of spray coating (Zinc, Aluminum, and Zinc-Aluminum alloy), three uncoated (control) specimens, and three pure Zinc specimens were fabricated and tested. The standard specimens made from plain thermal spray materials (e.g. Zinc, Aluminum and Zinc-Aluminum alloy) were initially planned for tension test. Unfortunately, it was only possible to make a standard specimen with plain sprayed Zinc material. Other materials, such as Aluminum and $Zinc^{85}$-$Aluminum^{15}$ alloy were too brittle and of low tensile strength to make specimens with. Therefore, specimens with these materials were produced by thermally spraying the materials on the steel substrate to produce a thick spray coating.

In general, cracks of the spray material and debonding from the substrate, as illustrated in Figure 3-3, were observed during fabrication. These defects resulted in poor quality specimens. To alleviate this problem, the spray materials should be applied at an appropriate rate, layer by layer, to reduce the formation of residual stresses in the spray coating. Compressed air could be applied on the back of the steel substrate to help dissipate the heat in the spray material.

Initially, it was difficult to control the thickness of the thermal spray coating on specimens. To solve this problem, the coating was sprayed thicker than the desired thickness and was later machined to the required thickness. This method provided a flat and smooth final surface.

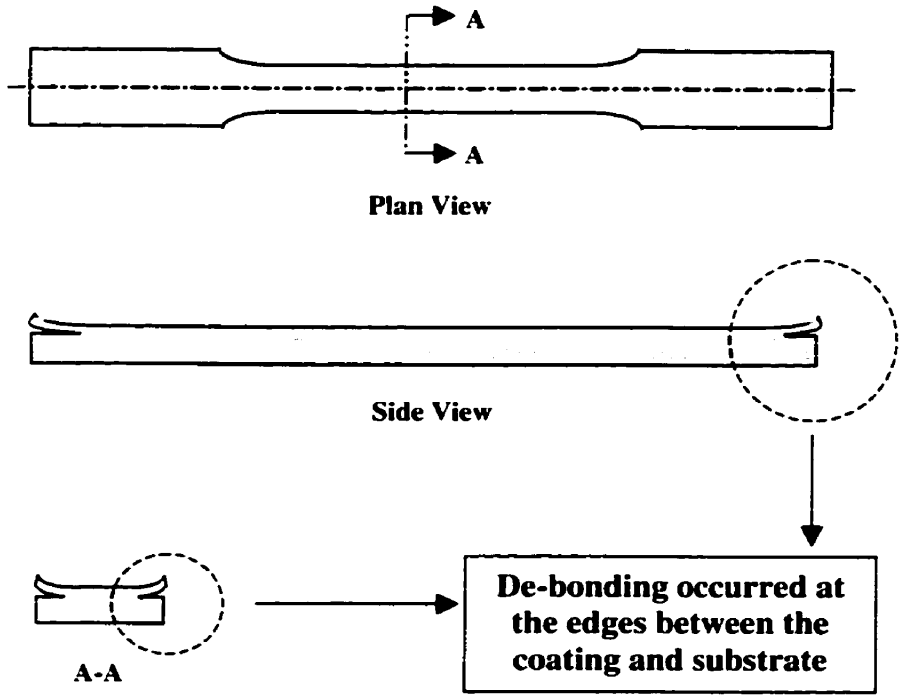

Figure 3-3 : Edge effect between the spray coating and the substrate material

3.2.3 Instrumentation

Bi-axial linear strain gauges were used to monitor the longitudinal and transverse strains at the center of the specimens on both the steel substrate and the spray coating. A 96-channels data acquisition unit capable of 100 readings per second was used to record the strains and the applied loads.

3.2.4 Test Procedure

A Baldwin testing machine with a 130-kN (30-kips) capacity was used in this testing program. The standard grip system shown in Figure 3-4 was used to hold the specimen in place and apply the load. The tests were conducted according to the specifications of the ASTM standard. Loading was applied slowly at the beginning until the grip between the machine and the specimen was fully developed. Then, the rate of loading was adjusted to, approximately, 0.002 mm/sec up to failure. The test results obtained in this phase of the experimental program are discussed in Chapter 4.

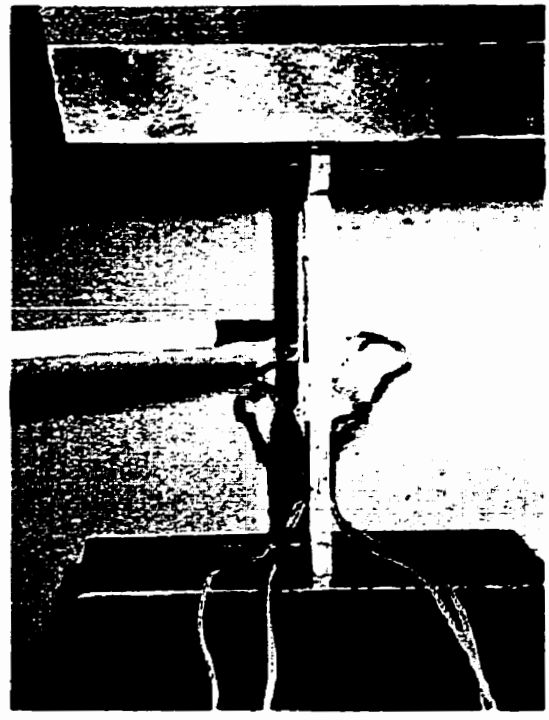

Figure 3-4: Test set-up for standard tension coupons

3.3 Phase 2 - Static Compression Tests on Coupons

Three groups of compression specimens were tested in the second phase of the investigation. The first group of specimens consisted of three perfectly cylindrical steel specimens which served as the control specimens. The dimensions of these specimens are given in Figure 3-5(a). The second group of specimens consisted of three cylindrical steel specimens that were machined to provide a reduced cross section, as shown in Figure 3-5(b). The objective of these tests was to investigate the strength of the specimens prior to spray-coating. The third group of specimens, shown in Figure 3-5(c), was fabricated by spraying machined steel specimens, similar to those of group 2, with spray material. A total of nine specimens of this group were tested: three coated with $Zn^{85}Al^{15}$, three coated with 10-carbon steel and three coated with 40-carbon steel. The specimens were labeled in a similar way on the tension specimens in Phase 1. For example, specimen C-ZnAl was a steel specimen coated with $Zn^{85}Al^{15}$ alloy and tested under compression (C). The types of specimens tested in this phase are listed in Table 3-3.

3.3.1 Test Specimens

ASTM (E9-89a) Standard specifies the test procedure and dimensions of compression metallic specimens tested at room temperature [32]. A height-to-diameter ratio of three was used for the cylindrical specimens in this testing program. The height and diameter of the specimens were 76.20 mm (3.0 inch) and 25.40 mm (1.0 inch), respectively. However, there is no standard test for composite specimens consisting of a metallic substrate and a thick spray coating. Therefore, the spray-coated specimens were

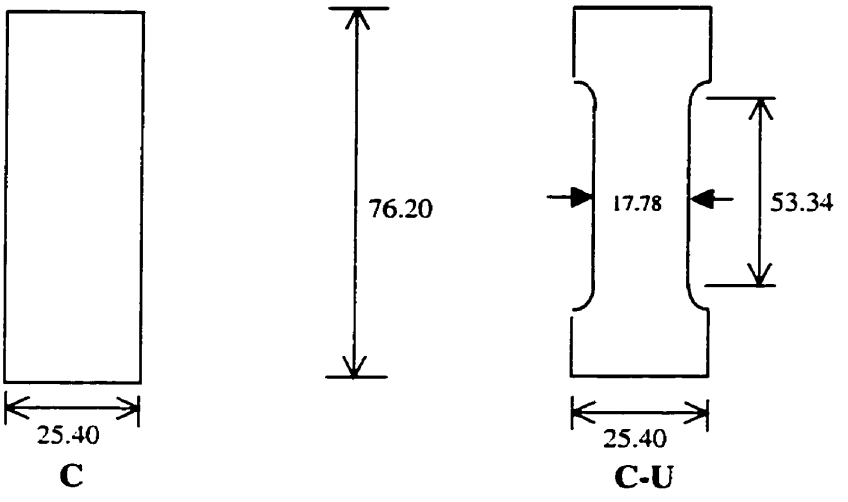

(a) Group 1: Perfect specimen **(b) Group 2: Uncoated specimen**

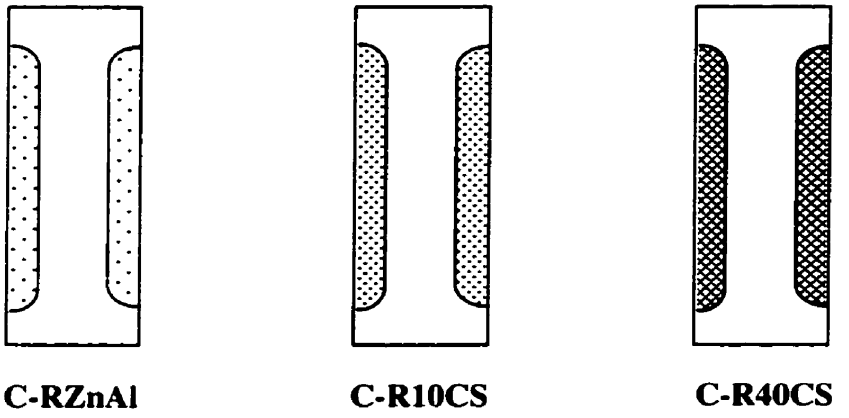

(c) Group 3: Spray-coated specimens

Material Type

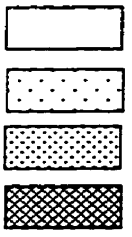

Solid steel

$Zinc^{85}Aluminum^{15}$ Alloy (Spray material)

10-carbon Steel (Spray material)

40-carbon Steel (Spray material)

Figure 3-5: Dimensions and materials of the compression specimens

modified to serve the purpose of the test program. A height-to-diameter ratio of three was used in both the unreduced (group 1) cross sections (76.20/25.40) and the reduced (group 2) cross sections (53.34/17.78). The ratio of three is recommended in evaluating the mechanical properties of metals under compression loading [33]. The specimens tested in this phase are summarized in Table 3-3.

Table 3-3: Compression specimens in Phase 2

Specimen Label	Number of Specimens	Substrate Material	Spray Material
C	3	Hardened Steel	None (Perfect cylindrical specimen)
C-U	3	Hardened Steel	None (Machined cylindrical specimen)
C-ZnAl	3	Hardened Steel	Zinc(85%) Aluminum(15%) alloy
C-10CS	3	Hardened Steel	10-carbon steel
C-40CS	3	Hardened Steel	40-carbon steel

Legend:
C = Compressive cylindrical specimens
U = Uncoated
ZnAl = $Zinc^{85}Aluminum^{15}$ alloy
10CS = 10-carbon steel
40CS = 40-carbon steel

3.3.2 Fabrication of Test Specimens

It is difficult to fabricate purely sprayed specimens in cylindrical form for test purposes. This is due to the nature of the thermal spraying process that makes the deposition of molten particles difficult in a hollow mold. An attempt was initially made to fabricate specimens inside a mold with a hollow space of cylindrical shape. However, the compressed air used to propel molten particles tended to blow the particles out from the mold. The deposition of spray material inside the mold was impossible. To solve this problem, steel substrate was used to assist the deposition of spray material. All steel substrates used in this phase of the testing program were extracted from a single cylindrical rod. The cylindrical steel specimens were machined to produce the reduced cross section and were spray-coated with various materials to produce a thicker coating, in order to machine all spray-coated specimens to the same diameter of 25.4mm (1 inch). Three spray materials were used: $Zinc^{85}Aluminum^{15}$ alloy, 10-carbon steel (steel with 0.1% carbon content) and 40-carbon steel (steel with 0.4% carbon content).

3.3.3 Instrumentation

Two bi-axial strain gauges were placed on opposite sides of each specimen. Average strain measurements were calculated and used in the analysis. The results were reported in chapter 4. A load cell in the testing machine was used to measure both the applied loads and the shortening of the specimen during the tests. The applied loads, the displacements and the strains were recorded by a data acquisition system.

3.3.4 Test Procedure

A closed-loop MTS 1000-kN (225-kips) testing machine was used to conduct the compression testing on the cylindrical specimens. Figure 3-6 shows the standard test set-up which was used according to the ASTM standard (E9 - 89a). Initially, a small amount of loading was applied which was adjusted to ensure that the loading was applied concentrically. A loading rate of 0.002 mm/sec was used for compression testing. All specimens were tested up to failure which was due to either crushing of the spray coating or buckling of the specimen.

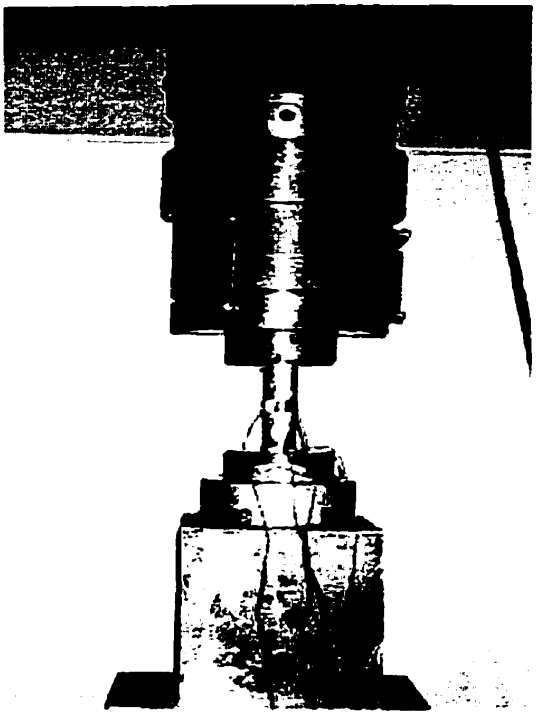

Figure 3-6: Test set-up for compression specimens

3.4 Phase 3 - Static Compression Test on Steel Angle Specimens

Fourteen steel angle specimens were tested in this phase. Various artificial defects, such as a circular hole, an elliptical indentation, and an elliptical indentation with a circular hole, were machined in the steel angle sections to simulate damage from corrosion. The simulated defects were then repaired with spray materials. The objective of these tests was to investigate the performance of steel sections repaired by the thermal spray metallizing technique.

3.4.1 Test Specimens

The test specimens were 850-mm long L76x76x4.8 (G40.21-350W) steel angles [34]. The cross-sectional properties of these specimens are listed in Table 3-4. Figure 3-7 shows the specimens tested, including the size of the defects machined to simulate corrosion damage. Two groups of specimens were machined and repaired. Specimens L1 were repaired with 10-carbon steel while specimens L2 were repaired with 40-carbon steel. The decision to use carbon steels as the repair material was based on the test results in Phases 1 and 2. The types of specimens tested in this phase are listed in Table 3-5. The labels used in identifying the specimens are also listed in this table.

3.4.2 Fabrication of Test Specimens

The test specimens consisted of 14 angle sections cut from two 6-m long pieces. All L1 specimens were cut from one piece while the L2 specimens were cut from the other. The cross-sectional properties and the yield strength of these pieces are given in Table3-4.

Table 3-4: Sectional and material properties of steel angles

Section	Area (mm^2)	I_y (mm^4)	r_y (mm)	J (mm^4)	C_w (mm^6)	Yield strength(F_y) (MPa)
L1	703	0.4×10^6	15.1	5.31×10^3	0.00241×10^9	400
L2	703	0.4×10^6	15.1	5.31×10^3	0.00241×10^9	400

All sprayed specimens were de-greased and grit-blasted prior to the thermal spraying process. The specimens with the circular holes were sprayed with a stainless steel block placed at the back of the hole. This allowed the proper deposition of spray material in the hole. Stainless steel was chosen because it had a smooth and hard surface. The bonding between the spray coating and the stainless steel substrate was weak and could be easily removed after the spraying process. Spray material was applied layer by layer with proper rate to control the amount of heat that would generate in spray coatings. The spray material was applied carefully in the areas where material had been removed and, later, it was milled to provide a final flat and smooth surface for instrumentation.

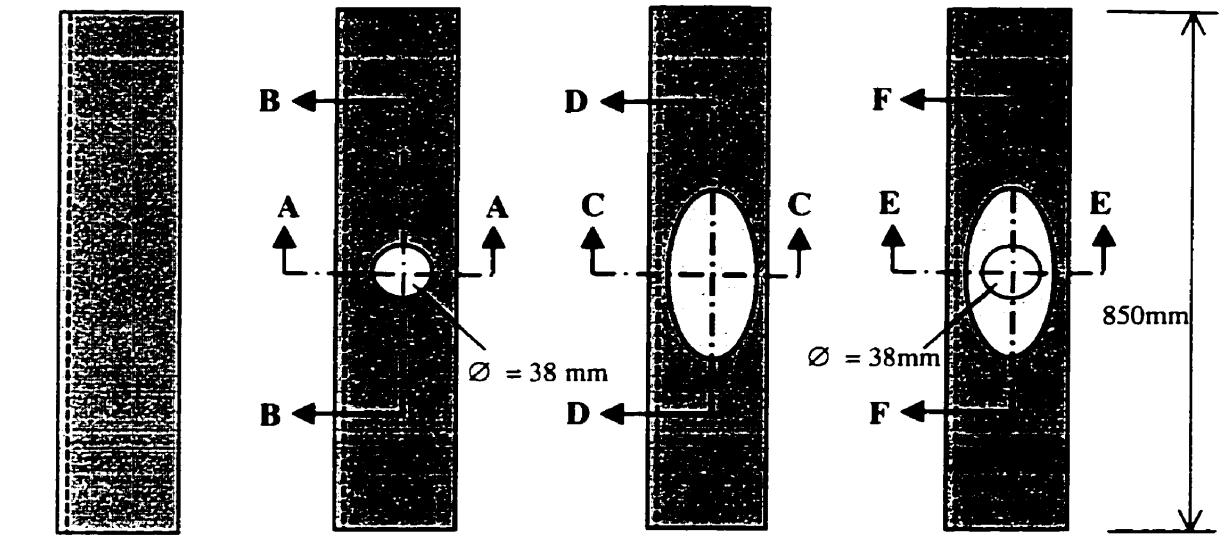

(a) Specimen L (b) Specimen L-O (c) Specimen L-E (d) Specimen L-EO

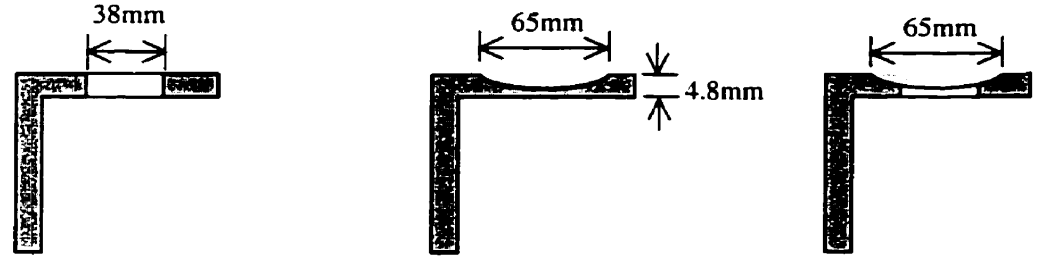

(e) Section A-A (f) Section C-C (g) Section E-E

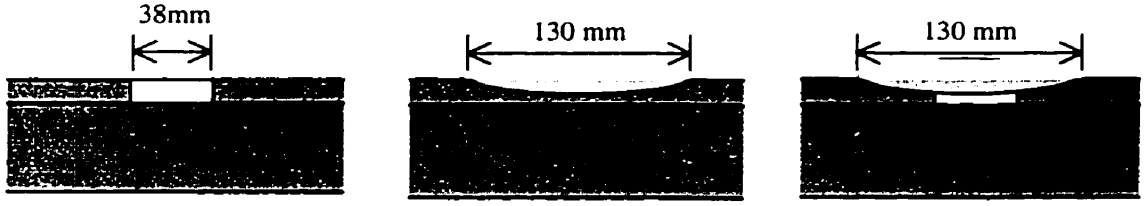

(h) Section B-B (i) Section D-D (j) Section F-F

Figure 3-7: Dimensions of steel angle specimens

Table 3-5: Steel angle specimens tested in Phase 3

Specimen Type	Simulated Defect	Spray Material
L1	None	None
L2	None	None
L1-OU	Circular hole	None
L2-OU	Circular hole	None
L1-OR-10CS	Circular hole	10-carbon steel
L2-OR-40CS	Circular hole	40-carbon steel
L1-EU	Elliptical	None
L2-EU	Elliptical	None
L1-ER-10CS	Elliptical	10-carbon steel
L2-ER-40CS	Elliptical	40-carbon steel
L1-EOU	Elliptical plus circular hole	None
L2-EOU	Elliptical plus circular hole	None
L1-EOR-10CS	Elliptical plus circular hole	10-carbon steel
L2-EOR-40CS	Elliptical plus circular hole	40-carbon steel

Legend:

L1 = Angle section cut from piece 1
L2 = Angle section cut from piece 2

O = Circular hole
E = Elliptical
EO = Elliptical plus circular hole

U = Unrepaired specimen
R = Repaired specimen

10CS = 10-carbon steel
40CS = 40-carbon steel

3.4.3 Instrumentation

Bi-axial strain gauges were mounted at the center of the undamaged leg of all specimens. The control specimens were instrumented with strain gauges attached to both legs to verify that the loading was applied uniformly on both legs. Strain gauges were also attached to the damaged leg of the specimens, whenever possible. For instance, in the unrepaired specimens with elliptical indentation plus hole, strain gauges were attached on the undamaged leg because it was impossible to attach them on the damaged leg. In the repaired sections, the strain gauges were attached to the undamaged and the damaged legs on both the steel and spray materials. The applied loads and the displacements were recorded by a data acquisition system.

3.4.4 Test Procedure

The same closed-loop MTS 1000-kN (225-kips) testing machine used in Phase 2 was also used in this phase. Figures 3-8 and 3-9 show the test set-up and the pin-ended support condition. The support system allowed load to be applied through the centroid of the specimens while at the same time the steel ball bearing allowed the specimens to rotate about the centroidal axes. A loading rate of 0.003 mm/sec was used to test the specimens under compression. The specimens were tested to failure which was due to either crushing of the spray material (brittle behavior) or local buckling of the steel angle near the damaged area. The results from the tests are discussed in Chapter 4.

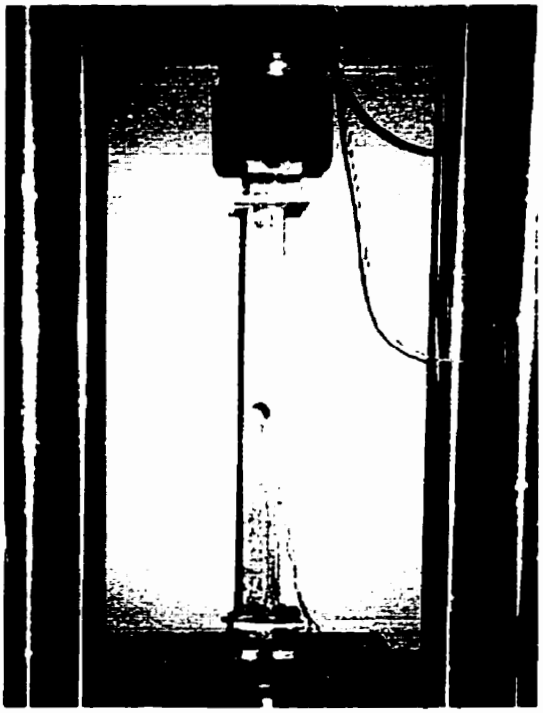

Figure 3-8: Test set-up for steel angle specimens

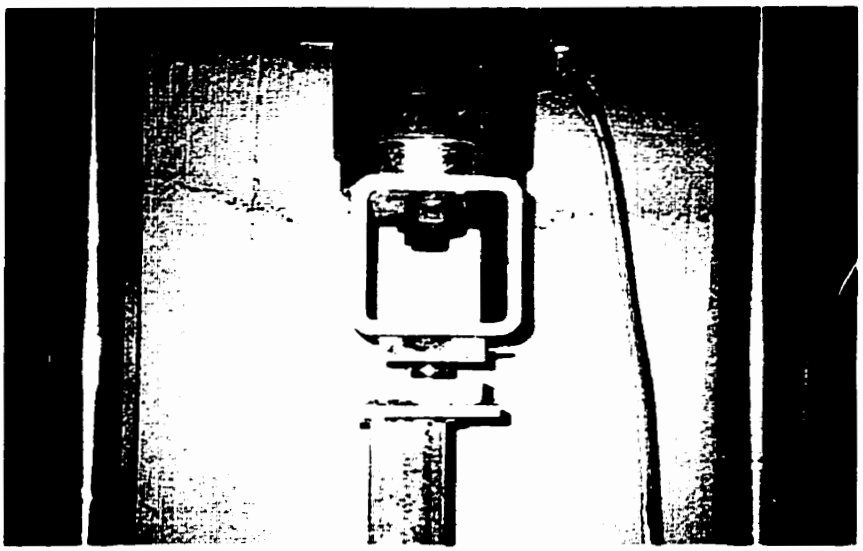

Figure 3-9: A close-up of a pin support in the test set-up

3.5 Phase 4 - Static Tension Test on Flat Plates Specimens

Seven flat plate specimens were fabricated and tested under tension in this phase. The plate specimens were designed so the strain distribution at the mid-span of the perfect specimens was uniform. The objective of these tests was to investigate the effectiveness of thermal spray metallizing as a repair technique for tension steel members.

3.5.1 Test Specimens

The flat plate specimens were fabricated with a gauge length L = 270 mm to ensure that failure occurred within the reduced region. Figure 3-10 provides the dimensions of the tension plate specimens. Two holes with a diameter of 38-mm were drilled at center line and at 50-mm from the ends to insert the pins through which the loading was applied during the test. The ends of the specimens were reinforced with stiffening plates on both sides to avoid failure at these locations during loading. The thickness of the specimens was 4.8 mm. The same defects used in the compressive steel angle specimens, shown in Figure 3-7, were fabricated to simulate loss of mass due to corrosion in the plate specimens. 10-Carbon steel was chosen as the repair material since this material performed well during the testing of the steel angle specimens under compression. Table 3-6 lists the specimens tested in this phase.

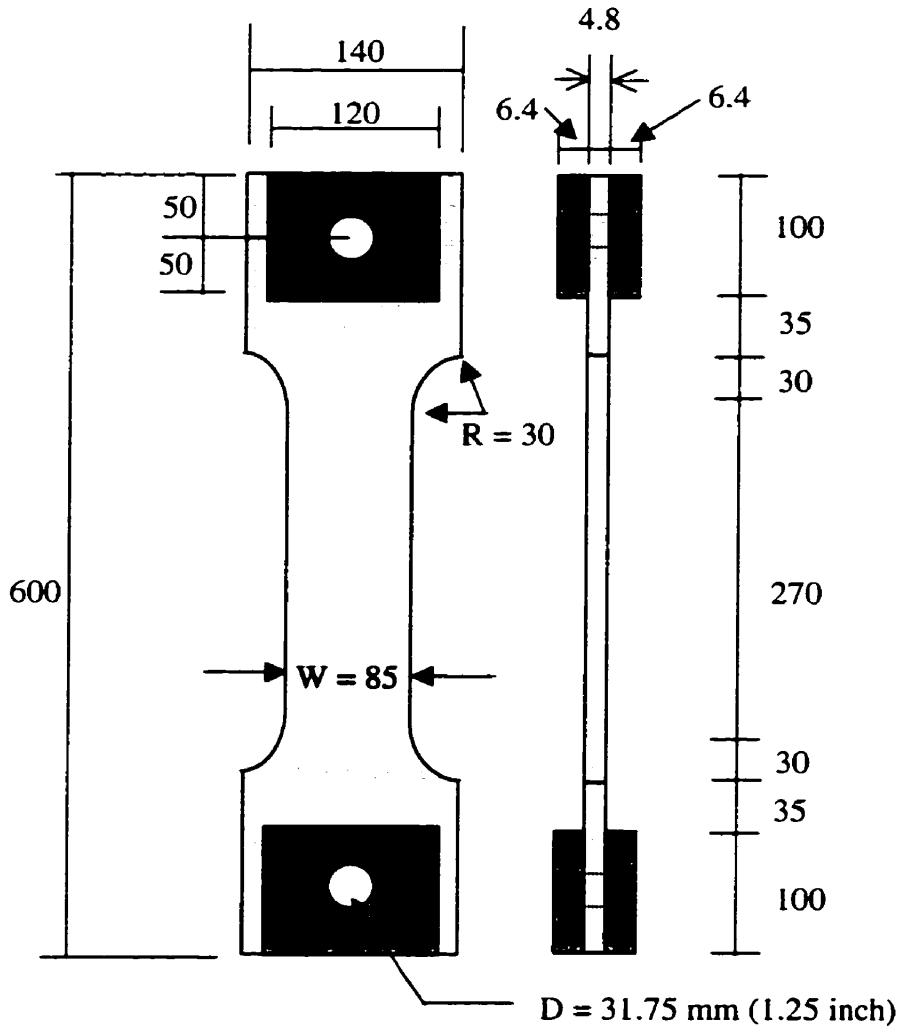

Figure 3-10: Dimensions of tension plate specimens (mm)

Table 3-6: Tension Plate specimens

Specimen Type	Simulated Defect	Spray Material	Legend
P	None	None	P = Tension plate specimen
P-OU	Circular hole	None	O = Circular hole
P-OR-10CS	Circular hole	10-carbon steel	E = Elliptical
P-EU	Elliptical	None	EO = Elliptical + circular hole
P-ER-10CS	Elliptical	10-carbon steel	U = Unrepaired
P-EOU	Elliptical + circular hole	None	R = Repaired
P-EOR-10CS	Elliptical + circular hole	10-carbon steel	10CS = 10-carbon steel

3.5.2 Fabrication of Test Specimens

The plate specimens were cut from a large steel plate to ensure constant material properties of the substrate. One plate specimen without defects was used as the control specimen while the other six specimens were machined to produce the same defects as the compressive steel angle specimens. The same thermal spraying procedure used in Phase 3 was also used to repair the defective specimens.

3.5.3 Instrumentation

The specimens were instrumented with strain gauges attached on one side at the locations shown in Fig. 3-11. The locations were chosen so that the strain distribution across the specimen could be measured. Bi-axial strain gauges were attached at the center of those specimens without the circular hole defect to measure the longitudinal and transverse strains. Specimens that had been repaired with spray material at the center were also instrumented with bi-axial strain gauges attached on both the substrate and spray material to measure strains.

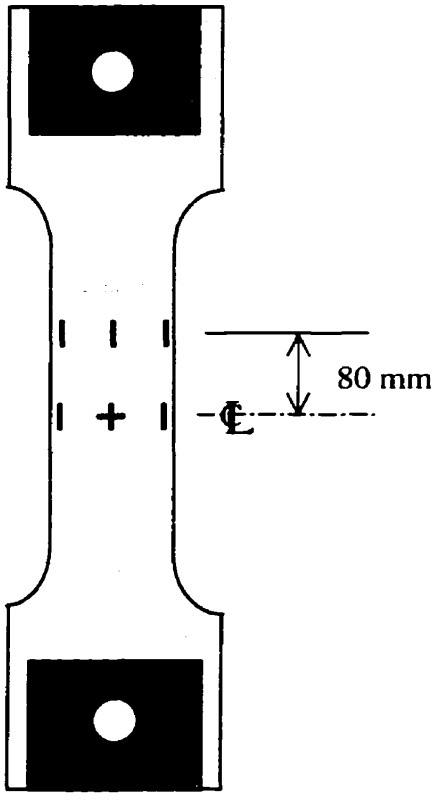

Figure 3-11: Location of strain gauges on plate specimen

3.5.4 Test Procedures

The 1000-kN (225-kips) closed-loop MTS testing machine was used to test the tension plate specimens. The test set-up shown in Figure 3-12 was prepared to perform the testing under tension up to failure. A loading rate at 0.003 mm/sec was maintained during testing up to yielding. After that, the loading was increased to 0.005 mm/sec until failure. The test results from Phase 4 are discussed in Chapter 4.

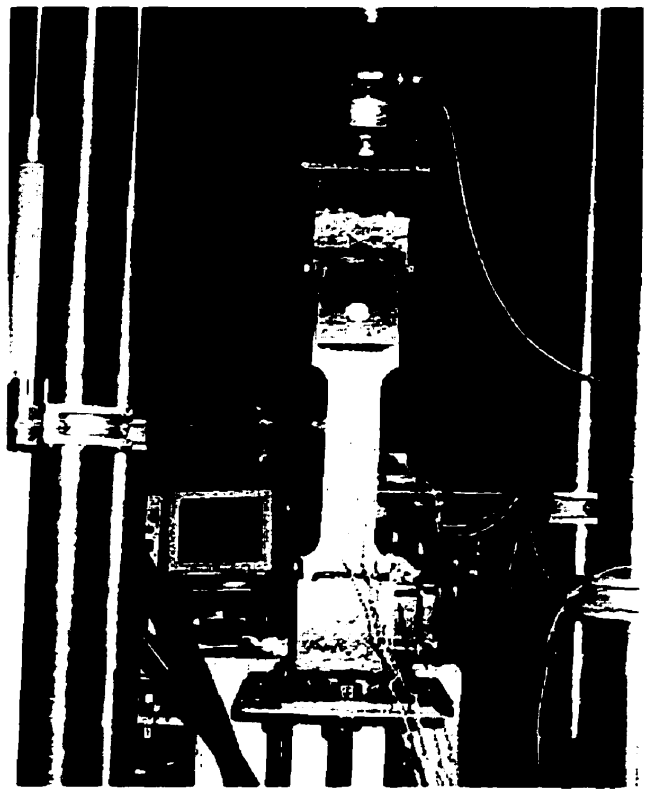

Figure 3-12: Test set-up for tension plate specimens

CHAPTER 4

TEST RESULTS AND ANALYSIS

4.1 General

In this chapter the results from the four phases of the experimental program are presented and analyzed. The results are in the form of stress-strain figures, specimen capacity, and load distribution. The information presented will be used in Chapter 5 where Finite Element modeling is carried out using the ANSYS computer program. The results from each phase of the experimental program are presented below.

4.2 Phase 1 : Static Tension Test on Standard Coupons

A total of 17 standard specimens were tested in this phase to investigate the tensile properties of spray materials. The results in the form of stress-strain graphs are plotted in Figures 4-1 to 4-5. The failure mode for the various specimens is shown in Figures 4-6 to 4-10.

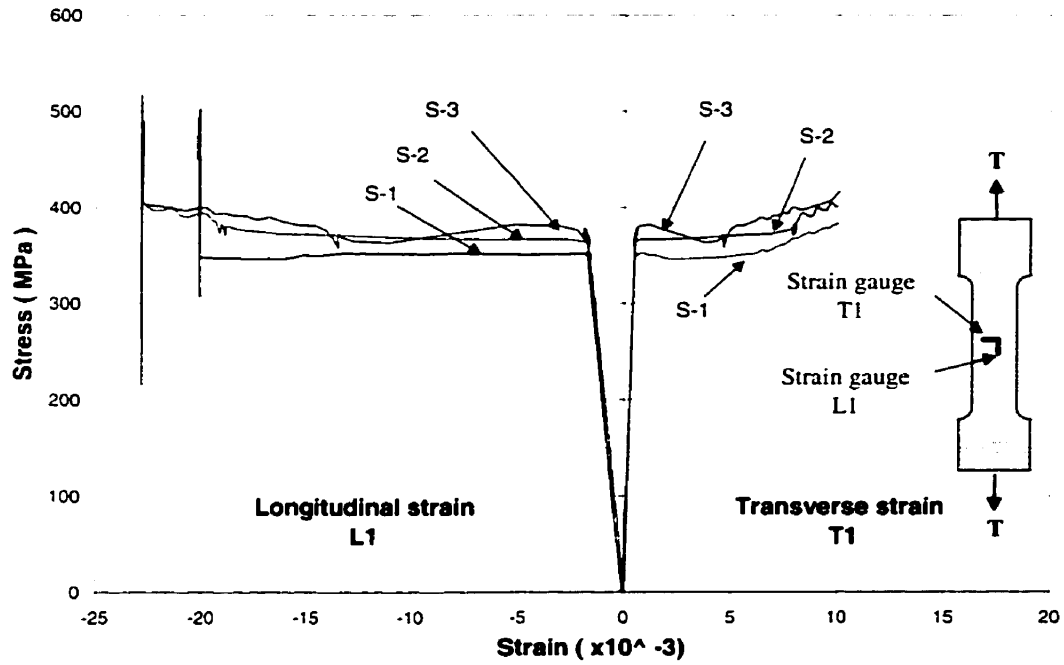

Figure 4-1: Stress-strain diagrams for plain steel specimens (S-1,2,3)

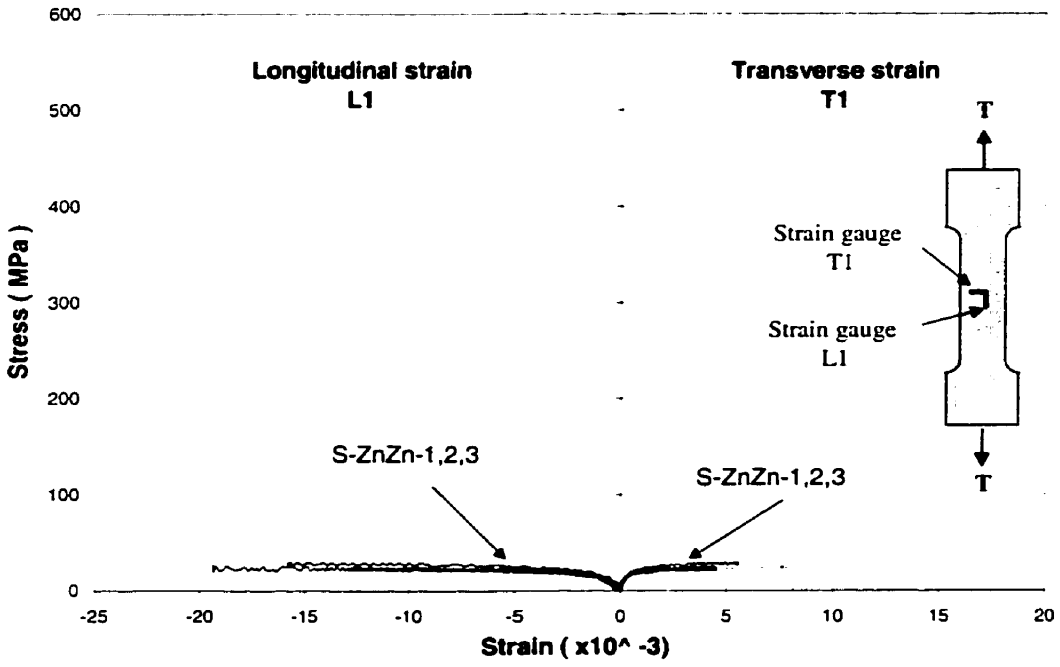

Figure 4-2: Stress-strain diagrams for S-ZnZn-1,2,3 specimens

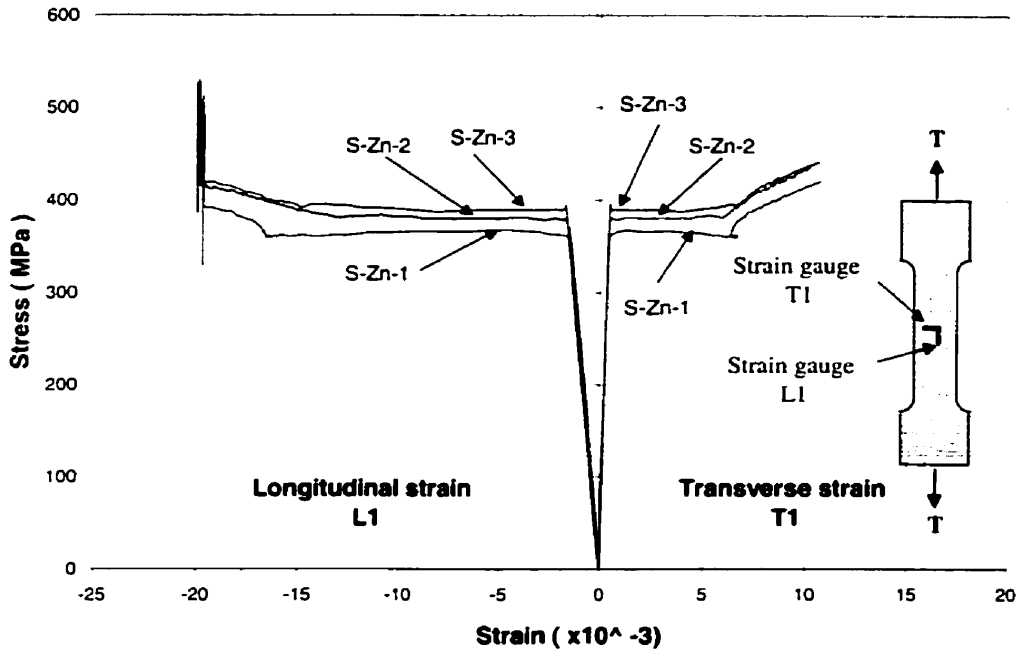

Figure 4-3: Stress-strain diagrams for Zinc coated specimens (S-Zn-1,2,3)

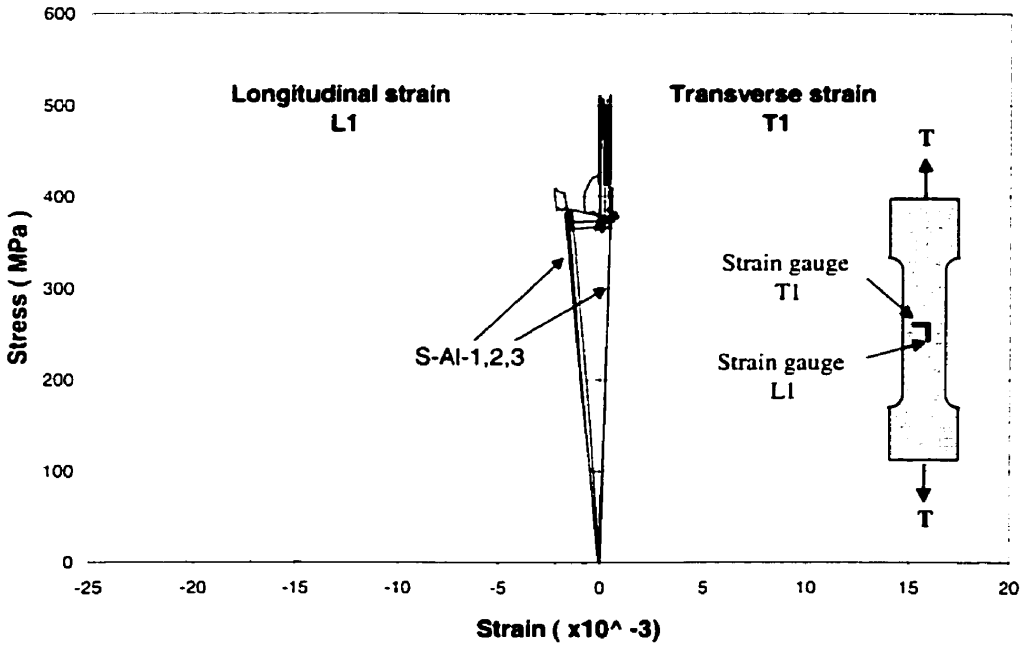

Figure 4-4: Stress-strain diagrams for Aluminum coated specimens (S-Al-1,2,3)

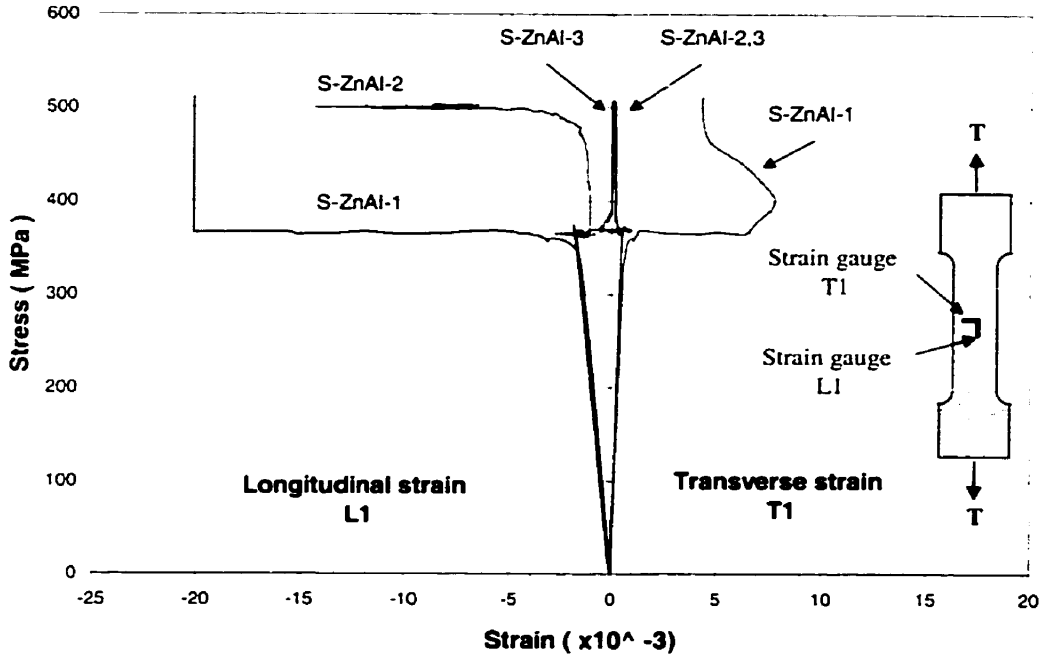

Figure 4-5: Stress-strain diagrams for $Zn^{85}Al^{15}$ coated specimens (S-ZnAl-1,2,3)

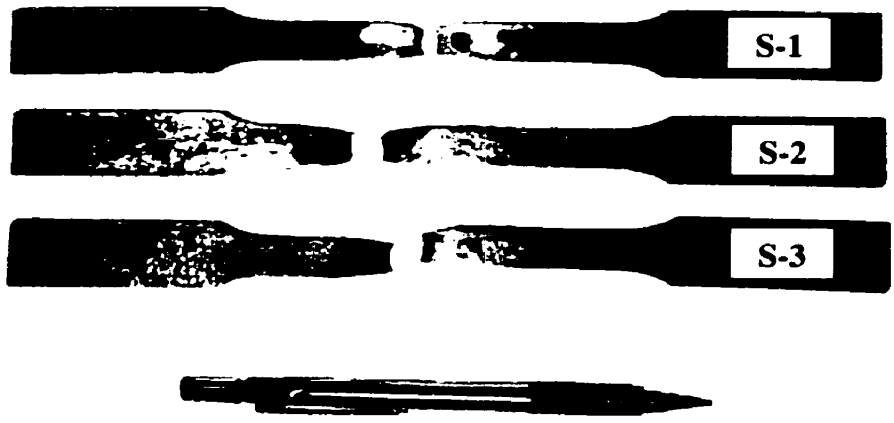

Figure 4-6: Failure of plain steel specimens (S-1,2,3)

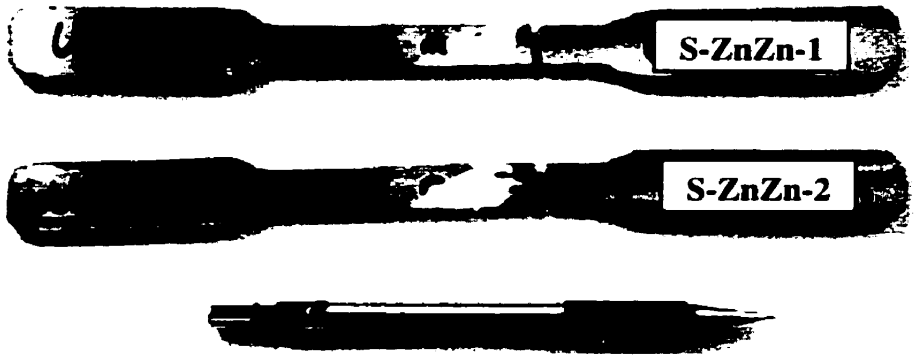

Figure 4-7: Failure of plain (sprayed) Zinc specimens (S-ZnZn-1,2)

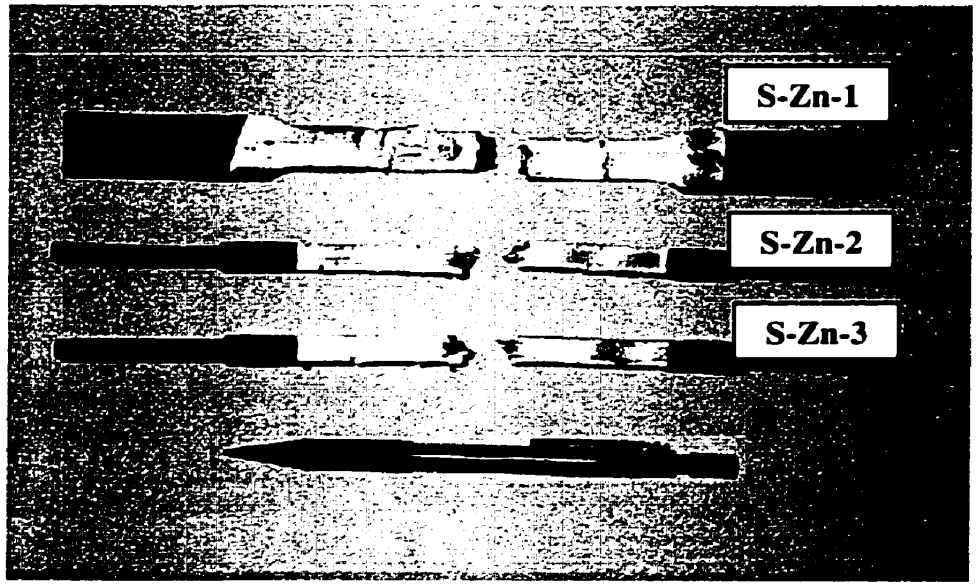

Figure 4-8: Failure of Zinc coated specimens (S-Zn-1,2,3)

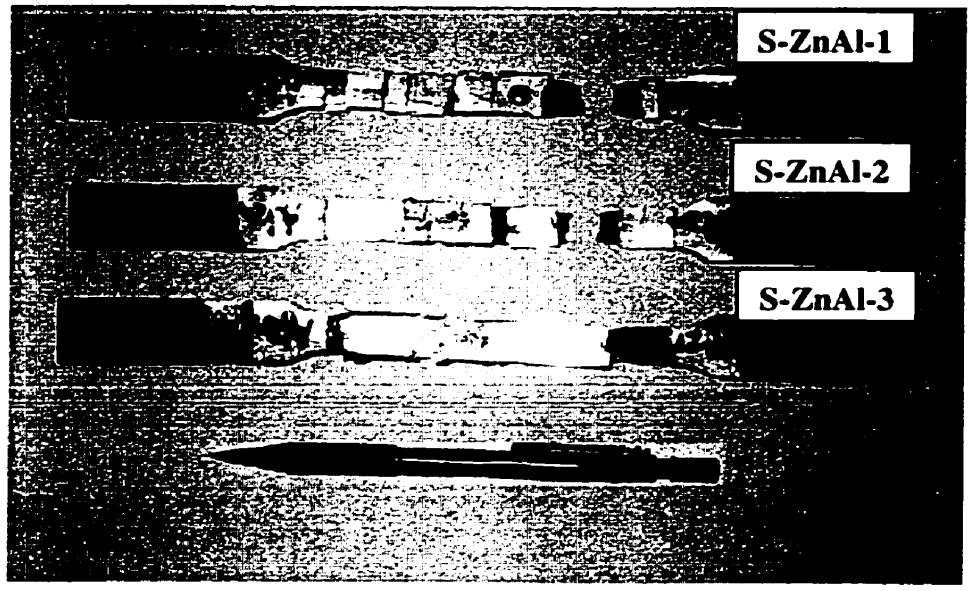

Figure 4-9: Failure of $Zn^{85}Al^{15}$ coated specimens (S-ZnAl-1,2,3)

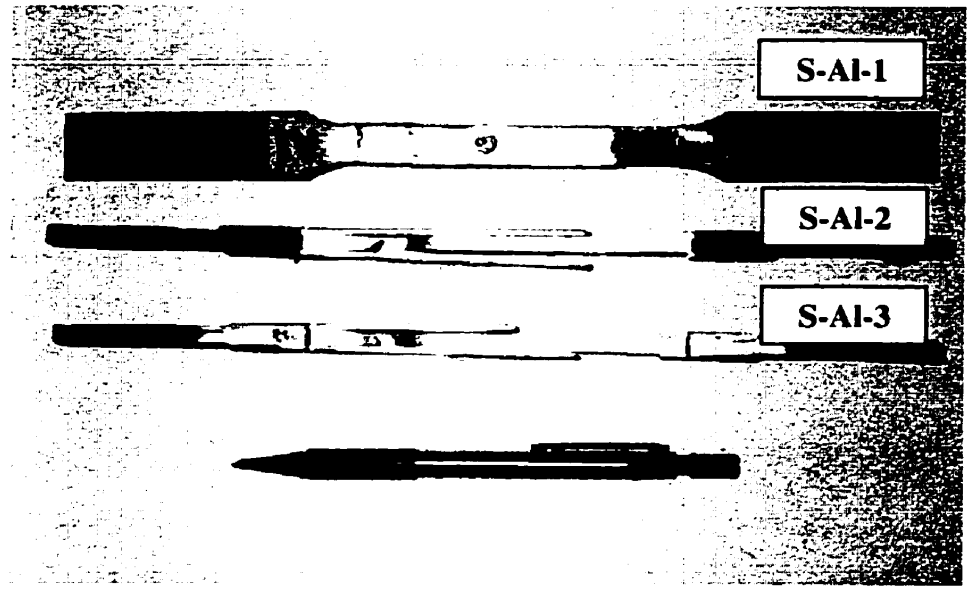

Figure 4-10: Failure of Aluminum coated specimens (S-Al-1,2,3)

As shown in Fig. 4-6, the plain steel specimens (S-1,2,3) exhibited typical yielding failure modes by stretching and necking at failure. The failure of the specimen fabricated from pure sprayed Zinc is shown in Figure 4-7. This specimen failed at, approximately, 25 MPa by cracking across the reduced section. This result clearly shows that tension specimens composed of plain spray materials have very little tensile strength.

In the spray-coated steel specimens two failure modes were observed: cracking and de-bonding of the spray coating. As shown in Fig. 4-8, in the Zinc coated specimens, cracks were produced on the Zinc coating, followed by de-bonding of the spray coating starting at the edge of the specimens. The $Zn^{85}Al^{15}$-coated specimens, shown in Figure 4-9, exhibited a failure mode similar to that of Zinc-coated specimens. More cracks were produced in this type of specimen. However, the spray coating was fully de-bonded from the steel substrate at failure. In contrast, the Aluminum coating, shown in Figure 4-10, was de-bonded from the substrate before any tension cracks had developed. The failure modes showed that the Zinc coating was the least brittle coating among the three spray coatings. The most brittle spray material was Aluminum which exhibited de-bonding before failure by cracking. The cracking pattern in the $Zn^{85}Al^{15}$ coating indicated that it is more brittle than the sprayed Zinc but less brittle than the sprayed Aluminum. The observations of Zinc and $Zn^{85}Al^{15}$-coated specimens also indicated that the tensile strength of spray coatings was lower than their bond strength.

4.2.1 Stress-Strain Behavior

Strain readings after cracking or after debonding of the spray coating were ignored in the analysis of the results. The stress-strain curves for plain steel and plain spray material of Zinc are shown in Figures 4-1 and 4-2. The average yield stress of the steel obtained from specimen S-1, S-2, and S-3 was found to be 366 MPa. The plain sprayed Zinc had a very low ultimate stress and strain of 25 MPa and 0.0194, respectively.

In general, the test results showed that the spray materials were quite brittle and low in tensile strength. However, the performance of the spray-coated steel specimens was quite different than that of the plain spray-material specimens. The stress-strain curves for these specimens are shown in Figures 4-3 to 4-5. The cross-sectional areas of the individual material components of the specimens are given in Table 4-1. Since the spray materials are weak in tension, the cross-sectional area of the steel substrate only was used to calculate the stress (load/area) of the spray-coated specimens. In this case, the results from spray-coated specimens were compared to the results from the plain steel specimens. The cross-sectional area of the spray coating on the specimens ranged from 26% to 73% of that the steel substrate. If the spray coatings had contributed to an increase in the overall strength of the specimens, the stress-strain curves of the spray-coated specimens would be different from those of the uncoated steel specimens. Otherwise, the spray coatings would not have contributed to the strength of the spray-coated steel specimens.

The stress-strain curves for three spray-coated specimens are shown along with the stress-strain curves of the plain steel specimens (C-2) in Figures 4-11 to 4-13. This curve is used as a comparison for the stress-strain curves of specimens that were spray-coated with Zn, Al and $Zn^{85}Al^{15}$ materials. From the figures, the curves for all spray-coated specimens present no variation from the control steel curve. This indicates that the spray materials are very weak and have no strength effect on the steel substrate under tension stress.

Table 4-1: Cross-sectional properties of standard tension specimens (Phase 1)

Specimen type	Substrate material	Cross Section area (mm^2)	Spray material	Cross section area (mm^2)	Percentage of spray material compared to steel substrate
S	Steel	62.65	None	-	-
S-ZnZn	None	-	Zinc	49.81	-
S-Zn	Steel	63.38	Zinc	40.25	63.51 %
S-Al	Steel	58.2	Aluminum	42.2	72.51 %
S-ZnAl	Steel	57.38	$Zinc^{85}Aluminum^{15}$	14.81	25.81 %

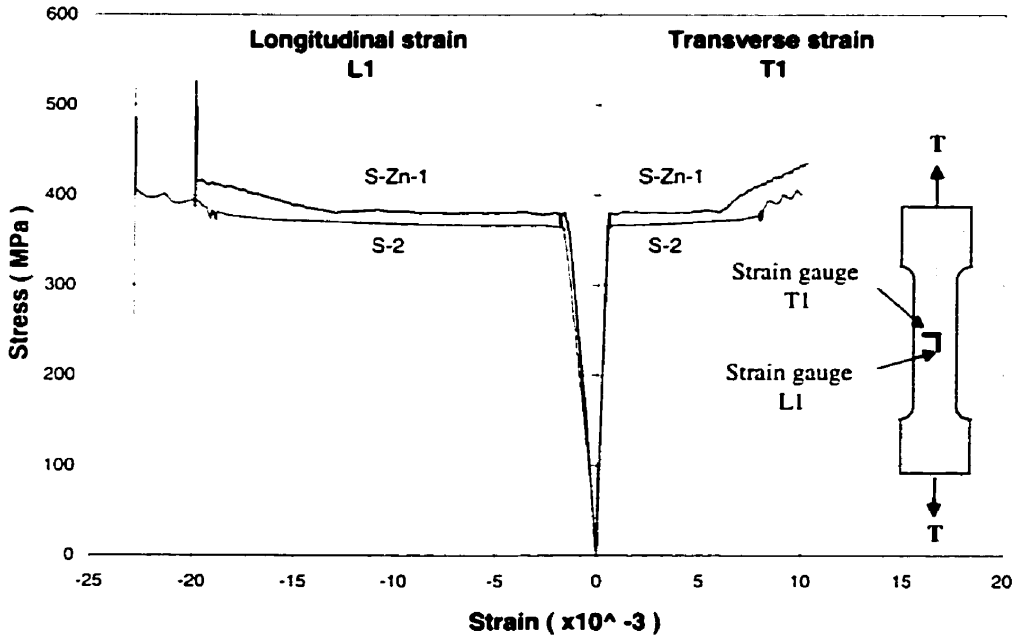

Figure 4-11: Stress-strain curves for plain steel and Zinc coated specimen

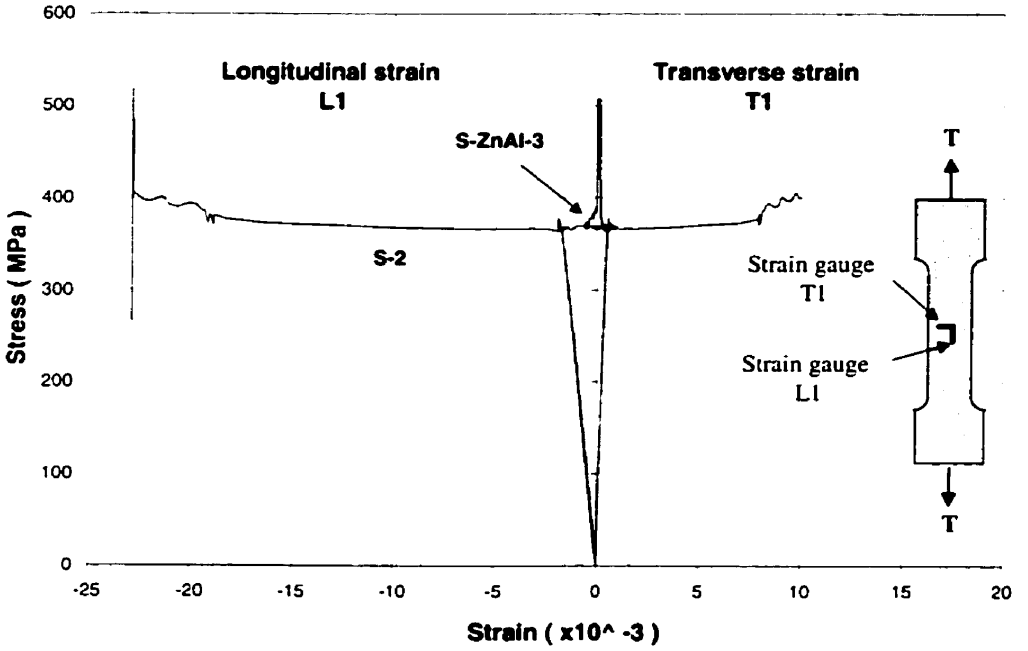

Figure 4-12: Stress-strain curves for plain steel and $Zn^{85}Al^{15}$ coated specimen

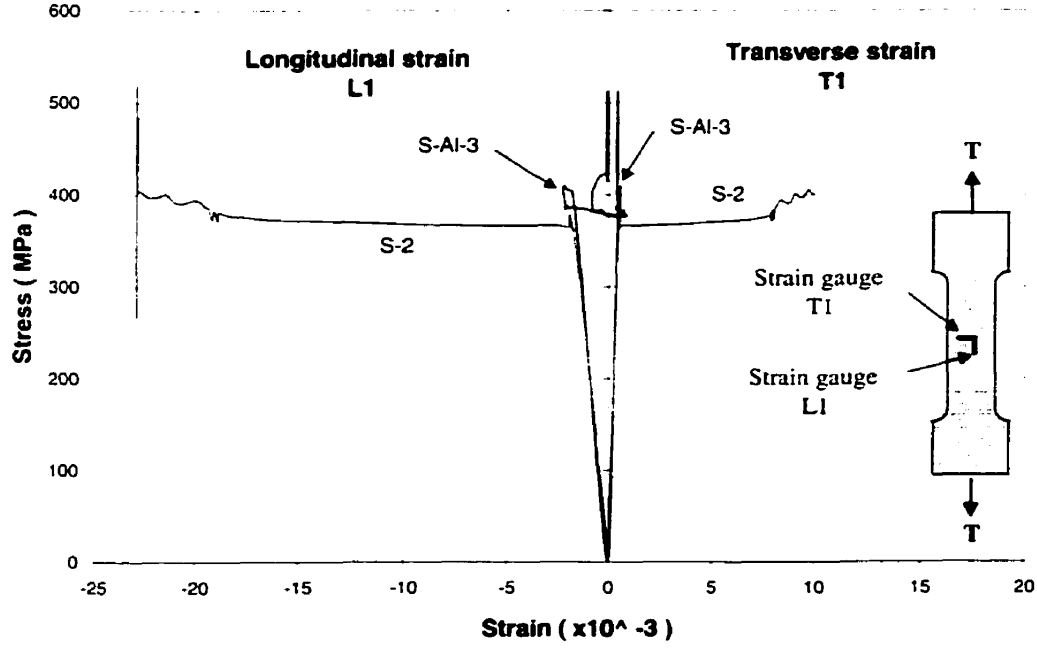

Figure 4-13: Stress-strain curves for plain steel and Aluminum coated specimen

4.3 Phase 2 : Static Compression Test on Coupons

Fifteen specimens were tested under compression to investigate the compressive properties of spray materials. The control specimens, shown in Fig. 4-14, were perfectly cylindrical and the machined specimens, shown in Fig 4-15, were uncoated and consisted of a reduced cross section. The results from these specimens were compared to the results obtained from the spray-coated specimens. The spray materials investigated in this test program were the $Zn^{85}Al^{15}$ alloy, 10-carbon steel (10% carbon content) and 40-carbon steel (40% carbon content). Figures 4-16 to 4-18 show the coated specimens before testing.

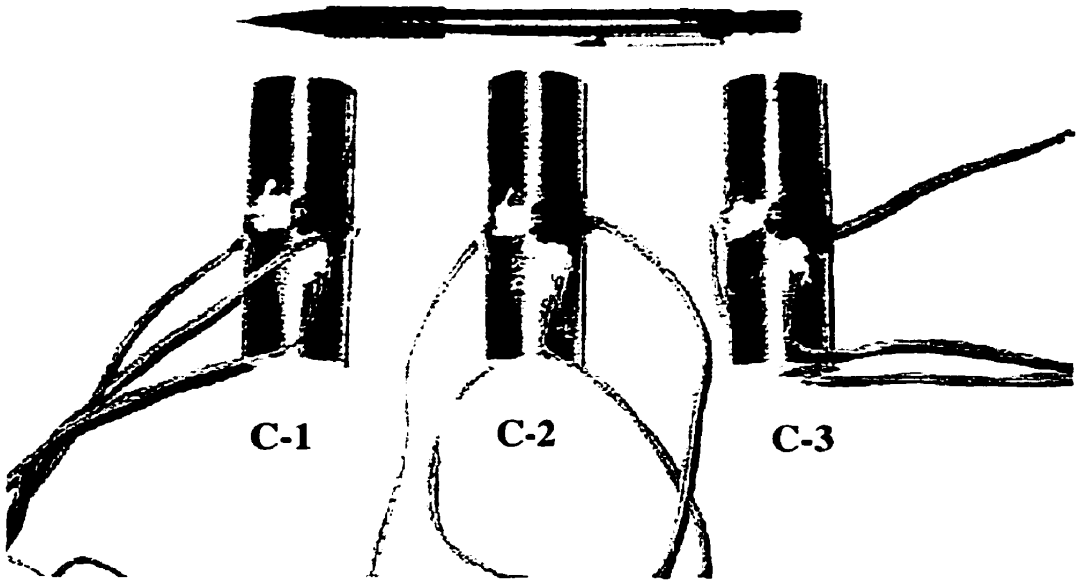

Figure 4-14: Cylindrical steel specimens before testing

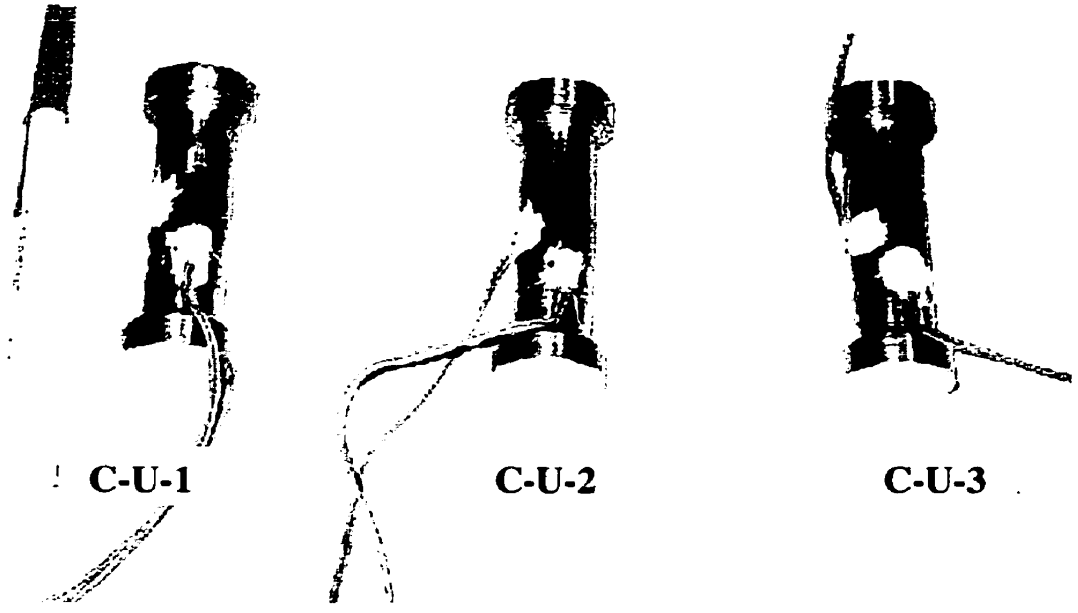

Figure 4-15: Uncoated steel specimens before testing

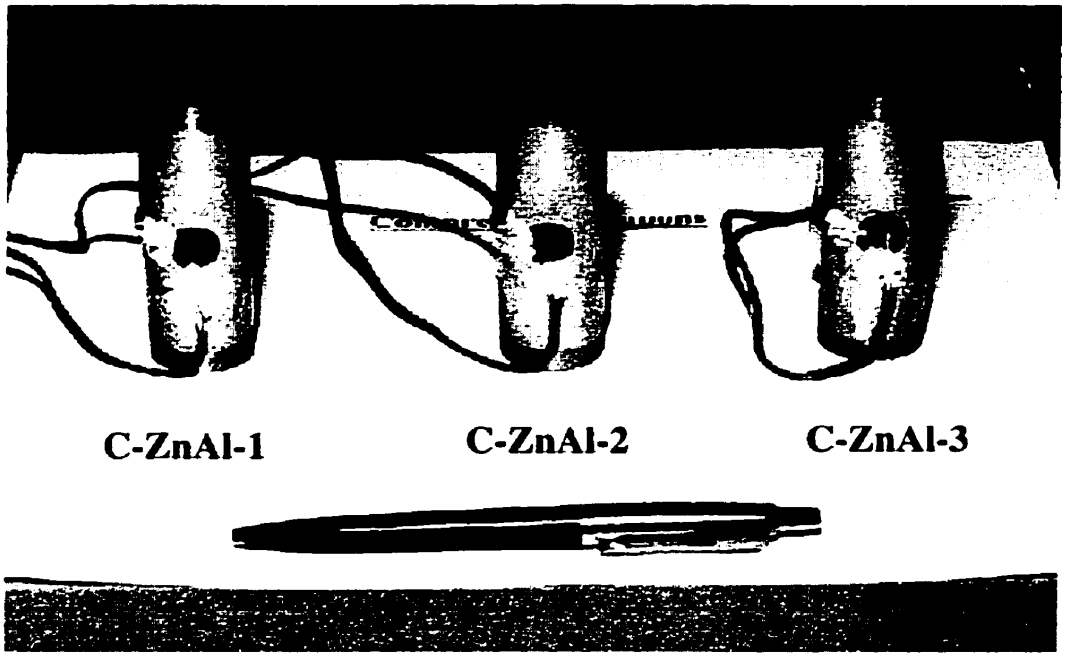

Figure 4-16: Steel specimens spray-coated with Zinc^{85}Aluminum^{15} before testing

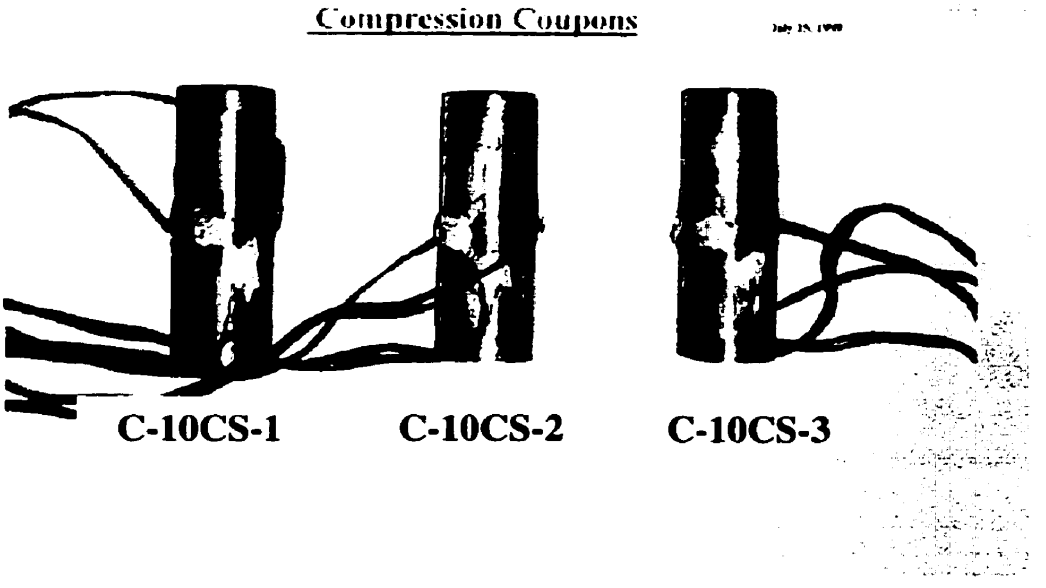

Figure 4-17: Steel specimens spray-coated with 10-carbon steel before testing

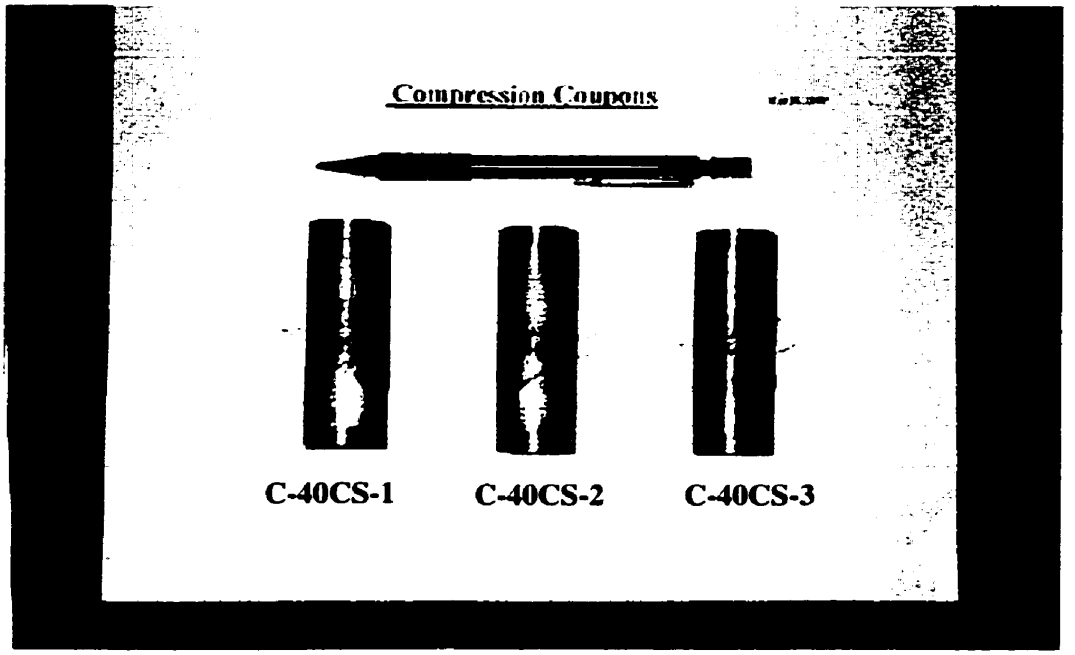

Figure 4-18: Steel specimens spray-coated with 40-carbon steel before testing

The perfectly cylindrical steel specimens used in the phase 2 tests (C-1,2,3) buckled at high loads due to the eccentricity of loading introduced during the testing process. Bi-linear strain gauges were attached on the opposite sides of the cylindrical specimens to measure the strains due to bending. Theoretically, the longitudinal strains on any two opposite sides would be equal for a concentrically loaded specimen. Any strain differential would indicate the degree of eccentricity introduced on the specimen. In this test phase, the strain differential was minimized prior to testing by pre-loading the specimen with a small amount of load and adjusting the location of the specimen. The strains recorded during the testing of the control specimens C-1,2,3 are shown in Figures

4-19 to 4-21. These results show that there was no load eccentricity until the specimen failed.

The control specimens and the spray-coated specimens after testing are shown in Figures 4-22 to 4-26. These figures show that the control specimens and the specimens spray-coated with $Zn^{85}Al^{15}$ material exhibited a ductile behaviour and failed by buckling. The specimens spray-coated with carbon steels exhibited a brittle behavior as they failed by crushing of the spray coating. Figure 4-24 shows the specimens spray-coated with $Zn^{85}Al^{15}$ material. Tension cracks were observed on the coating on one side of the specimens. This side was predominantly in tension near the failure load. The $Zn^{85}Al^{15}$ coating deformed in the same pattern as the steel substrate and was well bonded to the steel substrate after failure. In contrast, both the 10-carbon steel and 40-carbon steel exhibited brittle behavior. The C-10CS and C-40CS specimens, shown in Figures 4-25 and 4-26, failed when the spray material crushed and split in the longitudinal direction. There was no indication of bending or tension cracking on these specimens at failure. The spray coating failed suddenly.

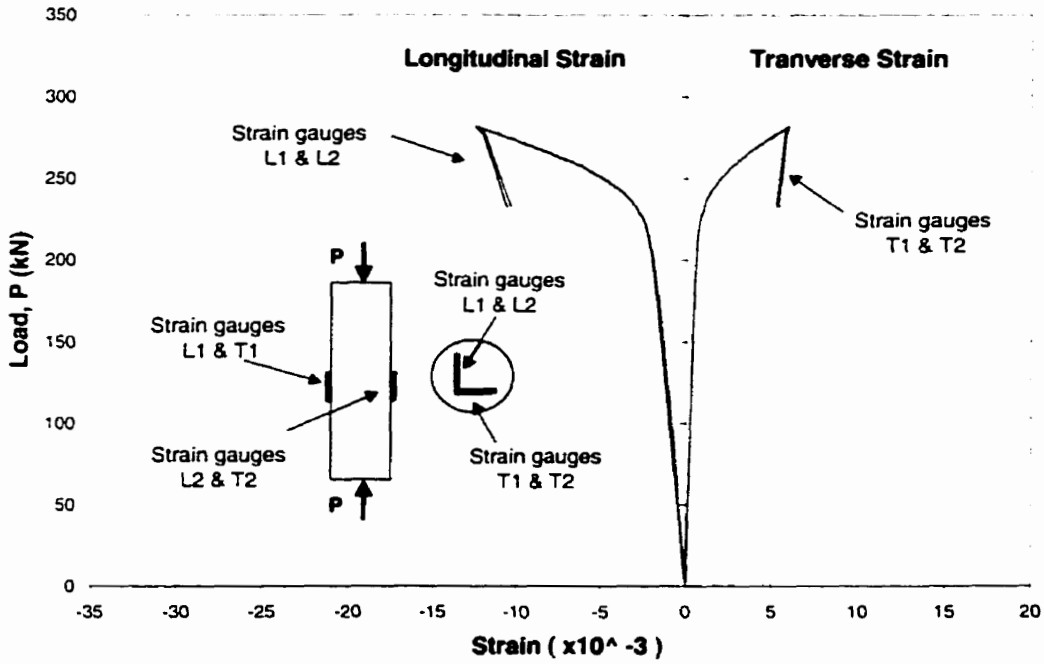

Figure 4-19: Strain readings from specimen C-1

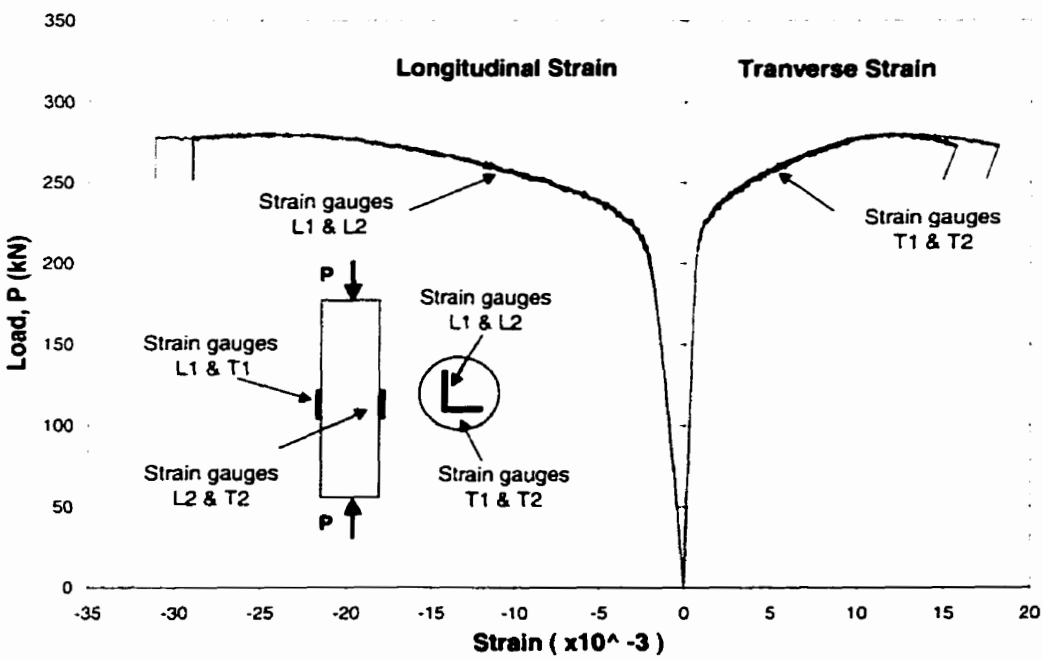

Figure 4-20: Strain readings from specimen C-2

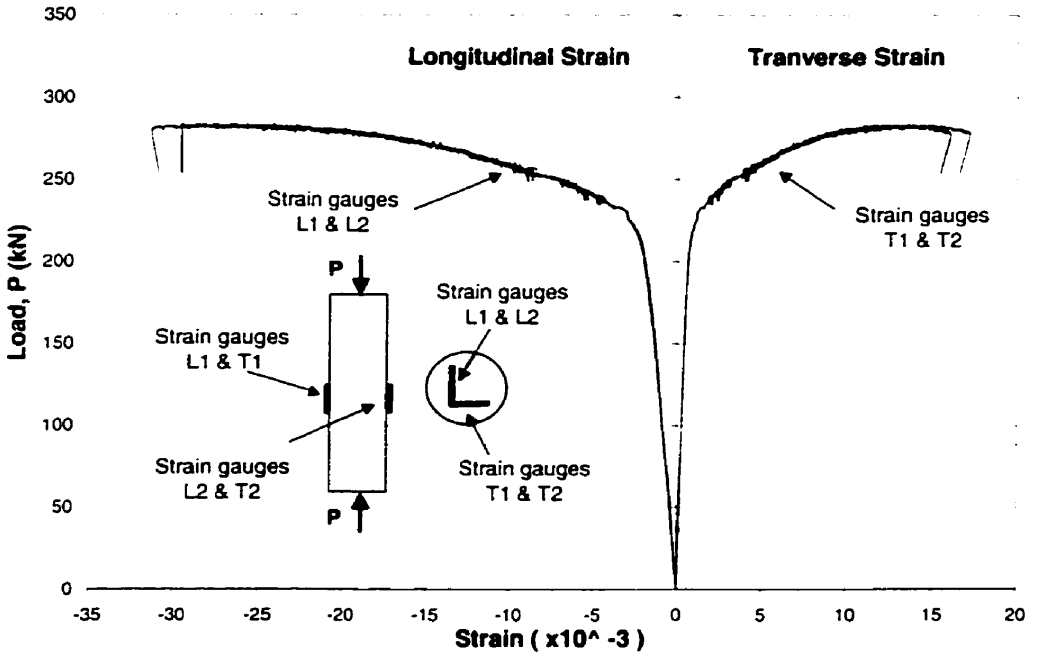

Figure 4-21: Strain readings from specimen C-3

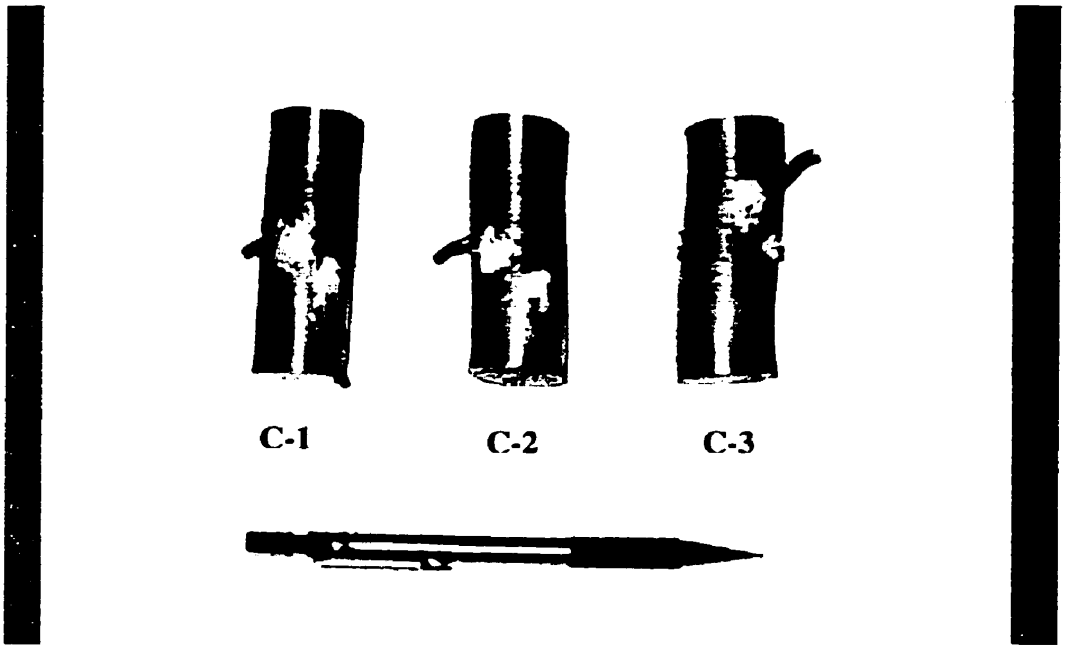

Figure 4-22: Failure mode of cylindrical steel specimens

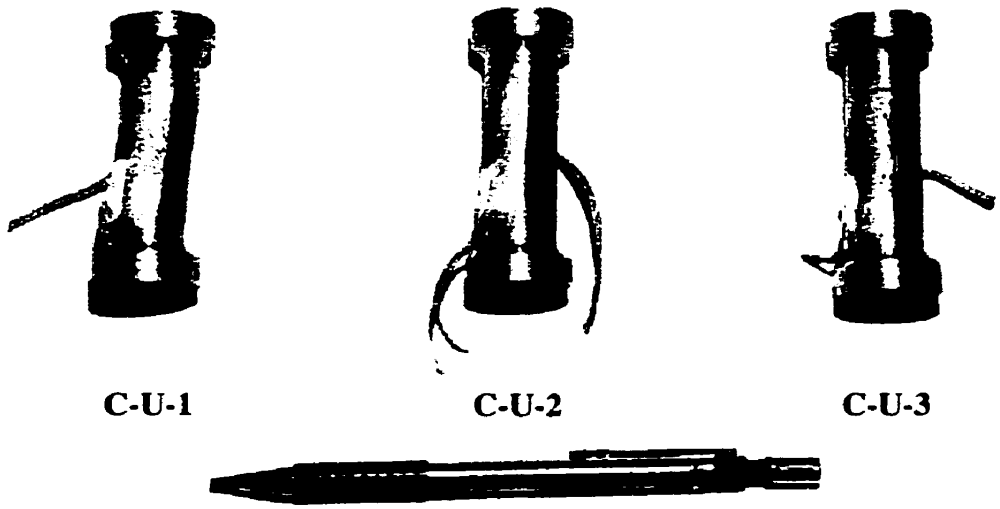

Figure 4-23: Failure mode of uncoated steel specimens

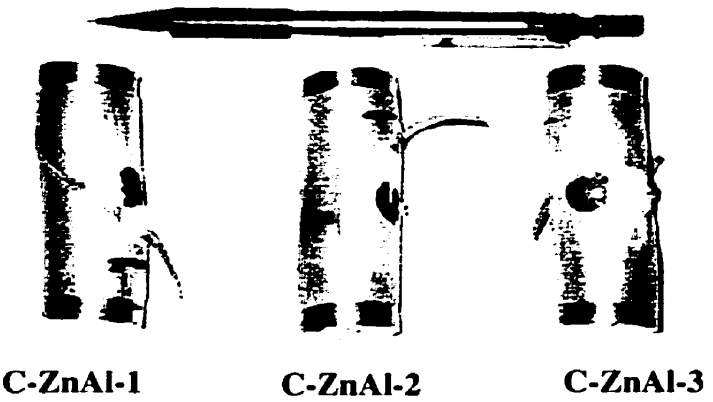

Figure 4-24: Failure mode of specimens coated with Zinc[85]Aluminum[15]

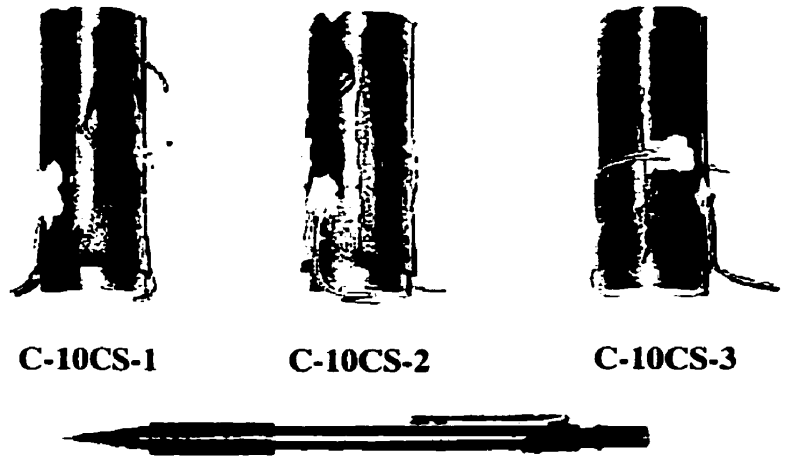

Figure 4-25: Failure mode of specimens coated with 10-carbon steel

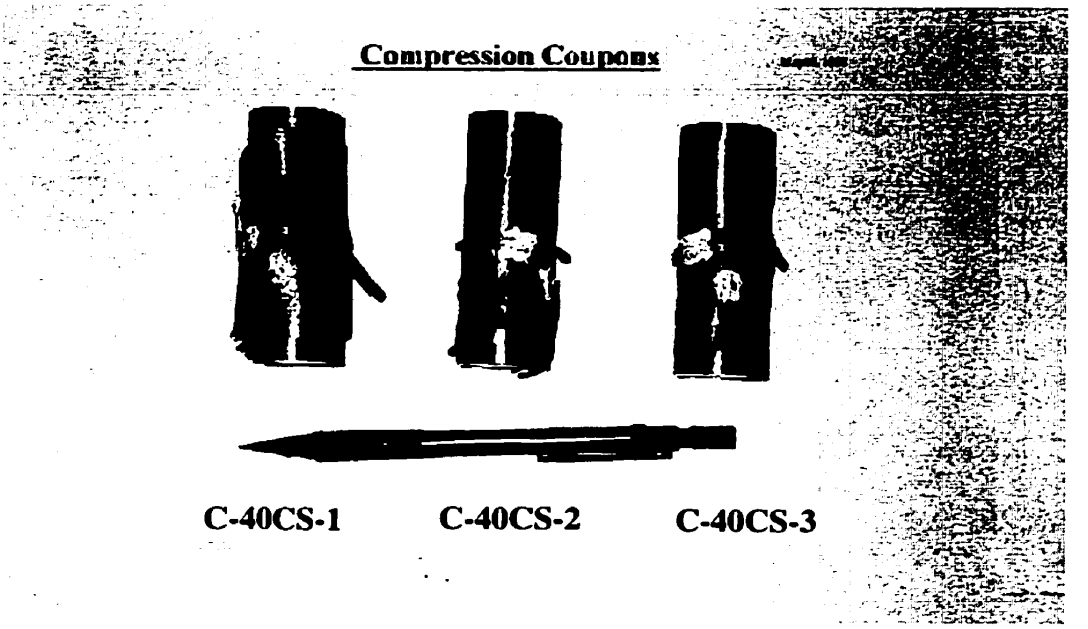

Figure 4-26: Failure mode of specimens coated with 40-carbon steel

The strain results for the repaired specimens are shown in Figures 4-27 to 4-32. The diagrams were plotted in terms of load with respect to strain in order to perform consistent comparisons of the behavior of different types of specimens. Machined (unrepaired) cylindrical specimens C-U-1,2,3 were used to compare the relative strength of the various spray-coated specimens. The results from the uncoated and coated specimens are summarized in Figure 4-33. The steel material chosen for the coating substrate in these specimens was a hardened steel with yield stress of F_y = 460 MPa. This yield stress was determined using the stress-strain curve shown in Figure 4-34 and the 0.2 percent offset technique, as specified by the ASTM standard [32].

The load-strain curves for the spray-coated specimens C-ZnAl, C-10CS, and C-40CS, shown in Figure 3-33, consisted of two, approximately, linear segments. The spray-coated specimens C-10CS and C-40CS had identical load-strain curves at the unset of loading up to failure. The transition point between the two linear axial load-strain segments observed in the spray-coated specimens was probably due to the interface slip of the spray coating from its substrate and its subsequent de-bonding.

The ultimate strength of the uncoated control specimen (C-U-1) shown in Figure 4-33, was 144 kN. This was, approximately, 50 percent of the strength of the perfect cylindrical steel specimen (C-2) which failed at 275 kN. The test results show that the ultimate strength for the repaired specimen C-ZnAl-1 was 210 kN. This specimen had the lowest strength compared to the other spray-coated specimens. Its ultimate strength was 46 percent higher than the uncoated specimen and 76 percent of the

ultimate strength of the cylindrical (control) specimen (C-2). The ultimate strength of the repaired specimens C-10CS-1 and C-40CS-1 was, approximately, 306 kN. The ultimate strength of these specimens was 113 percent higher than the uncoated specimen (C-U-1) and 11 percent higher than the ultimate strength of the cylindrical specimen (C-2). Based on these test results, the carbon steel materials were chosen as the repair materials for the steel angle specimens tested in Phase 3.

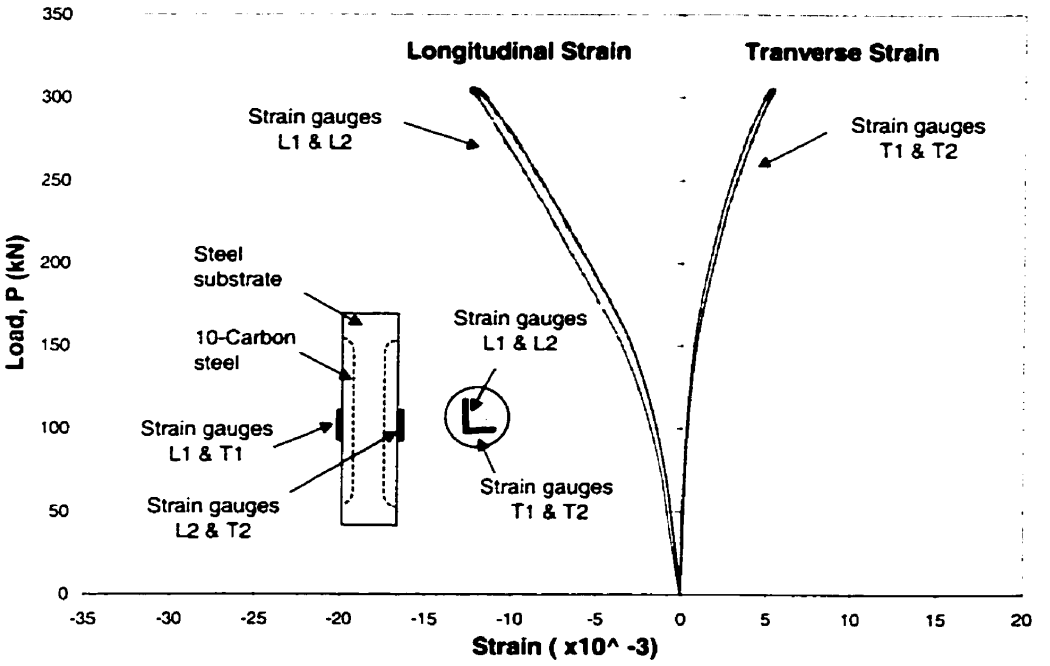

Figure 4-27: Strain readings for specimen C-10CS-1

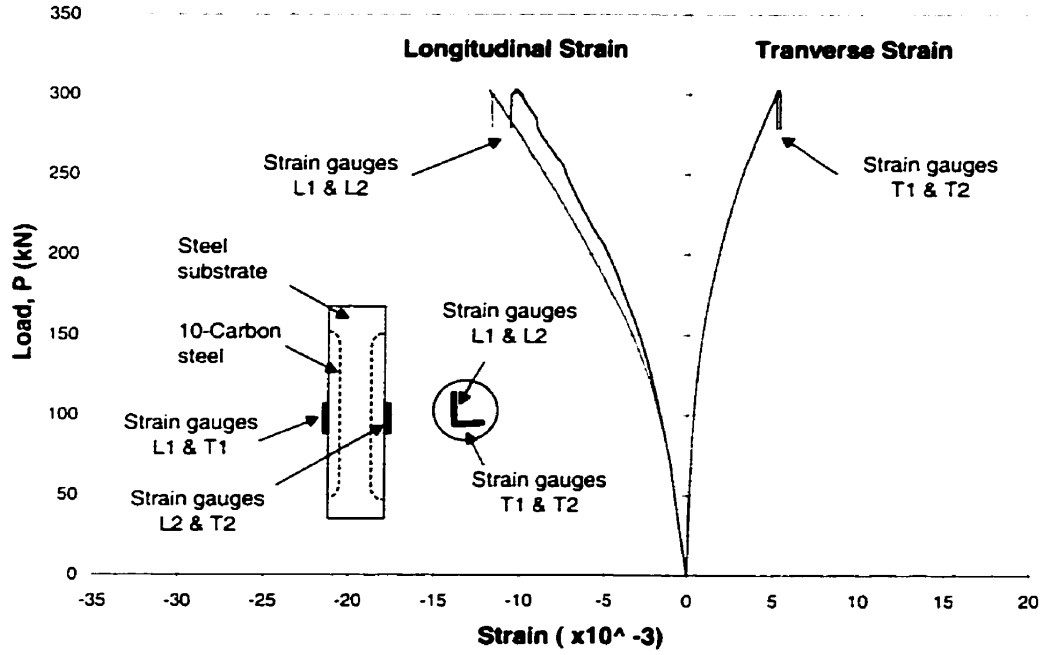

Figure 4-28: Strain readings for specimen C-10CS-2

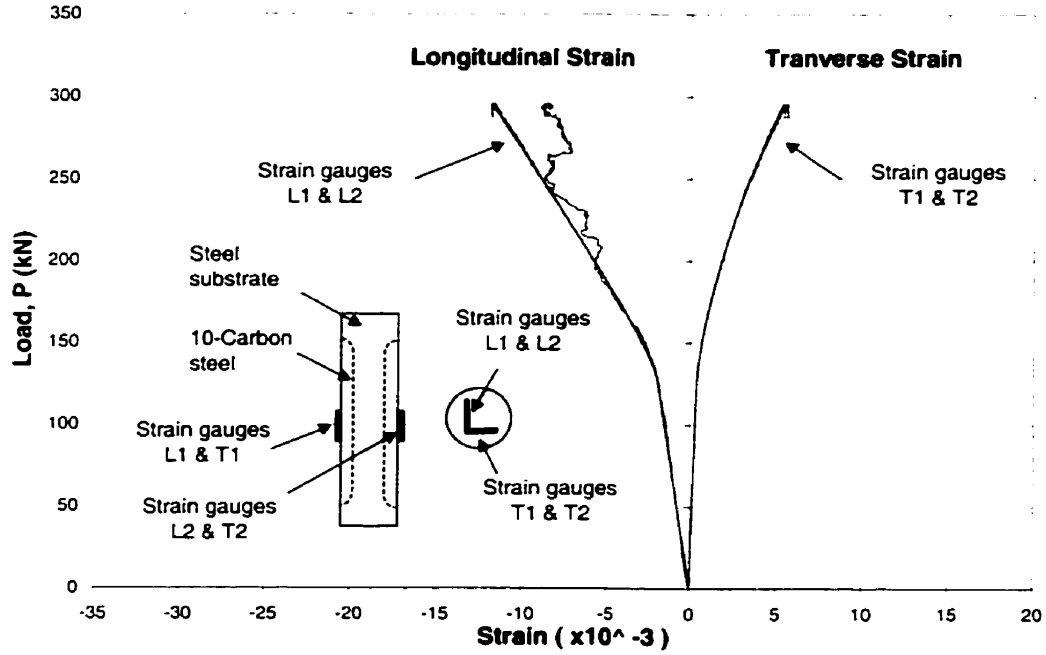

Figure 4-29: Strain readings for specimen C-10CS-3

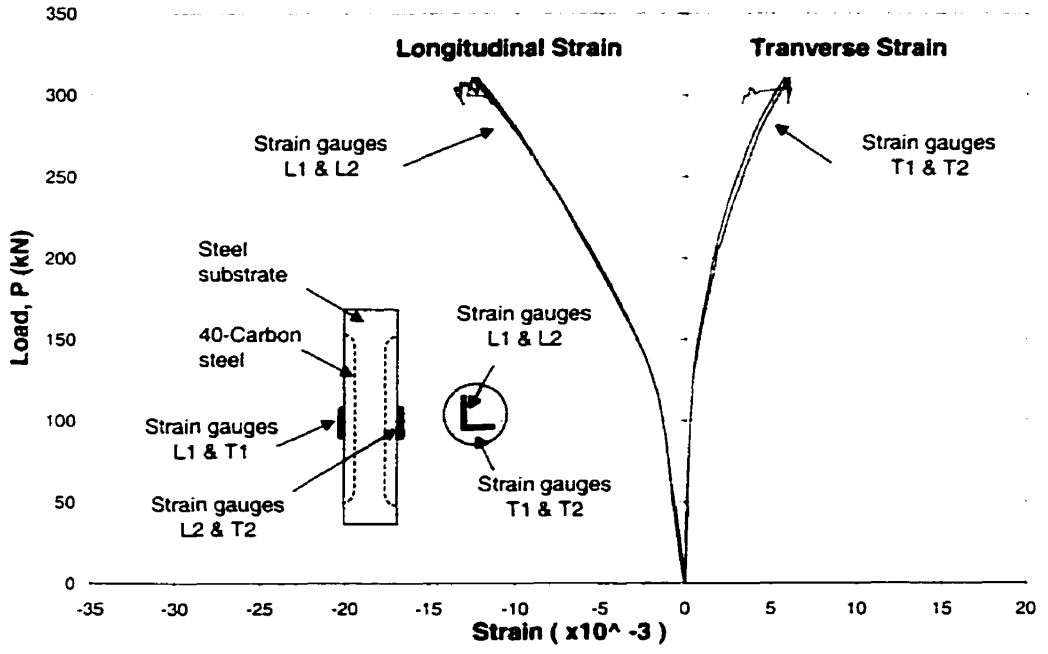

Figure 4-30: Strain readings for specimen C-40CS-1

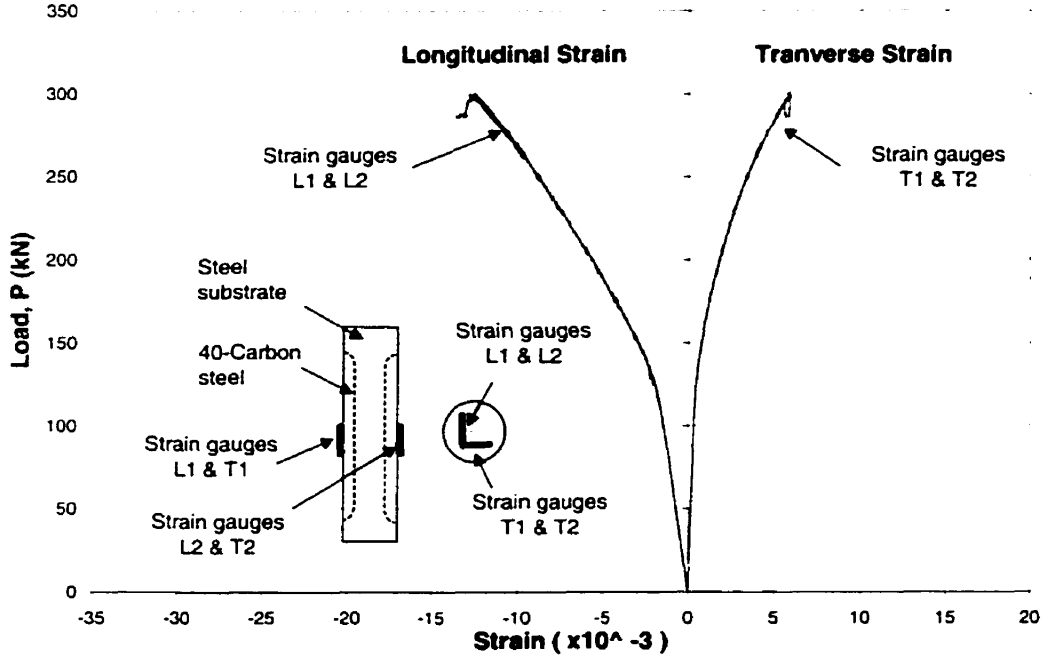

Figure 4-31: Strain readings for specimen C-40CS-2

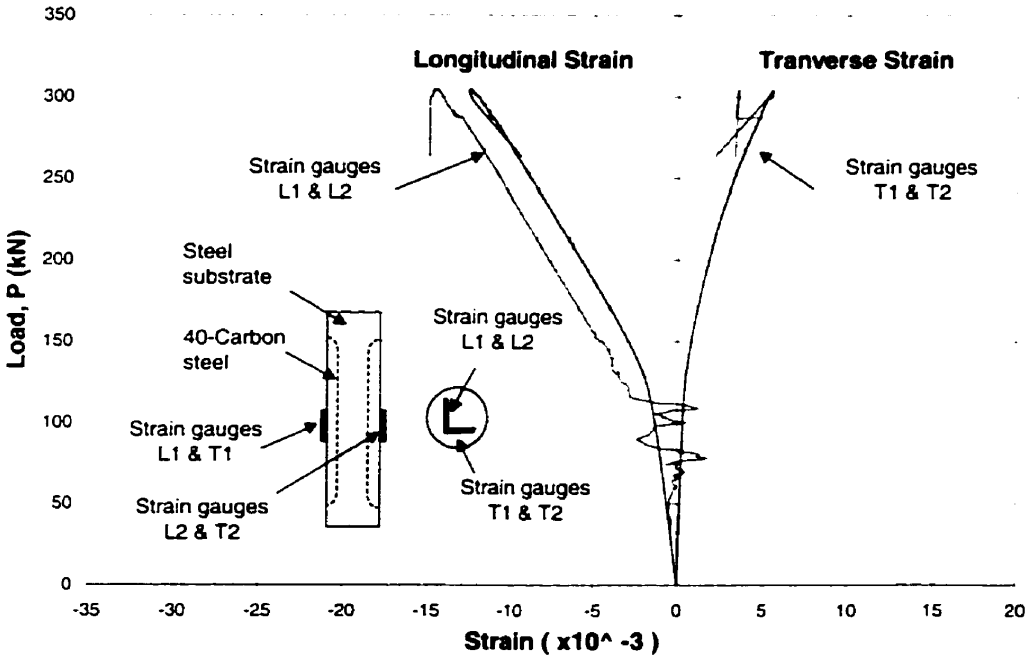

Figure 4-32: Strain readings for specimen C-40CS-3

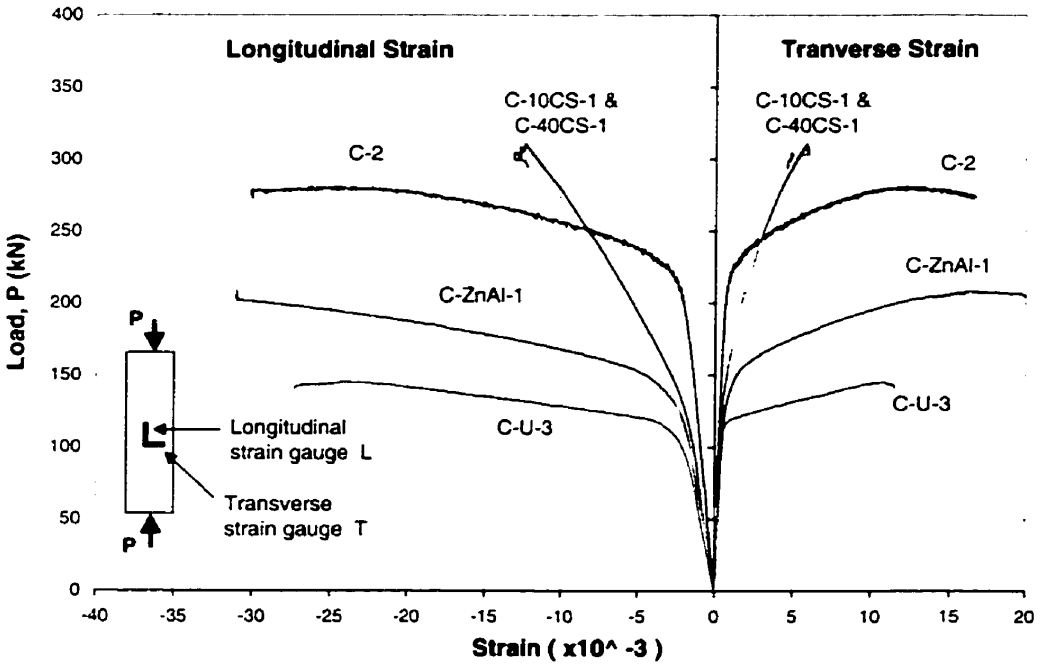

Figure 4-33: Load-strain curves for coated and uncoated specimens tested under compression

4.3.1 Strength of Spray Materials

An indirect method was used to determine the stress-strain behavior of the spray materials tested in Phase 2. The stress-strain behavior of both the steel substrate and the spray material was investigated by determining the total stress resisted separately by the steel and by the spray material. The stress resisted by the steel material, used as the substrate, was computed using the sectional properties and the strain data corresponding to the control specimens (C-1,2,3). A stress-strain relationship was developed using the Ramberg-Osgood equation given by equation Eq. 4-1 [33]. This equation can simplify the stress-strain diagram so that the relation between $\varepsilon/\varepsilon_o$ and σ/σ_o for a variety of materials is expressed by the exponent "n". The terms σ and ε in Eq. 4-1 are the stress and strain in the material and, σ_o and ε_o are shown in Figure 4-34.

$$\frac{\varepsilon}{\varepsilon_0} = \frac{\sigma}{\sigma_0} + \frac{3}{7}\left(\frac{\sigma}{\sigma_0}\right)^n$$

..... **Eq. 4-1**

The exponent "n" was found using the following method: First, the stress-strain curve for the cylindrical specimen C-2 was plotted, as shown in Figure 4-34. Then, the tangent modulus of E = 200 000 MPa, along with the secant modulus corresponding to $E_s = 0.7E$, were drawn on the diagram. The stress corresponding to the intersection of E_s and the stress-strain curve is the base value σ_o. The strain corresponding to the intersection of E and the base stress σ_o is the base strain ε_o. The computed base values of ε_o and σ_o, shown in Figure 4-34, were 0.0022 and 446 MPa, respectively. These base values were

substituted into Eq. 4-1 to compute the value of the exponent "n" for the steel material used in Phase 2. An exponent value of n=17 matched perfectly the stress-strain curve of the control specimen. The final equation was used to compute the stress of the steel substrate in the spray-coated specimens using the recorded strain. The load corresponding to that strain was obtained by multiplying the stress by the cross-sectional area. The stress in the spray coating was obtained by dividing the remaining load corresponding to that strain with the coating's cross-sectional area. The stress-strain curves for the various coatings are shown in Figure 4-35.

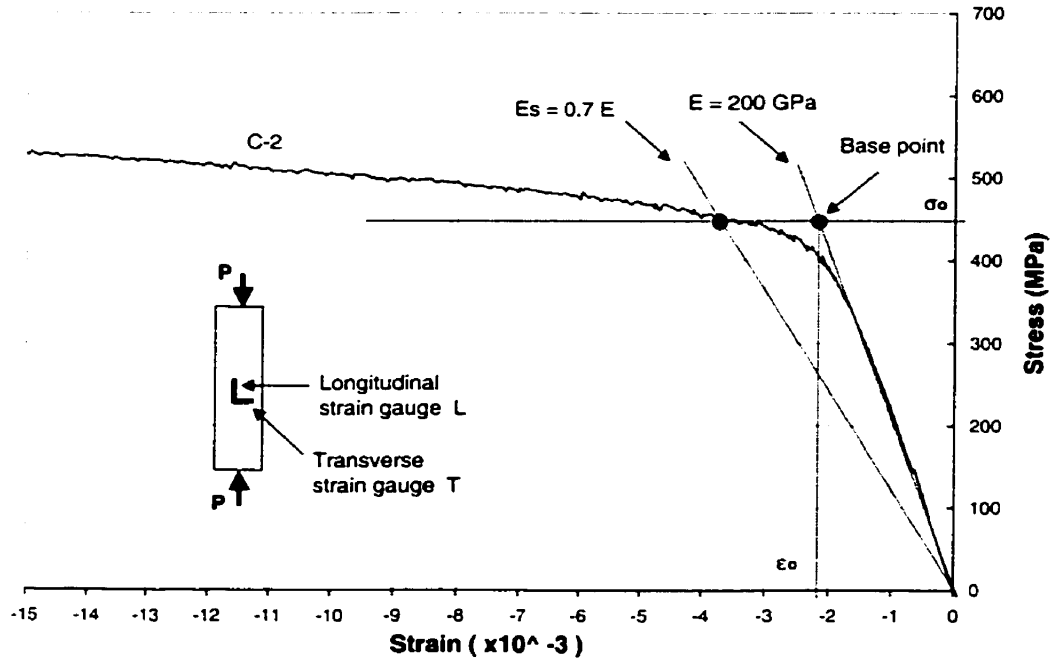

Figure 4-34: Stress-strain curve of steel material used to calculate the base values in the Ramberg-Osgood equation [E1]

The stress-strain curves for the 10-carbon steel and for the 40-carbon steels show that they are the most brittle materials among the coating materials and their modulus of elasticity is much lower than that of the steel substrate. The $Zn^{85}Al^{15}$ alloy was a ductile material with lower ultimate strength than that of carbon steels. The kinks in the curve of carbon steels correspond to the de-bonding of the spray coating from the steel substrate.

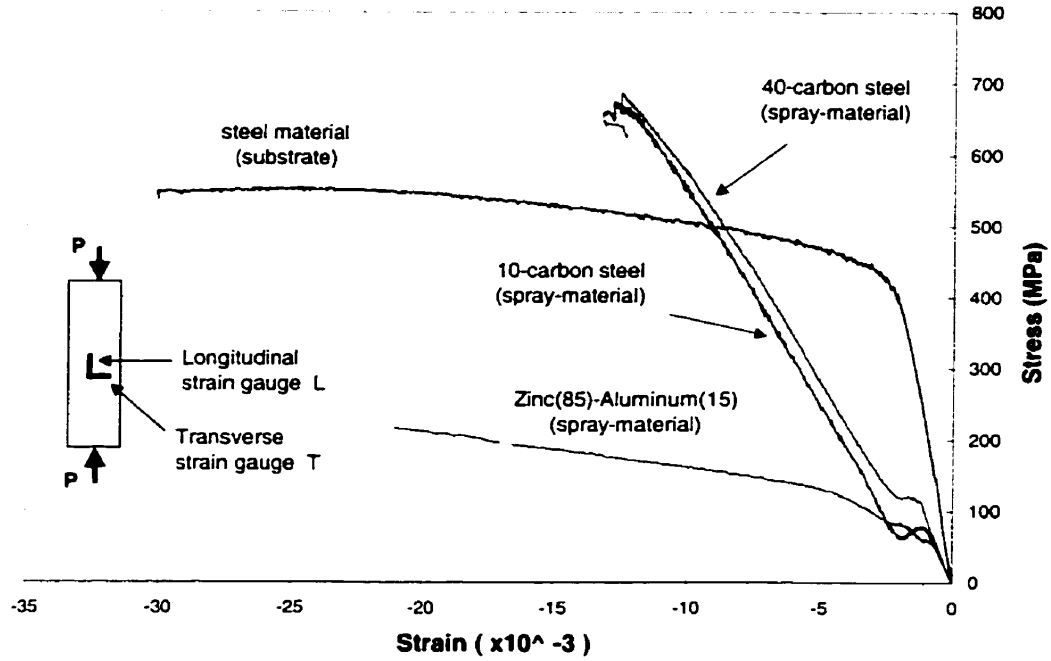

Figure 4-35: Comparison of stress-strain curves between steel and spray coating

Since the spray coating of these specimens was in a confined condition, the carbon steel coated specimens were still resisting the applied loads after de-bonding of the spray coating from the steel substrate up to the failure. In a confined condition, the

spray coating of $Zn^{85}Al^{15}$ alloy achieved an ultimate stress of 217 MPa, which is only 40% of the ultimate stress of the steel (550 MPa). The 10-carbon steel and 40-carbon steel have the same ultimate stress level of 680 MPa, which is 124% of the steel strength.

4.4 Phase 3: Static Compression Test on Steel Angle Specimens

Two groups of steel angle specimens were tested to investigate the ability of the spray materials to repair steel angle specimens. Each group of specimens consisted of seven angles cut from two 6-m long pieces. 10-carbon steel and 40-carbon steel were used as the repair materials in this phase. In each group, one perfect angle section was used as the control specimen and six sections were machined to simulate different corrosion patterns.

The data recorded during the tests included stroke displacements and strains. These data, along with visual observations, were used to determine if the repaired materials improved the strength of the steel angles. 10-carbon steel and 40-carbon steel were chosen as the repair materials not only because of their high strength, but also because they were relatively easy to obtain at a lower cost compared to other metallic materials.

A perfect steel angle specimen is shown in its test set-up in Figure 4-36. Two bi-linear strain gauges were attached on both legs of the specimen L1. The strains recorded during the testing of the perfect steel angle (L1) are shown in Figure 4-37.

These results show that there was no load eccentricity on the angle section. The specimens repaired with 10-carbon steel are shown in Figures 4-38 to 4-43 while those repaired with 40-Carbon steel are shown in Figures 4-44 to 4-47. The ultimate loads for all specimens are listed in Tables 4-2 and 4-3. The ratio of the ultimate strength of the specimens-to-the ultimate strength of the perfect angle specimens are also given in these tables and are shown in bar graphs in Figures 4-48 and 4-49.

The angle specimens failed by either buckling or separation of the spray material. Twisting was observed in the perfect steel angle once buckling failure had occurred. The unrepaired specimen L1-OU, shown in Figure 4-41, failed by local buckling at the edge of the circular hole simulating the defect due to corrosion. The same figure also shows that the repaired specimen, L1-OR-10CS, failed by crushing of the spray material. At failure, the crushed spray material was peeled off. Local buckling was also the governing failure mode in specimen L1-EU, as shown in Figure 4-42. It took place at the edge of the elliptical defect where a high concentrated stress was located. The repaired specimen, L1-ER-10CS, failed the same way as the perfect specimen by twisting. Local buckling occurred in the repaired leg and several tension cracks due to the bending deformation were observed on the surface of spray material. Specimen L1-EOR-10CS, shown in Figure 4-43, shows the spray material crushed at the circular hole location.

Group II specimens were repaired by the 40-carbon steel spray material. The unrepaired specimens in group II had, approximately, the same strength and failure modes as their counter parts in group I. However, the failure mode of the specimens

repaired with 40-carbon material was different than those specimens repaired with 10-carbon steel material. Figure 4-44 shows the failure of the L2-OR-40CS specimen caused by crushing of the spray material. Crushing of the spray material in this specimen was more serious than that of the L1-OR-10CS specimen. This result indicates that the 40-carbon steel material is more brittle than the 10-carbon steel material. A difference in the failure mode was also observed in specimens L2-ER-40CS and L1-ER-10CS, as shown in Figures 4-45 and 4-42, respectively. The L2-ER-40CS specimen failed by local buckling at the edge of the defect after the spray material was de-bonded from the steel substrate, whereas specimen L1-ER-10CS failed by torsional buckling. Figure 4-46 provides a closer view of the failure mode of the repaired L2-ER-40CS specimen, which was due to de-bonding of the spray material from the steel substrate. The L2-EOR-40CS specimen, shown in Figure 4-47, also failed by local buckling after de-bonding of the spray material from the steel substrate. The difference in the failure modes between the specimens repaired with 10-carbon steel and the specimens repaired with 40-carbon steel, indicates that the 10-carbon steel material was less brittle and had a higher bond strength than the 40-carbon steel.

Table 4-2: Ultimate load of angle specimens (group L1)

Specimen Type	Ultimate Load, P_u (kN)	$P_u / P_{u(L1)}$
L1	210	1.00
L1-OU	120	0.57
L1-OR-10CS	187	0.89
L1-EU	96	0.46
L1-ER-10CS	198	0.94
L1-EOU	78	0.37
L1-EOR-10CS	203	0.97

Table 4-3: Ultimate load of angle specimens (group L2)

Specimen type	Ultimate Load, P_u (kN)	$P_u / P_{u(L2)}$
L2	225	1.00
L2-OU	130	0.58
L2-OR-10CS	175	0.78
L2-EU	102	0.45
L2-ER-10CS	195	0.87
L2-EOU	81	0.36
L2-EOR-10CS	178	0.79

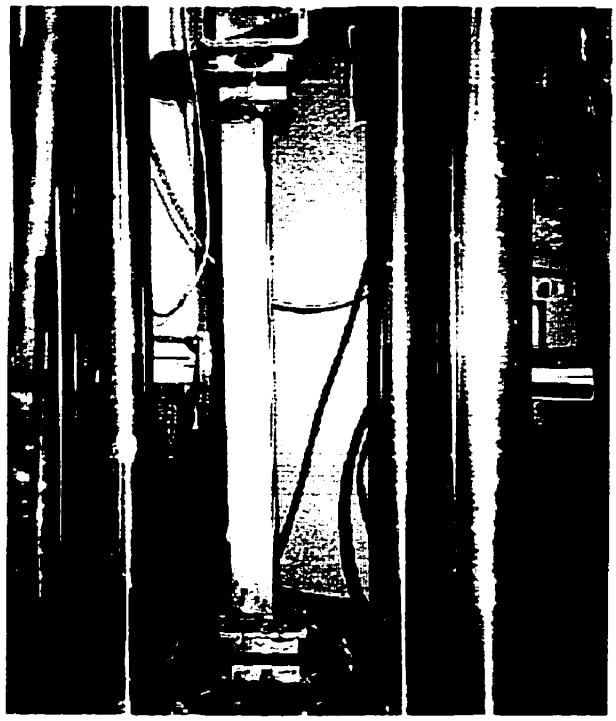

Figure 4-36: Test set-up and specimen L1 in place before testing

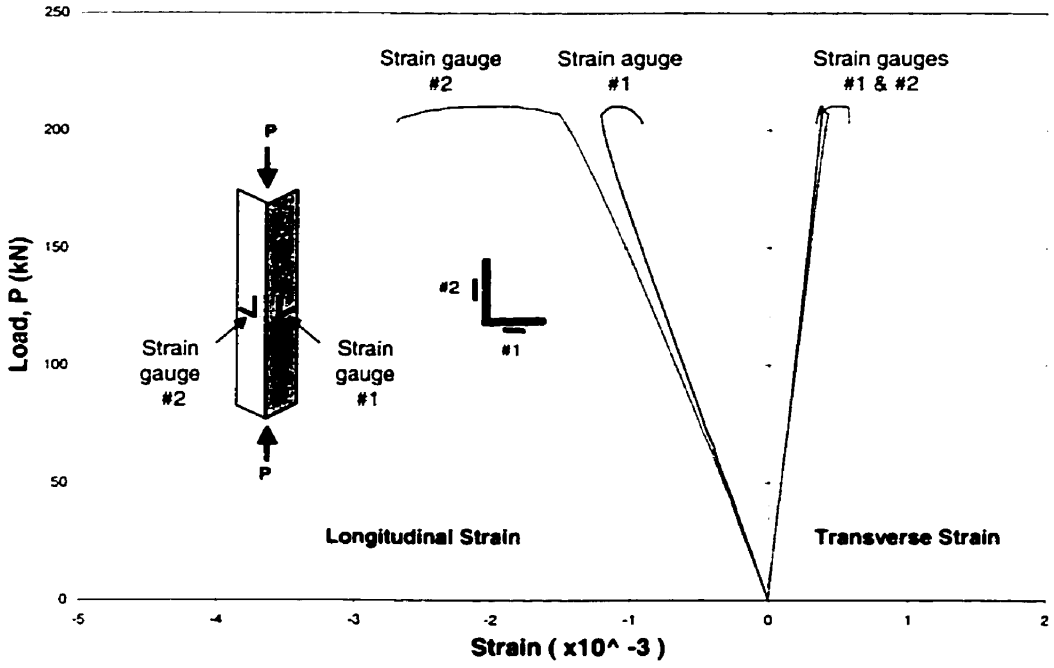

Figure 4-37: Strain readings for specimen L1 indicate that the concentric load was applied

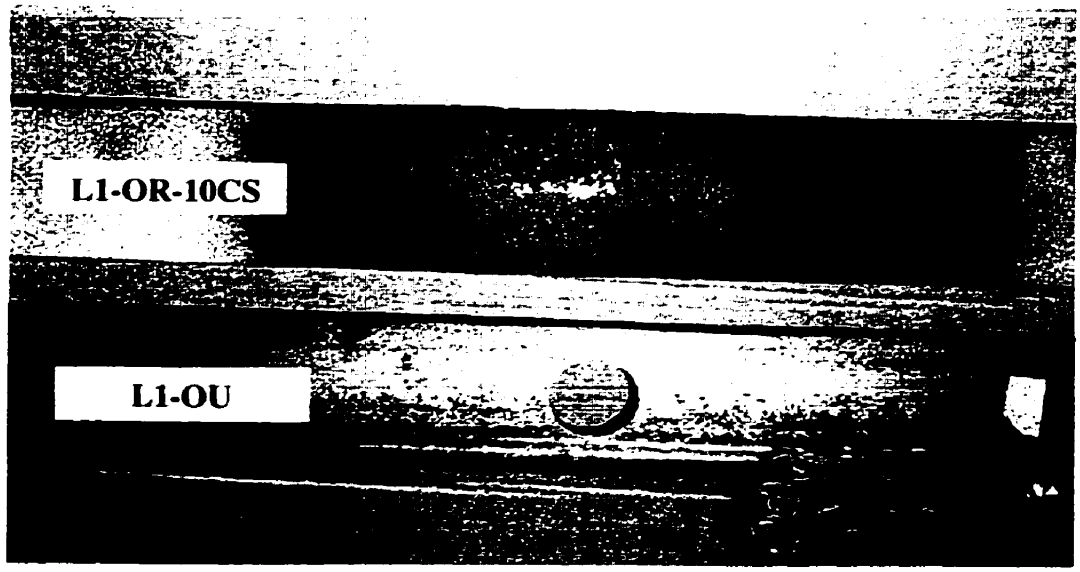

Figure 4-38: Specimens L1-OU and L1-OR-10CS before testing

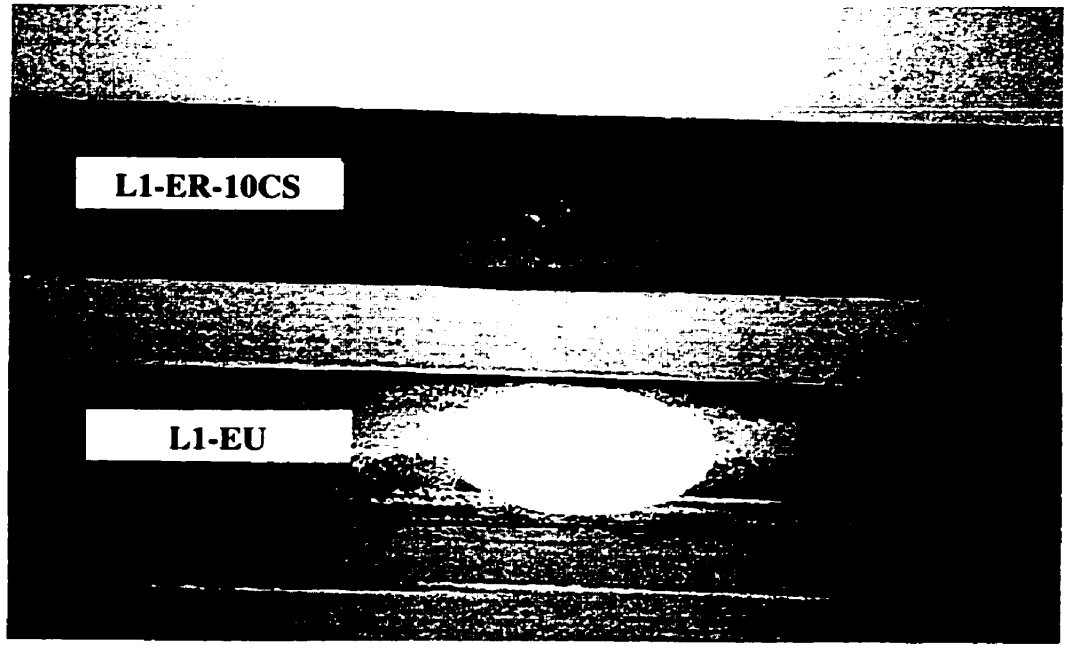

Figure 4-39: Specimens L1-EU and L1-ER-10CS before testing

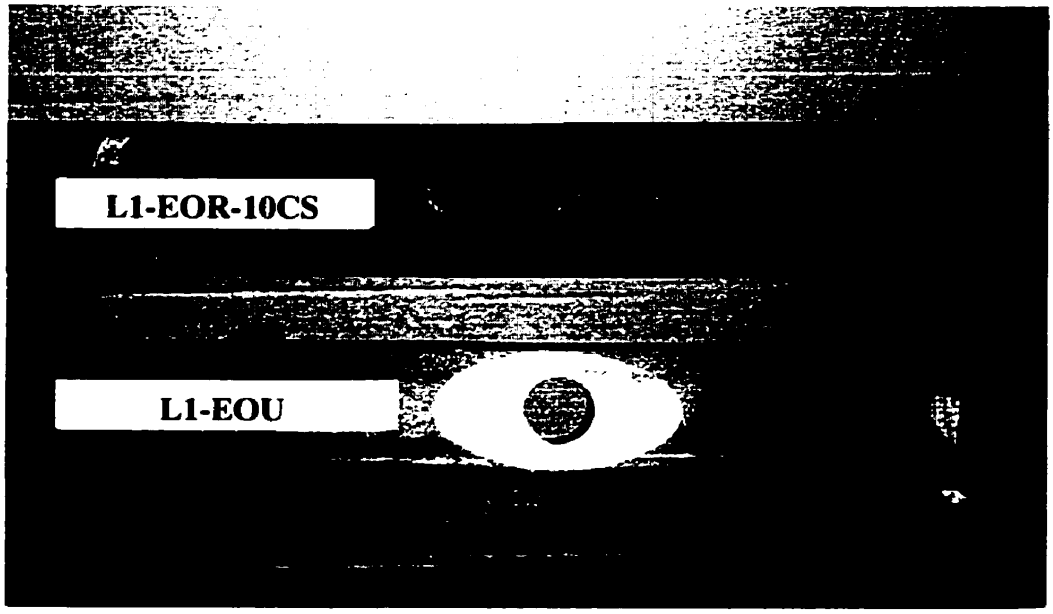

Figure 4-40: Specimens L1-EOU and L1-EOR-10CS before testing

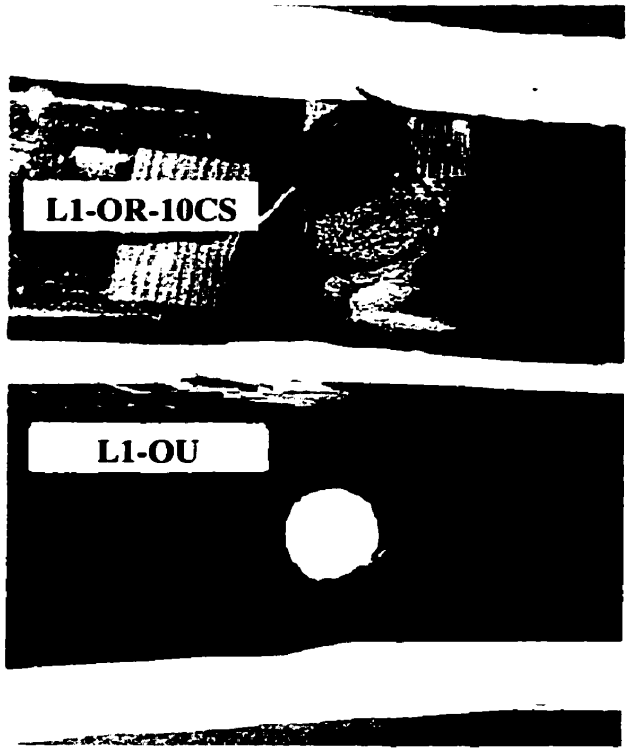

Figure 4-41: Failure mode of specimens L1-OR-10CS and L1-OU

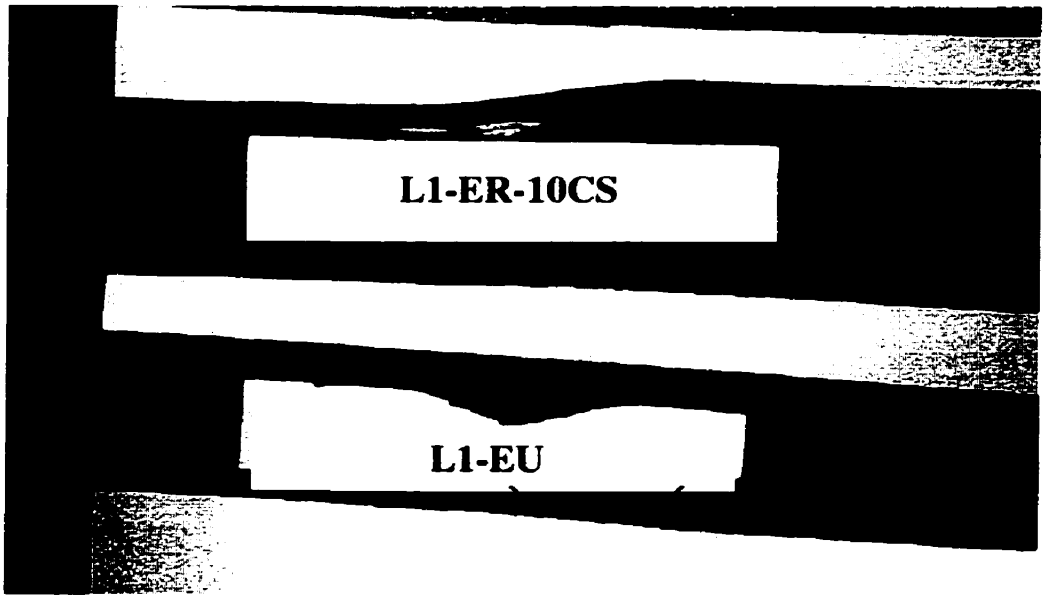

Figure 4-42: Failure mode of specimens L1-ER-10CS and L1-EU

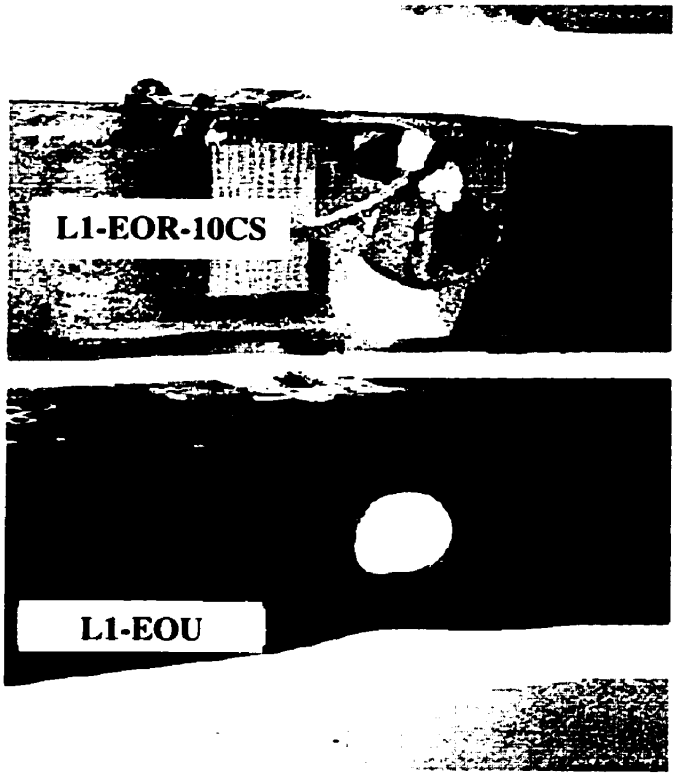

Figure 4-43: Failure mode of specimens L1-ER-10CS and L1-EU

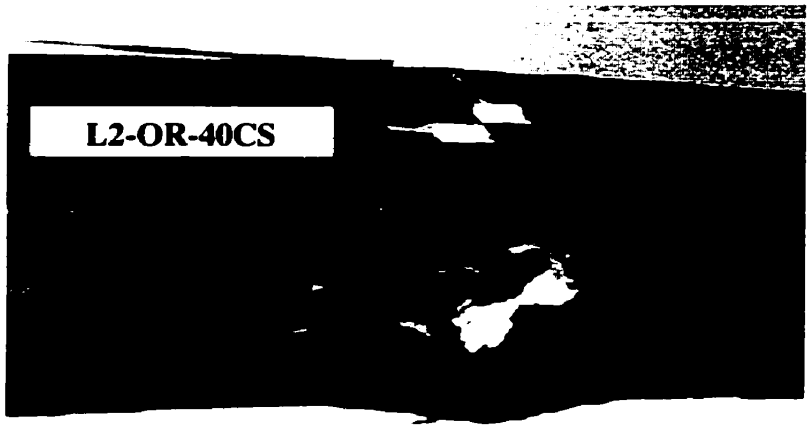

Figure 4-44: Failure mode of specimen L2-OR-40CS

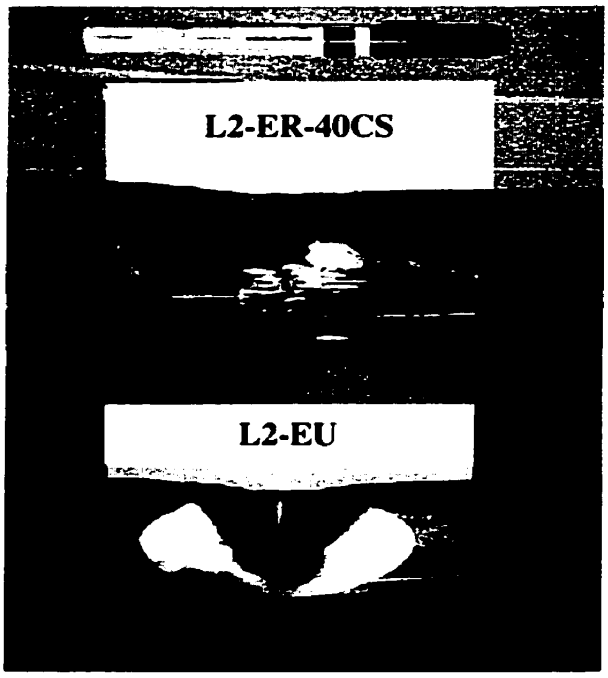

Figure 4-45: Failure mode of specimens L2-ER-40CS and L2-EU

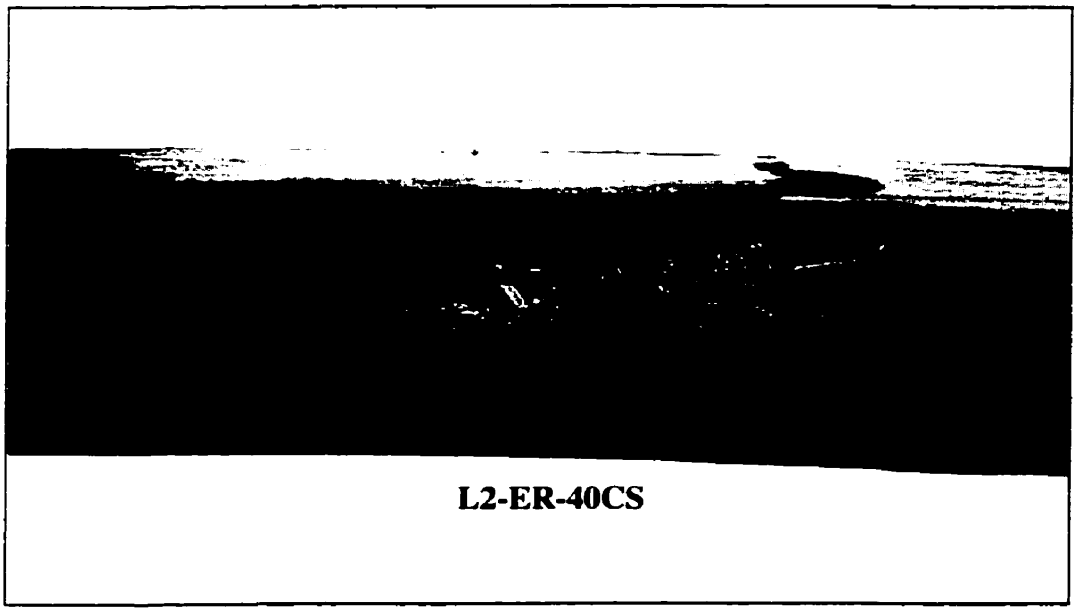

Figure 4-46: A close-up of the failure mode of specimen L2-ER-40CS

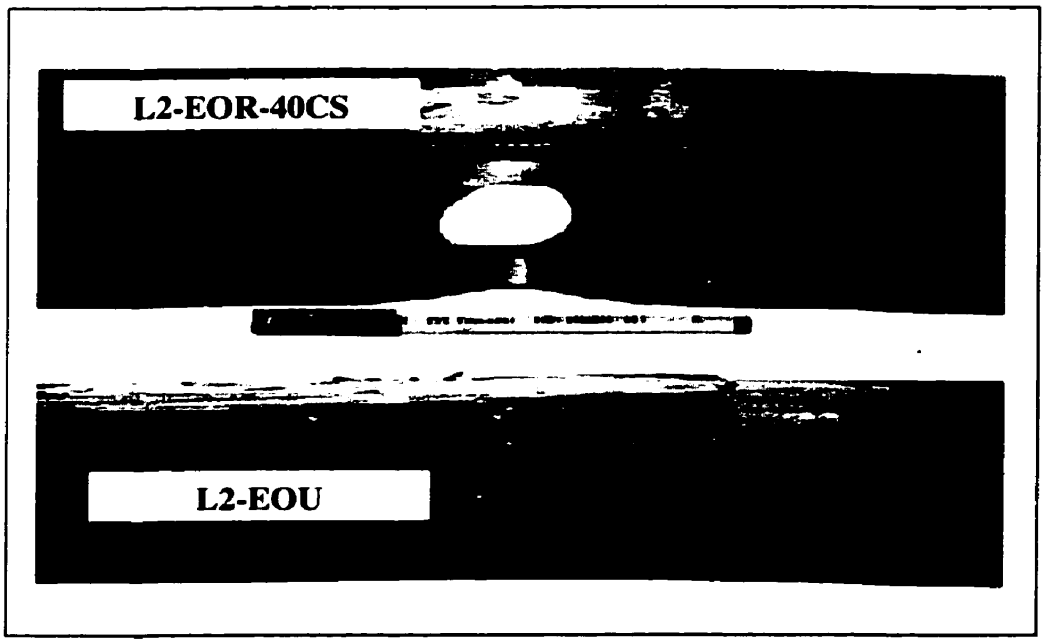

Figure 4-47: Failure mode of specimens L2-EOR-40CS and L2-EOU

The ultimate strength of the specimens in both groups I and II are shown in the histograms of Figures 4-48 and 4-49 respectively. The results indicate that repair materials 10-carbon steel and 40-carbon steel improved the strength of the unrepaired specimens considerably. The ultimate strength of the unrepaired specimen L1-OU was 120 kN. It increased by 56% to 187 kN after it was repaired with 10-carbon steel. This repaired specimen achieved 89% of the strength of the perfect angle specimen. The strength of the repaired specimen L1-ER-10CS increased from 96 kN to 198 kN after repair (an increase of 106%). The ultimate strength of this repaired specimen was 94% of the strength of the perfect angle specimen. An even greater improvement was observed in specimen L1-EOU. The strength of the repaired specimen L1-EOR-10CS increased by 160% from 78 kN to 203 kN. In fact, the strength of the repaired specimen was 97% of the strength of the perfect angle specimen.

The specimens repaired using 40-carbon steel also showed a good improvement in strength. However, the specimens repaired with 40-carbon steel achieved a lower increase in strength than the specimens repaired with 10-carbon steel. The strength improvement of these specimens varied from 78% to 87% of the perfect specimen strength. This was due to the brittle nature of 40-carbon steel material which failed prematurely by de-bonding. The repaired specimens of L2-OR-40CS and L2-EOR-40CS were able to achieve 78% and 79% of the perfect specimen strength, respectively. The L2-ER-40CS specimen reached 87% of the strength of the perfect angle specimen.

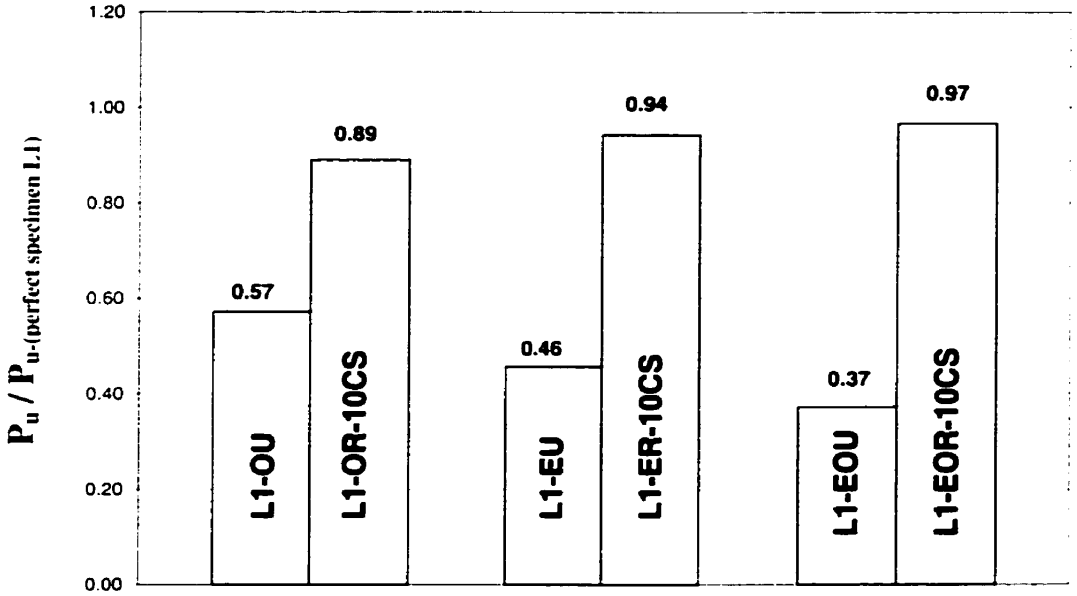

Figure 4-48: Ultimate strength of specimens L1 repaired with 10-carbon steel material

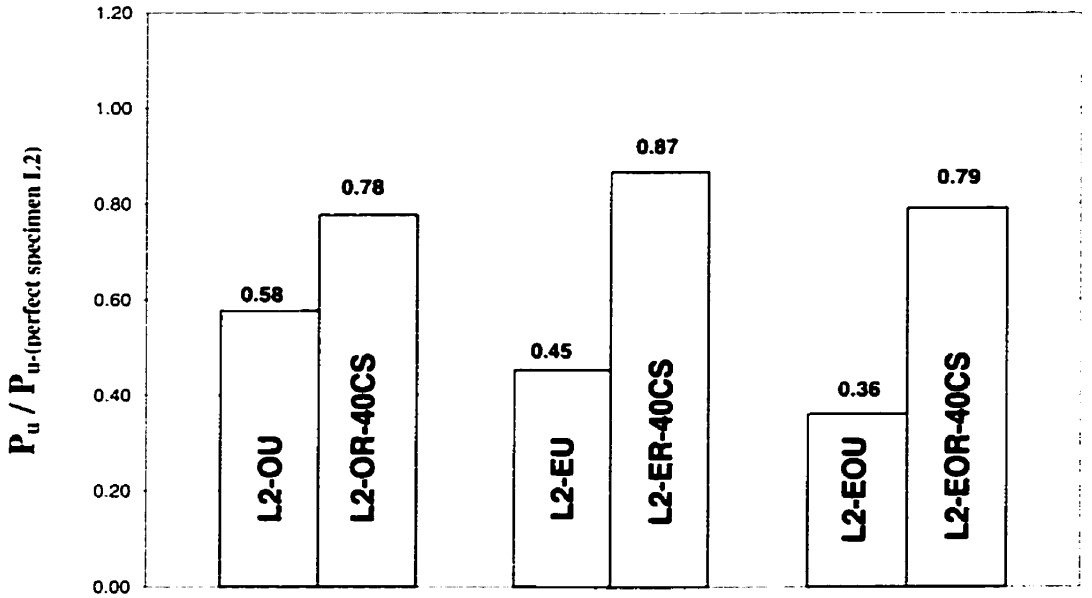

Figure 4-49: Ultimate strength of specimens L2 repaired with 40-carbon steel material

4.4.1 Load-Stroke Diagrams

The load-stroke curves of the angle specimens in the two groups are shown in Figure 4-50 and 4-51. A well repaired specimens should have a similar load-stroke curve as the perfect angle specimen. The repaired material is considered ideal when the displacement pattern of the repaired specimen is nearly identical to that of the perfect angle specimen. This enables an engineer to predict the displacement of a repaired section correctly after repairing it with spray material. The results indicate that the stiffness of both repaired and unrepaired specimens was almost the same as that of the perfect angle section. The angle specimens repaired with 10-carbon steel had minimum and maximum stroke displacements of 91% and 103% of the stroke displacement of the control specimen L1, respectively. The angle specimens repaired with 40-carbon steel were displaced with the minimum stroke of 93% and the maximum stroke of 99% of that the control specimen L2.

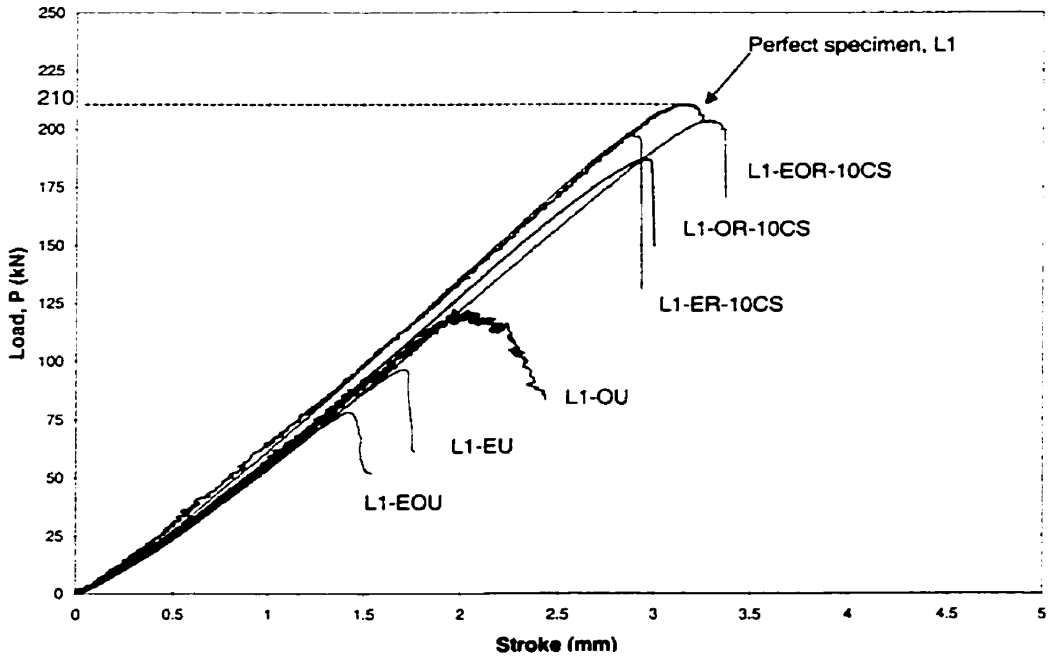

Figure 4-50: Load-stroke curves for specimens repaired with 10-carbon steel material

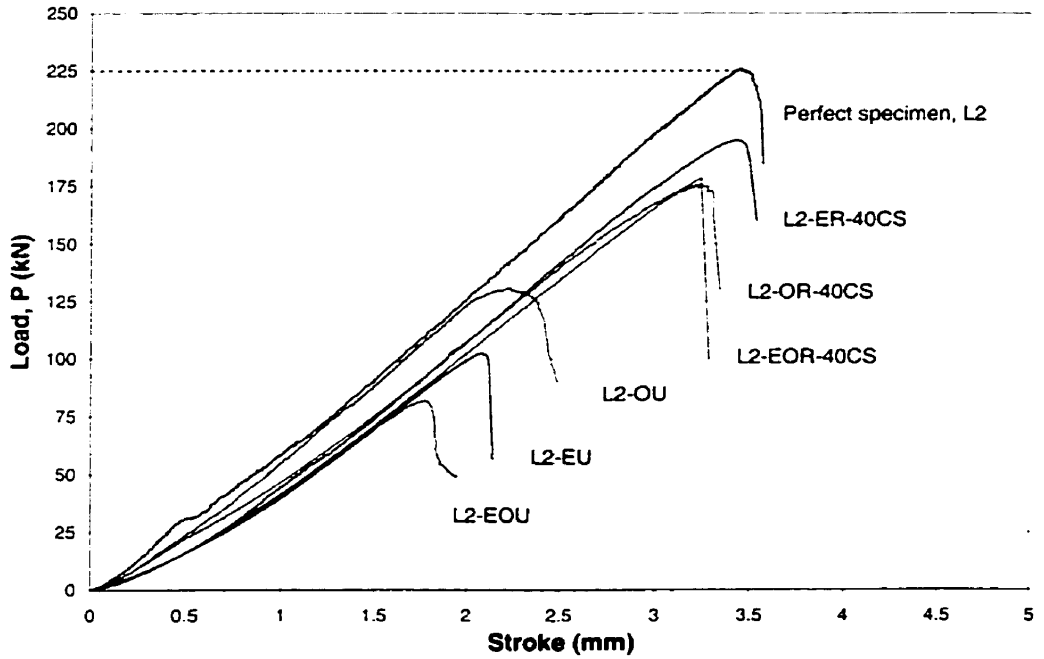

Figure 4-51: Load-stroke curves for specimens repaired with 40-carbon steel material

4.4.2 Load-Strain Curves

To investigate the performance of the spray material, strain gauges were mounted on both legs of the specimens. Load-strain curves for all specimens are plotted in Figures 4-52 and 4-53. The load-strain curves in Figure 4-52, show that the strains in the non-defective leg of group I repaired specimens are almost the same as the strains in the perfect angle specimen. Only small variation in the curves is observed between the repaired and the control specimens at a load range close to buckling failure. This indicates that the performance of 10-carbon steel was good and that this material can

provide sufficient strength to a defective leg to allow uniform distribution of the applied stresses in both legs.

The load-strain curves of the repaired specimens in group II are shown in Figure 4-53. The curves exhibit a larger variation from the reference curve of the perfect specimen. The specimens L2-OR-40CS, L2-ER-40CS, and L2-EOR-40CS that were repaired with 40-carbon steel started to deviate from a linear behavior at a load level of, approximately, 100 kN which is only 44% of the ultimate strength of the control specimen L2. This indicates that local buckling took place at that load level and any subsequent increase in strength was due to post-buckling strength.

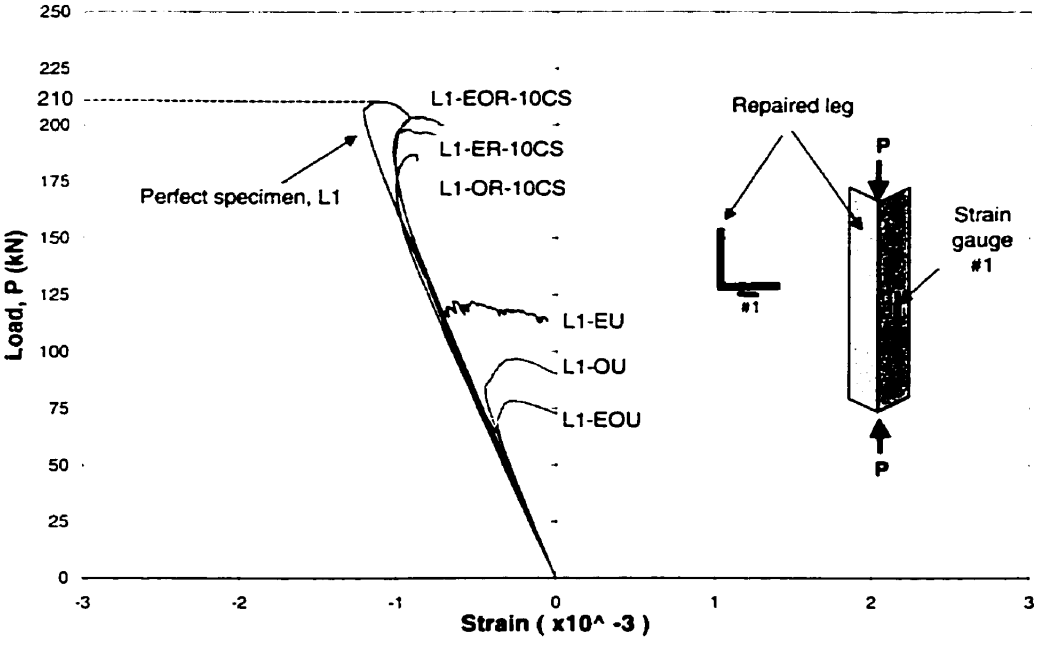

Figure 4-52: Load-strain curves of specimens repaired with 10-carbon steel material

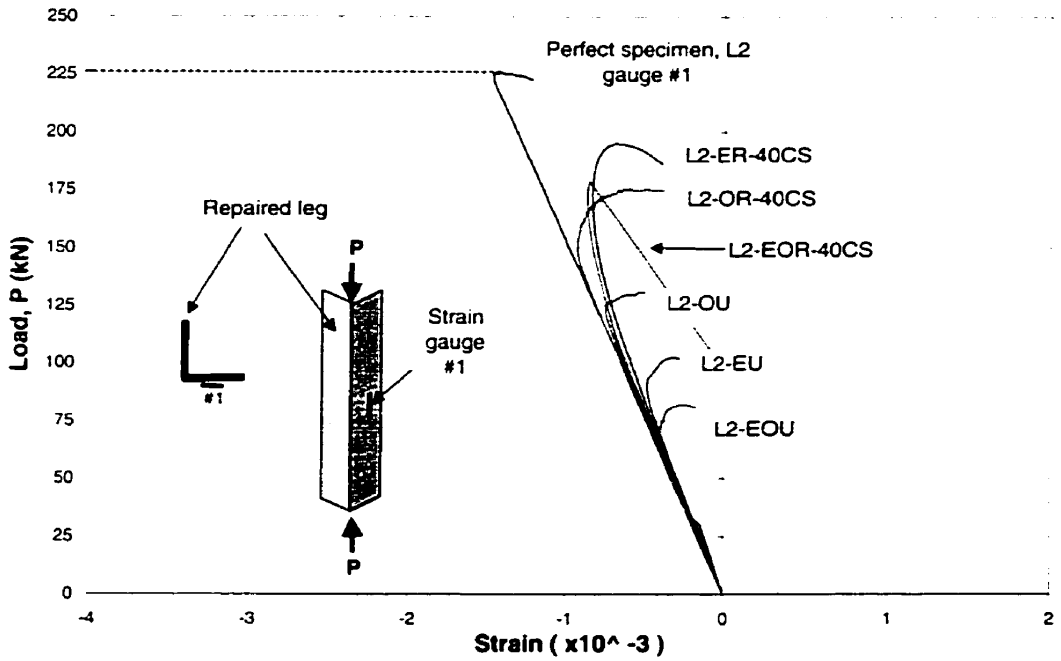

Figure 4-53: Load-strain curves of specimens repaired with 40-carbon steel material

In general, the specimens repaired with the 10-carbon steel material have a more consistent load-strain behavior on both the non-defective and the defective legs. Figures 4-54 to 4-56 show the load-strain curves of specimens L1-OR-10CS, L1-ER-10CS, and L1-EOR-10CS for group I. Strain gauge #1 was mounted on the non-defective leg to measure the longitudinal strain. Two additional strain gauges, #2 and #3, were mounted at mid-height to measure the longitudinal strains on two opposite sides of the defective leg. Strain gauge #2 was used to measure the strain in the repaired material in specimens L1-ER-10CS and L1-EOR-10CS. Strain gauge #3 was used to measure the strain in the

steel material of specimen L1-ER-10CS and the strain in the repaired material of specimen L1-EOR-10CS.

The strain readings from gauge #2 shown in Figures 4-54 to 4-56 indicate that the stiffness of the repaired leg is lower than that of the non-defective leg. However, the repaired material was able to resist an applied load and fail at a load close to the original strength of the perfect specimen. The strain curves also show the load at which local buckling occurred and the ability of the specimens to achieve a post buckling failure, mainly through stress redistribution. At ultimate stress, the repaired material failed causing the failure of the whole specimen.

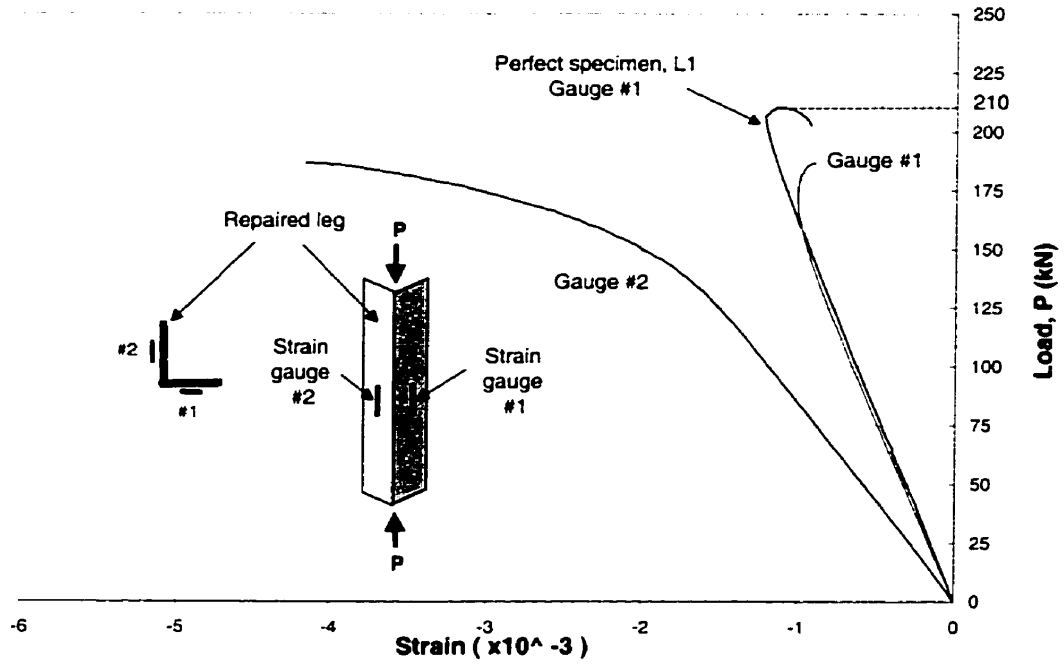

Figure 4-54: Load-strain curves for specimen L1-OR-10CS

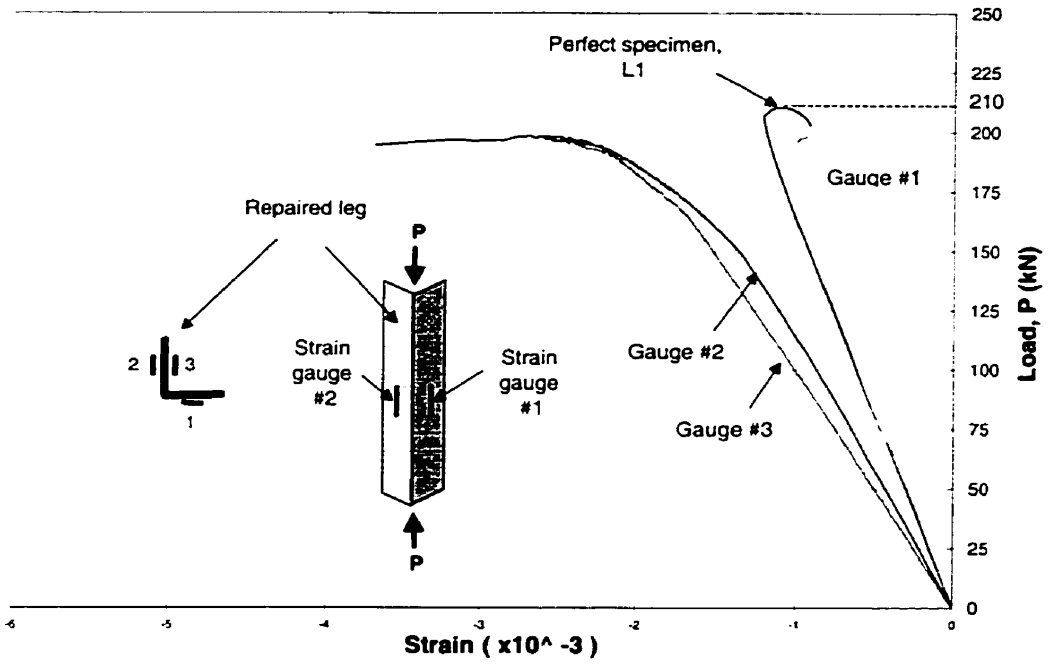

Figure 4-55: Load-strain curves for specimen L1-ER-10CS

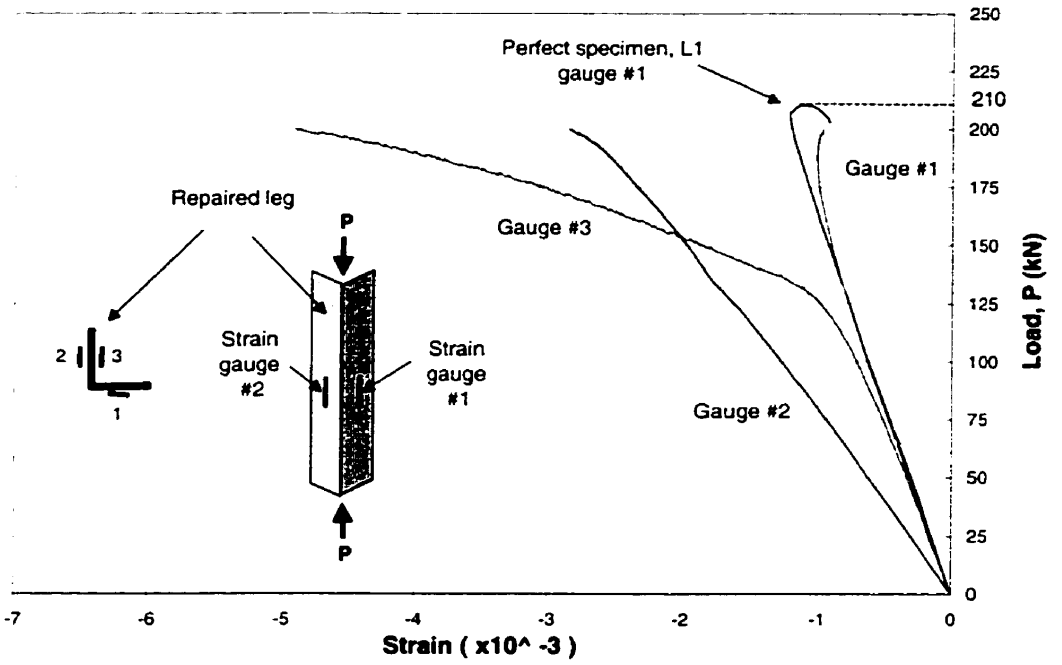

Figure 4-56: Load-strain curves for specimen L1-EOR-10CS

The strain readings from gauge #2 and #3 attached to the repaired legs of group II specimens were different than those of specimens in group I because 40-carbon steel was more brittle than 10-carbon steel. As shown in Figure 4-57, the strains from the repaired leg of specimen L2-OR-40CS were lower than the strains from the non-defective leg. However, the strain readings increased rapidly once the repaired leg failed. The difference in the strain values between the two legs is also attributed to the difference in the stress-strain relationship between the 40-carbon steel and the G40.21 steel. Gauge #2 was attached to the 40-carbon steel, whereas, gauge #1 was attached to the G40.21 steel material. The load-strain curve of L2-ER-40CS specimen is shown in Figure 4-58. The repaired leg was instrumented with two gauges. Gauge #2 was mounted on the repaired material, whereas gauge #3 was mounted on the opposite side and on the steel material. As shown in Figure 4-58 the strains on the repaired material were almost zero. In this case, most of the applied load was resisted by the remaining steel cross section. As a result, the strains in the defective leg increased at a high rate leading to failure by local buckling. The load-strain curves for specimen L2-EOR-40CS were plotted in Figure 4-59. These are quite different than those of specimen L1-EOR-10CS. As for the L2-EOR-40CS specimen, the strains in the repair material (gauge #2) were considerably higher than those of the steel (gauge #1). However, the values from gauge #3 were much lower than those from gauge #2, even though both were attached to the same repaired material.

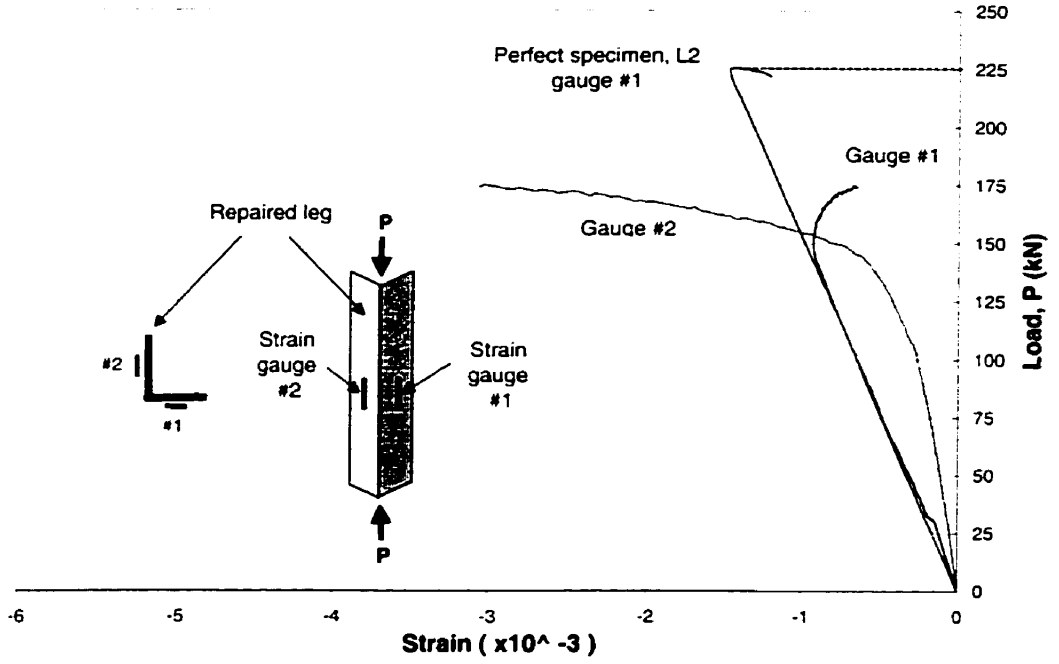

Figure 4-57: Load-strain curves for specimen L2-OR-40CS

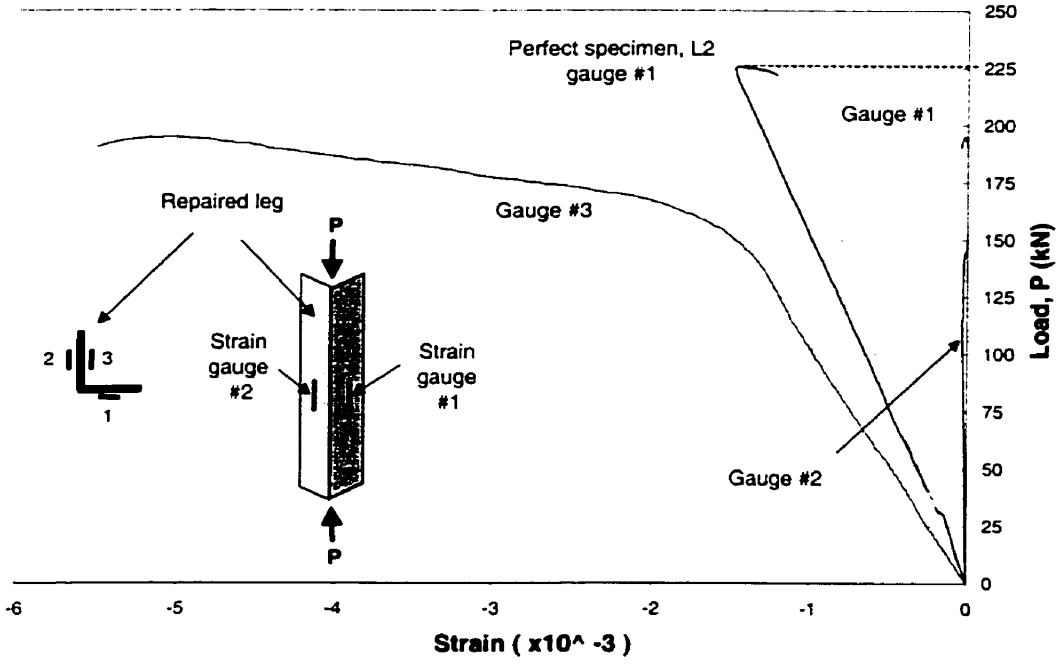

Figure 4-58: Load-strain curves for specimen L2-ER-40CS

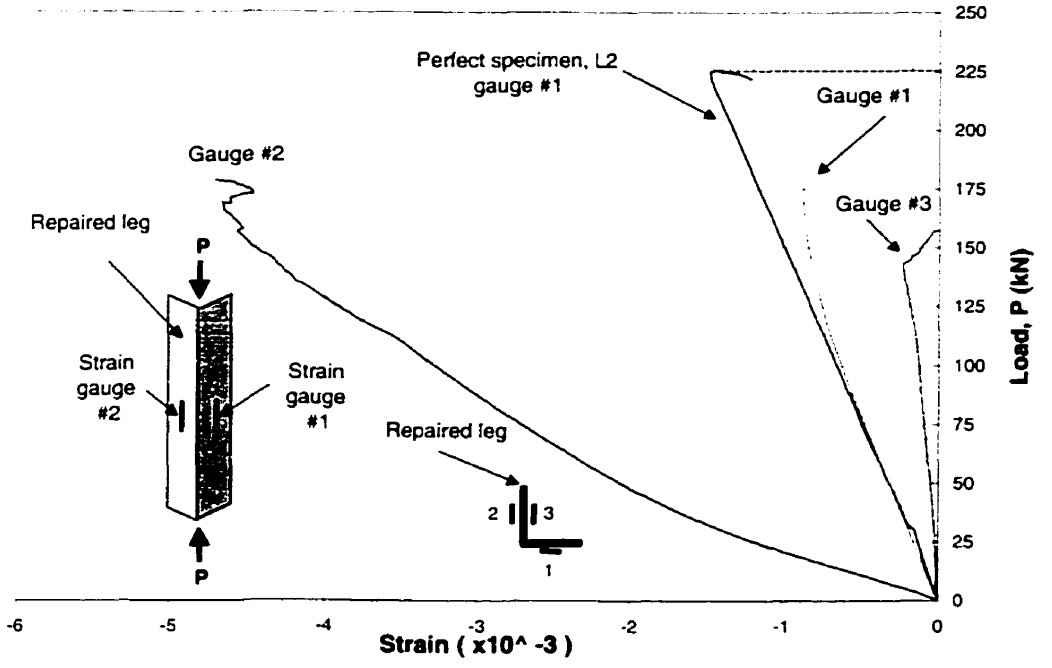

Figure 4-59: Load-strain curves for specimen L2-EOR-40CS

4.5 Phase 4: Static Tension Test on Steel Plate Specimens

Seven specimens were tested under static tension. Steel plates were machined to simulate different corrosion patterns similar as produced in the steel angle specimens. 10-carbon steel was the only repair material used in this phase because 40-carbon steel did not performed well under compression compared to 10-carbon steel.

4.5.1 Test Observations

Figure 4-60 shows the test set-up used for this series of testing with a perfect tension specimen in place. Unrepaired and repaired specimens prior to testing are shown in Figures 4-61 to 4-63. Typical tensile failure with necking deformation was observed at failure in all the unrepaired specimens. Figure 4-64 shows the failure modes of specimens P-OU and P-OR-10CS. Debonding of the repair material occurred in the P-OR-10CS specimens. No crack or damage of the spray material was observed. The P-ER-10CS specimen after testing is shown in Fig. 4-65. Failure in this specimen was first observed at the center of the repair material. A tension crack appeared suddenly across the section at mid-height of the specimen. The crack width increased with the applied load. Also, debonding occurred between the repair material and its substrate followed by failure of the steel substrate. It was difficult to observe whether cracking of the repair material or debonding occurred first. However, results from Phase 1 tests indicate that the Al coating, which had a brittle behavior, failed by debonding. Thus, it seems that the brittle 10-carbon steel coating debonded before the tension crack appeared at the center of the elliptical defect. Figure 4-66 shows specimen P-EOR-10CS after testing similarly to the case of specimen P-ER-10CS, a crack started at the circular hole and propagated to the elliptical region of the defect. Observations during these tests, showed that edges around the defective area with sharp or unrounded corners, can cause premature failure of the spray material by initiating debonding between the spray material and the substrate and introducing cracking of the section.

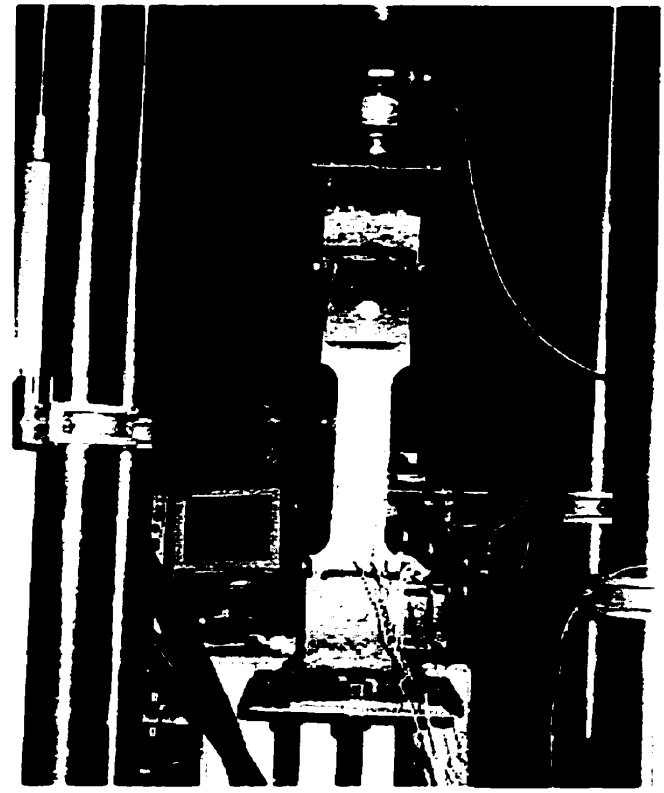

Figure 4-60:Test set-up for the tension specimens

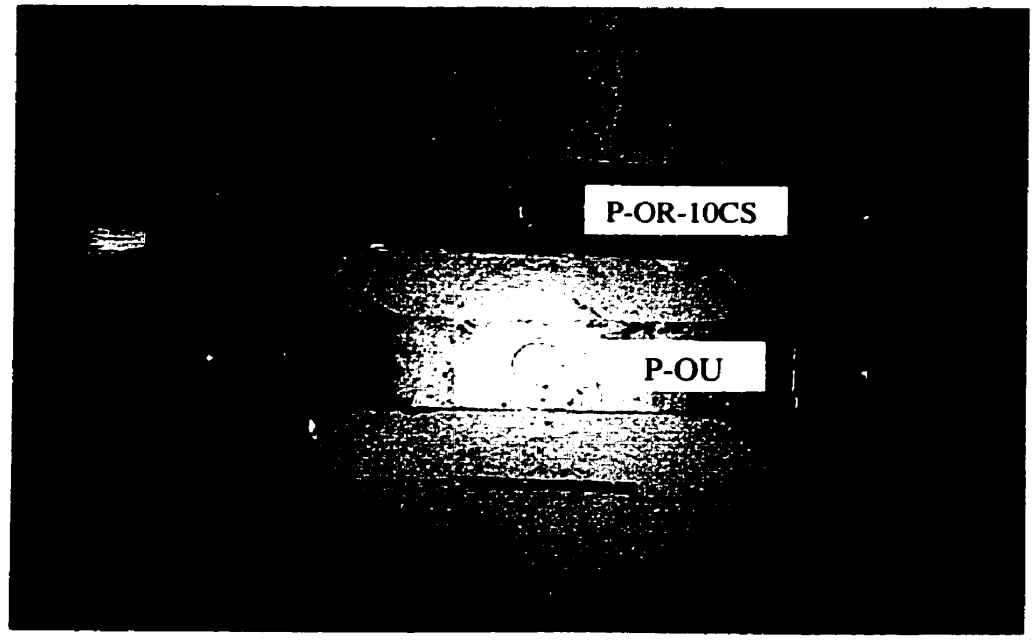

Figure 4-61: P-OU and P-OR-10CS specimens before testing

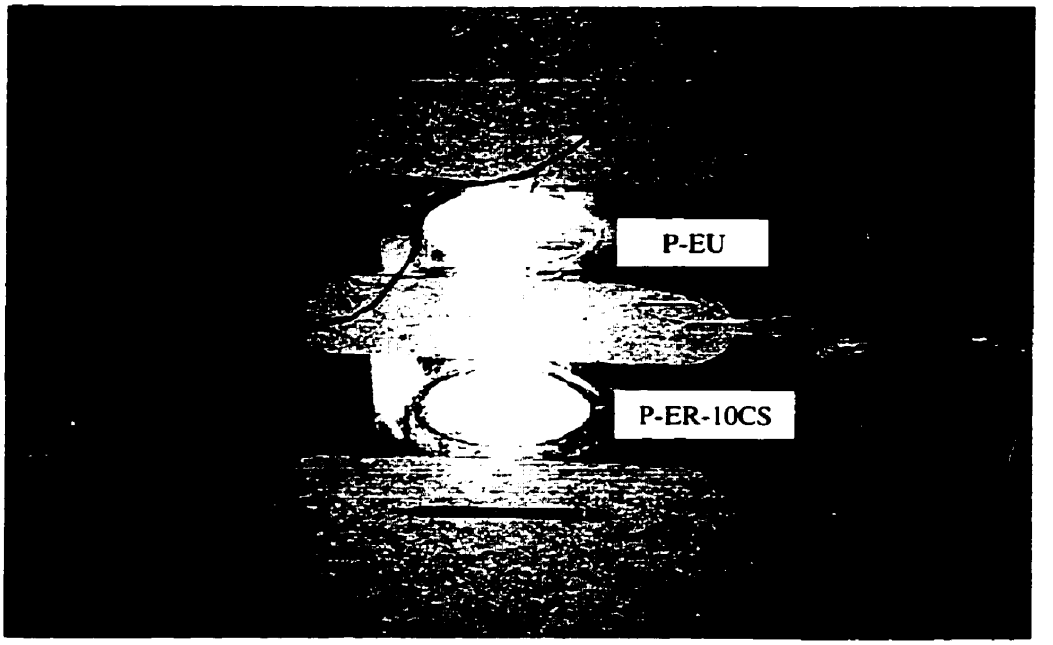

Figure 4-62: P-EU and P-ER-10CS specimens before testing

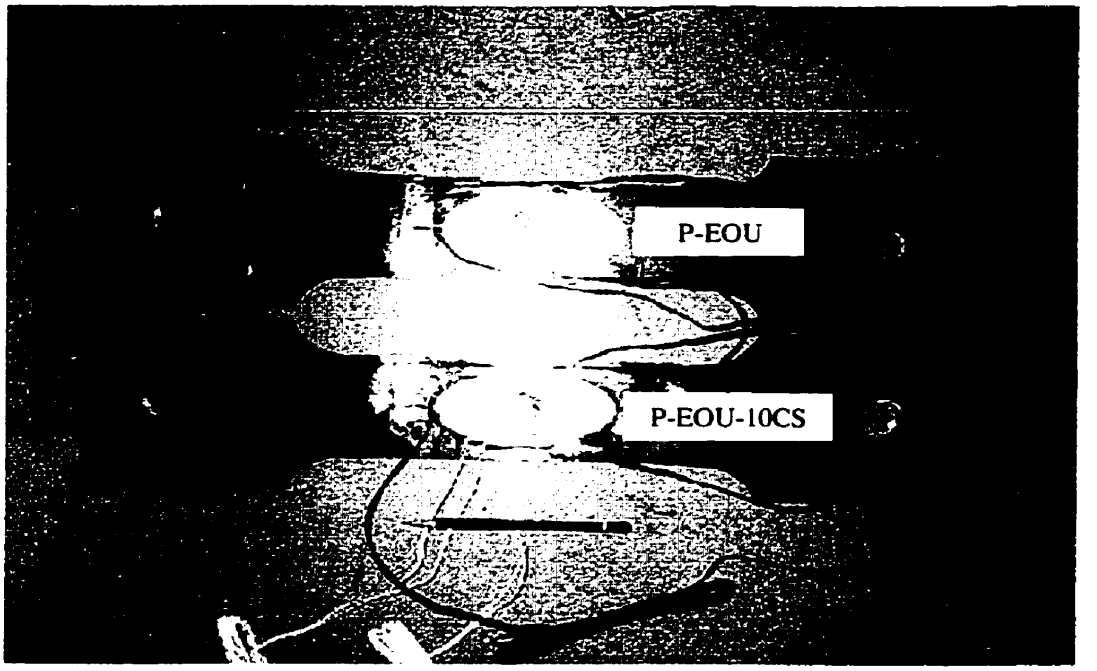

Figure 4-63: P-EOU and P-EOR-10CS specimens before testing

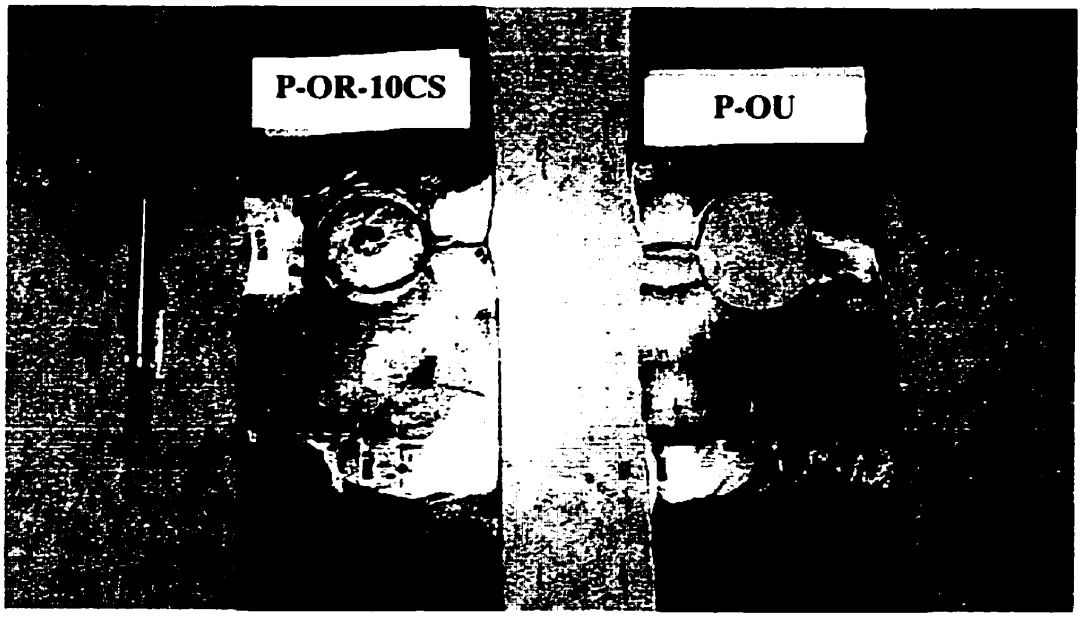

Figure 4-64: Failure modes of P-OU and P-OR-10CS specimens

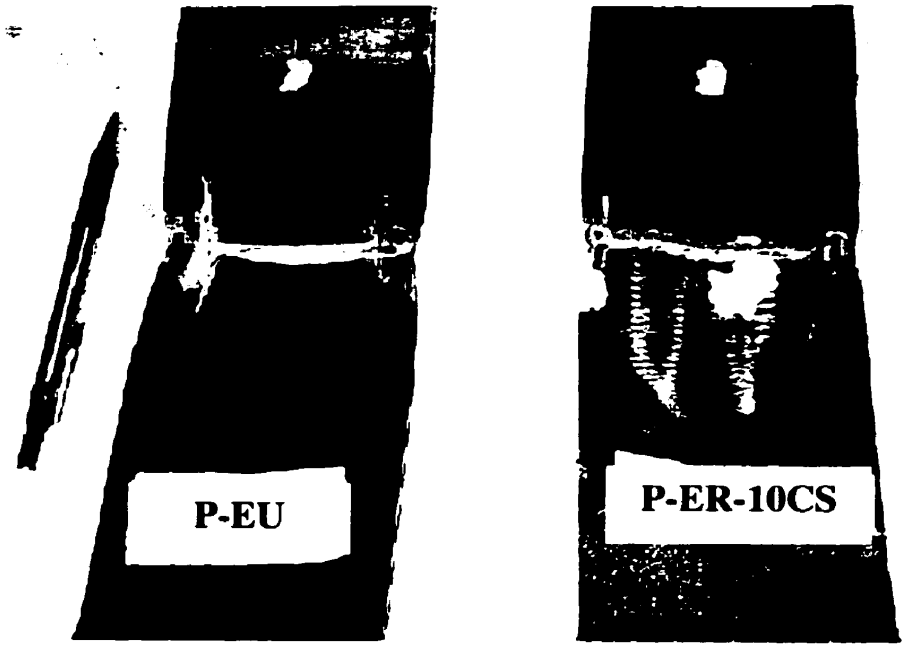

Figure 4-65: Failure modes of P-EU and P-ER-10CS specimens

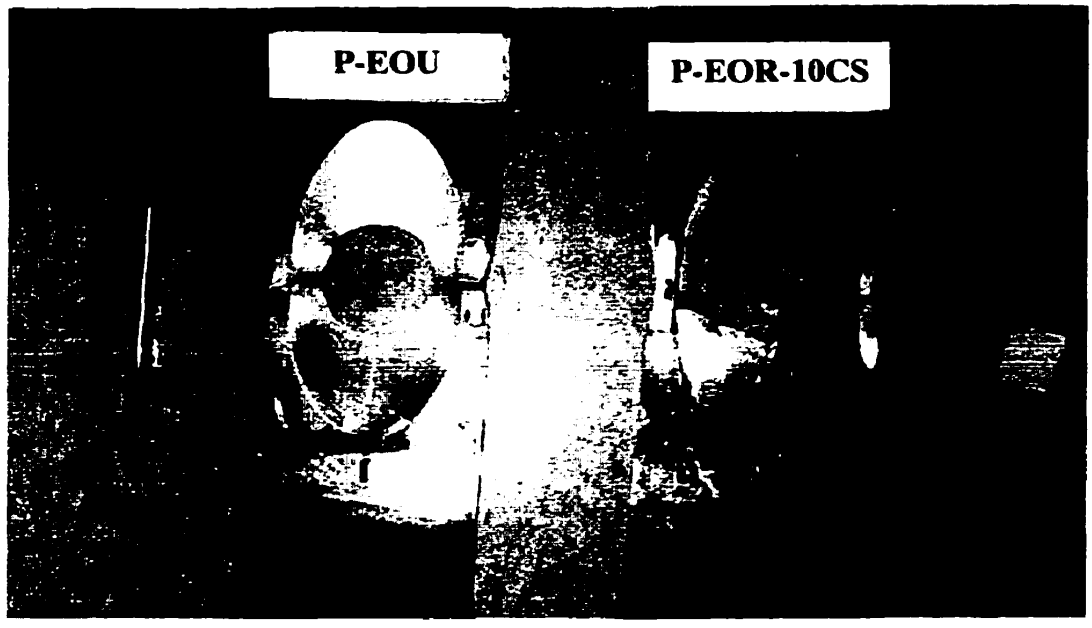

Figure 4-66: Failure modes of P-EOU and P-EOR-10CS specimens

4.5.2 Test Results and Analysis

The results from phase 4 are summarized in Figure 4-67. In this figure, the ratio of the ultimate load of both the unrepaired and the specimens repaired with 10-carbon steel material to the ultimate load of the perfect specimen is shown for comparison. In general, the spray material had almost no effect on the strength of the repaired specimens. There were no strength improvements in either the P-OR-10CS or P-EOR-10CS specimens. There was a small improvement in the strength of the P-ER-10CS specimen

from 88 kN to 102 kN, an increase of 16%. The strength of both the repaired and unrepaired specimens are 67% and 58% strength of the perfect specimen, respectively.

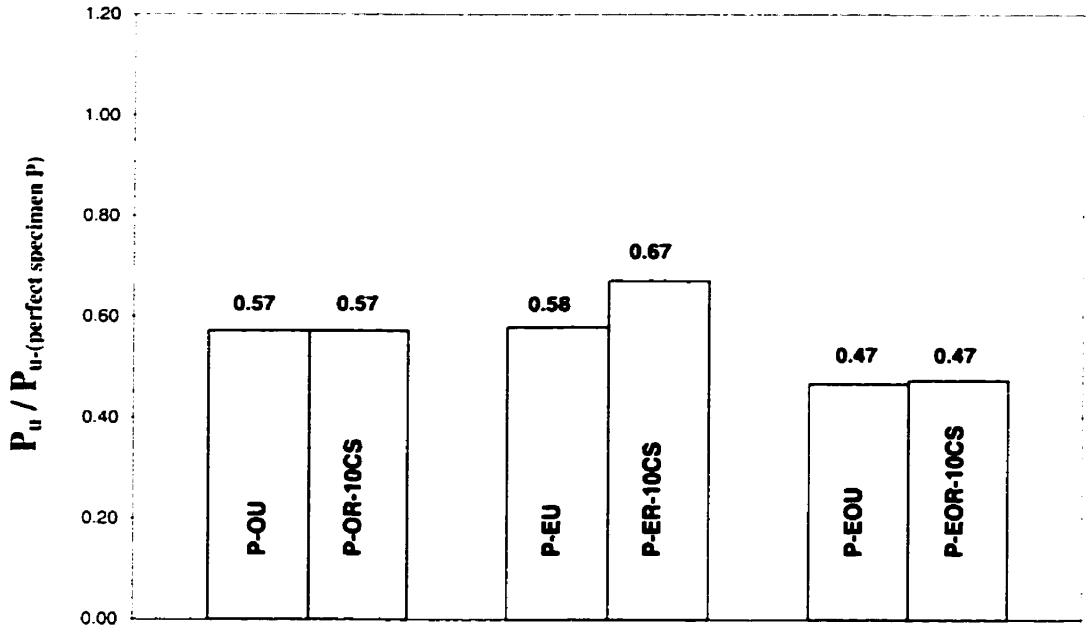

Figure 4-67: Strength comparison for the repaired and unrepaired specimens

The strain distributions in the repaired specimens, shown in Figures 4-68 to 4-70, were almost the same as those of the unrepaired specimens recorded at the same location. Strain gauge #1 was used to measure the strain in the steel near the edge of the defected area. Strain gauge #2 was used to measure the strain at the center of the spray material. In specimens P-ER-10CS and P-EOR-10CS, strain gauge #3 was used to measure the

strain of steel immediately behind the repair patch. In specimen P-EOR-10CS, strain gauge #3 was attached on the spray material behind the hole of the elliptical defect.

The load-strain curves shown in Figure 4-68 show that strain gauge #2 attached to the repair material of specimen P-OR-10CS did not register any strain. This is an indication that the spray material was not carrying any load. A similar behavior was observed in specimen P-EOR-10CS, shown in Figure 4-70. In this case, the strain gauge #3 attached to the spray material debonded from the material at a very low load. The strain readings from strain gauge #2 indicate that the spray material, with larger contact area in the elliptical region, had some bonding capacity but failed at 20 kN. The load-strain curve for specimen P-ER-10CS, shown in Figure 4-69 indicates that the spray material failed suddenly at 104 kN. The spray material could not resist additional load after cracking. The load suddenly dropped from 104kN to 80kN, the same level as the unrepaired specimen P-EU. During the drop of the load the strains recorded by strain gauge #2 attached at the center of the repair material were the same as those recorded by strain gauge #3 attached to the steel substrate behind the repair material. In this case the repair material was still bonded to the substrate.

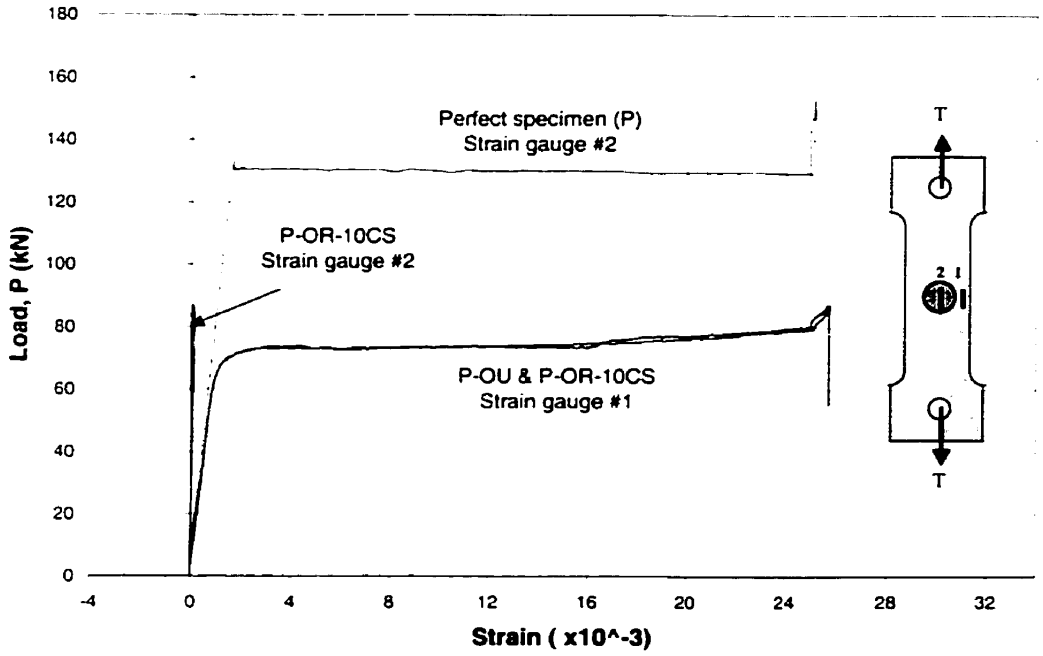

Figure 4-68: Strains in specimens P-OU and P-OR-10CS

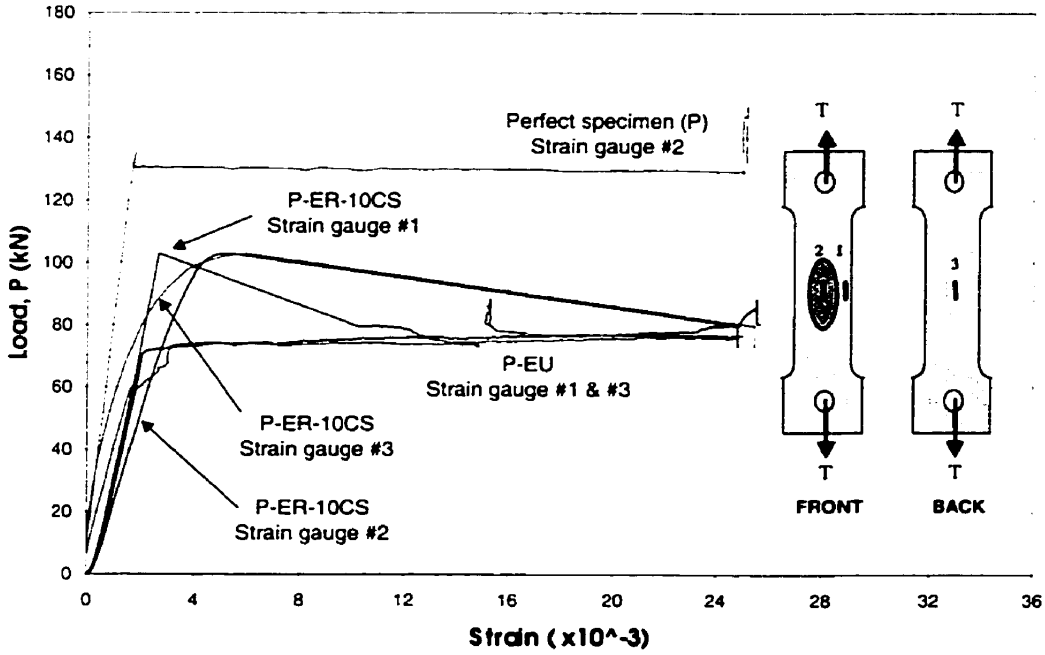

Figure 4-69: Strains in specimens P-EU and P-ER-10CS

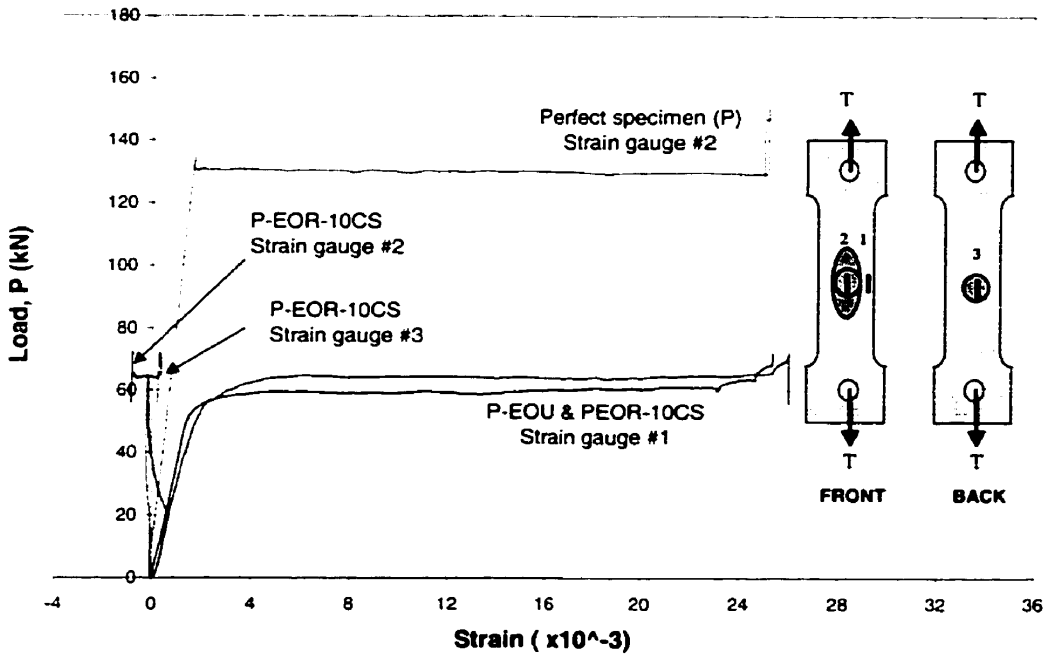

Figure 4-70: Strains in specimens P-EOU and P-EOR-10CS

CHAPTER 5

FINITE ELEMENT MODELING

5.1 General

Thermal spray metallizing was used to repair steel structural elements in this research program. This technique proved to be effective in improving the strength of members in compression. However, the simulated corrosion patterns used in this research program were limited to certain configurations. Corrosion patterns in natural corrosive environments are in random configurations. It is, thus, impossible to simulate all possible corrosion patterns in an experimental program. In order to resolve this limitation, finite element modeling was used to model possible corrosion patterns on a steel member. The commercially available software package ANSYS was used to develop the finite element modeling which is presented in this chapter.

The experimental results from Phase 4 showed that the repair material subjected to tensile stress did not improve the strength of the substrate material. Therefore, no finite element modeling of the tension specimens was performed. In compression tests, the repair material of 10-carbon steel showed a better performance than the 40-carbon steel. Thus, the steel angle compression specimens repaired with 10-carbon steel were

modeled using the ANSYS program in this chapter. The ultimate strength and load-strain behaviors of the specimens modeled by the ANSYS program were compared to the experimental results to verify the accuracy of the modeling.

5.2 Finite Element Modeling

A non-linear structural analysis was performed with the finite element modeling by the ANSYS software. This type of analysis has the capability to account for both the geometric and material non-linearities of a model [35]. The non-linear stress-strain relationship of a member material is the most common source of non-linear structural behavior. The ANSYS program provides the equation solver that operates on a set of simultaneous linear equations to predict the response of an engineering system. The applied load is divided into several increments. At the completion of each incremental solution, the program adjusts the stiffness matrix to reflect the non-linear changes in the structural stiffness before proceeding to the next load increment. The Newton-Raphson method, which drives the solution to equilibrium convergence within a specified tolerance limit at the end of each load increment was used to minimize the accumulated error at each load increment.

The three-dimensional models were developed by the program to model the compression steel angle specimens as tested in the experimental program. Two types of structural 3-D solid elements were used in the modeling and the angle member was divided into three sections. The element SOLID95 with 20 nodal points was used in the mid section to model the simulated defect and its complicated deformation accurately.

The other element was the SOLID73 with only 8 nodal points which used to model the end sections. This element was chosen because the end cross sections were constant and no complicated deformations were produced. Additionally, this element requires less computation time compared to the 20-node element.

The models were loaded through the centroid of the angle section. As shown in Figures A-1, Appendix A, the bearing blocks were placed at the ends of the angle section for purposes of applying the load and maintaining the required degrees-of-freedom at the centroid. This design was similar to that used in the experimental set-up. At one end of the section, where a pin support was assumed, no displacement was allowed in all directions except for the rotations about the pin support. At the other end, the load was applied through centroid and the degrees-of-freedom were restricted in all directions except for the displacement in longitudinal axis and the rotations about the pin support.

5.3 Analytical Strength for Steel Angle

The buckling strength of a compression angle section can also be calculated, rationally, using Euler's Equation 5-1 in the elastic range and the Column Research Council (CRC) buckling Equation 5-2 in the inelastic range of a member behavior [36]. Figure 5-1 shows the principal axes of an angle section that were used in calculating the sectional properties. Euler's equation was used to determine the elastic buckling strength when the applied stresses was less than half of the yield stress. For applied stresses that exceeded half of its yield stress, inelastic behavior was assumed. In this range, the CRC equation was used to calculate the ultimate strength of the steel angle. Figure 5-2 shows

both the theoretical results by the CRC equation and the analytical results from the ANSYS modeling. In general, the results in the inelastic range obtained from ANSYS modeling were lower than the results obtained from the rational analysis. However, the ANSYS results were very close to the rational results in the elastic range. In the inelastic range, the results obtained from ANSYS were 8.5 percent to 17 percent lower than the CRC results. Therefore, this ANSYS modeling is suitable for analyzing angle sections with an effective length greater than 750 mm.

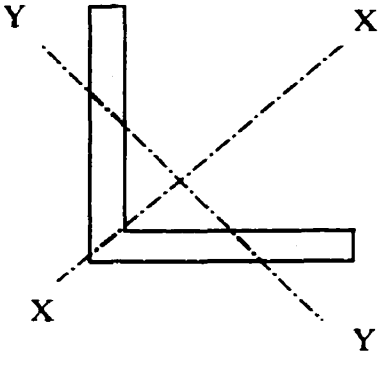

Figure 5-1: Principal axes of angle section

For $F_{cr(el)} \leq \frac{F_y}{2}$, $\quad F_{cr(el)} = \frac{P}{A} = \frac{\pi^2 E}{(KL/r)_y^2}$ ..... Eq. 5-1

For $F_{cr(el)} \leq \frac{F_y}{2}$, $\quad F_{cr(inel)} = \frac{P}{A} = F_y\left[1 - \frac{F_y}{4\pi^2 E}\left(\frac{KL}{r}\right)_y^2\right]$ ..... Eq. 5-2

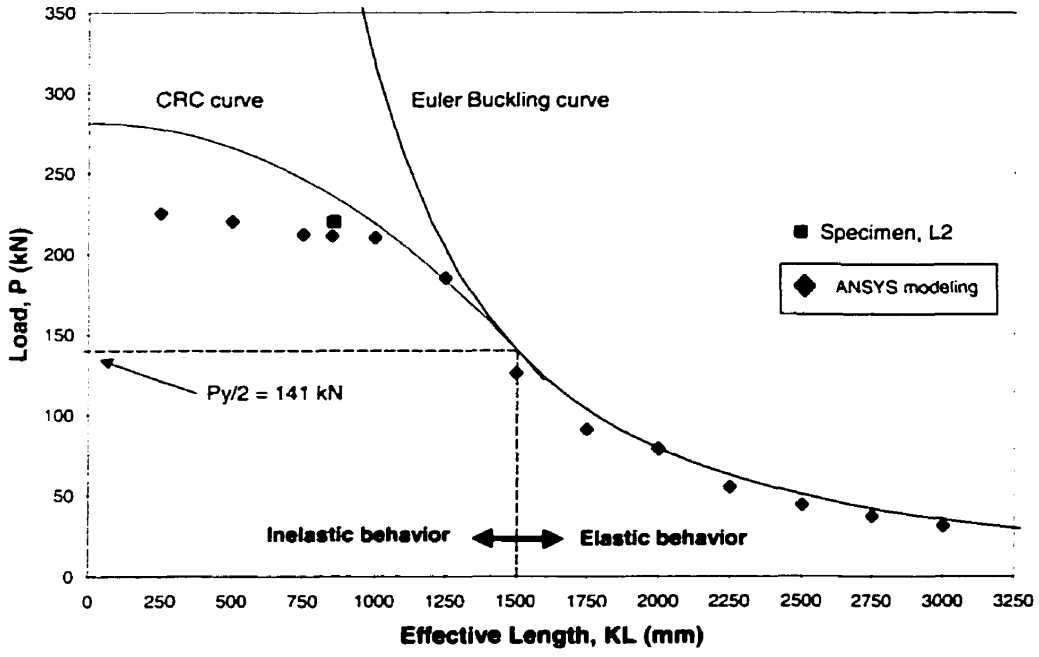

Figure 5-2: Theoretical critical load of steel angle sections

5.4 Material Properties

The material properties obtained from the testing of tension coupons were used in the finite element model. Three standard tension specimens were extracted from the compression angle sections and tested to determine their mechanical properties. The stress-strain curves are shown in Figure 5-3. They were used to obtain the yield strength of the specimens using the 0.2 percent offset method. Figure 5-4 shows the longitudinal and transverse strains used to obtain the Poisson's ratio of the steel material. The mechanical properties of the spray material 10-carbon steel investigated in section 4.3 were used in the modeling. The material properties of the steel and spray material used in the finite element models are shown in Table 5-1.

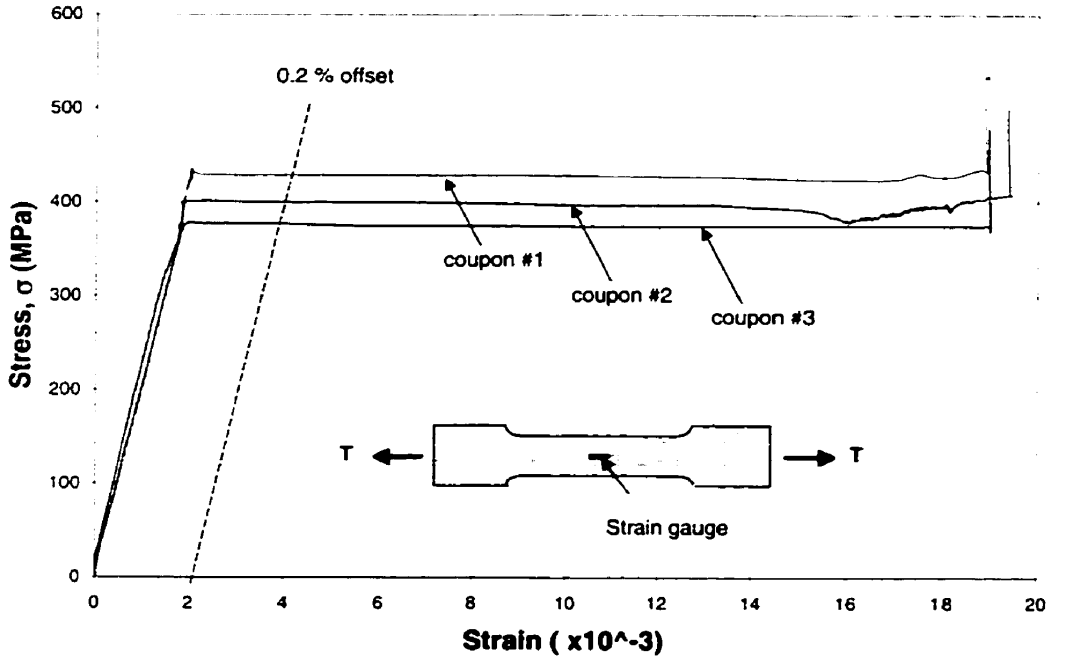

Figure 5-3: Stress-strain curves for tension coupons

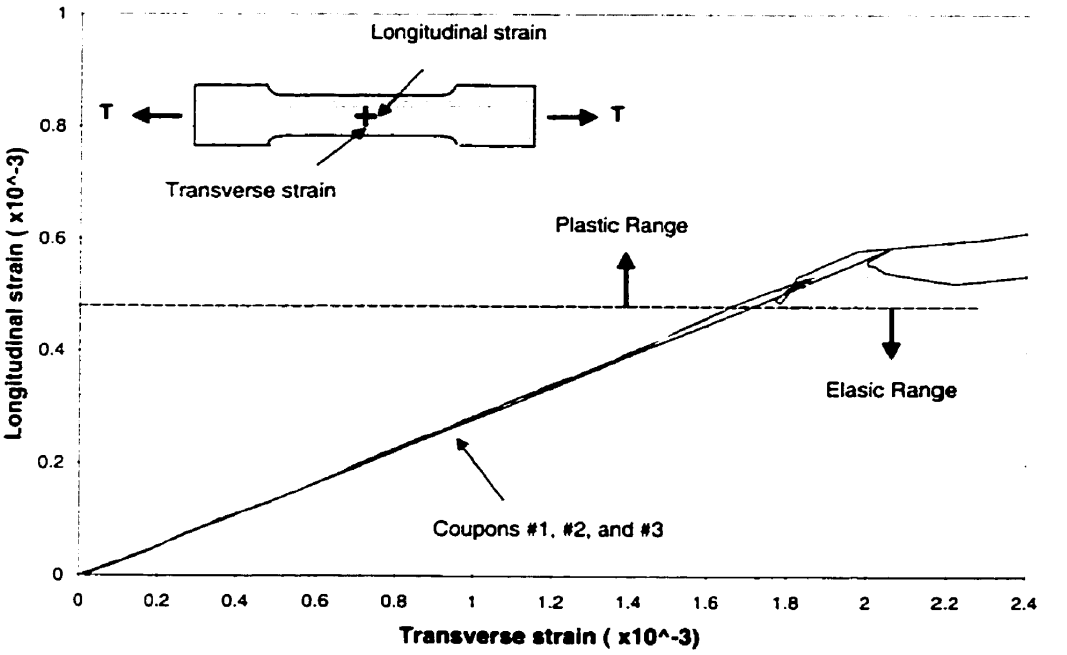

Figure 5-4: Poisson's ratio at the elastic range

Table 5-1: Mechanical properties of materials used in the finite element modeling

Material	Modulus of Elasticity, (E)	Poisson's Ratio, (v)	Yield Strength, (F_y)
Mild steel	211,000 MPa	0.285	400 MPa
10-carbon steel	80,000 MPa	0.180	None

The steel angle sections modeled by ANSYS before and after failure are shown in Figures A-1 to A-12 in Appendix A. The buckling modes of the modeled specimens are similar to those of the experimental program. Figure 5-2 gives the ratio of the ultimate strength of the angles obtained experimentally to the ultimate strength obtained analytically. The ratio ranged from 0.89 to 1.06. Thus, the finite element modeling gives good results and is suitable for use in estimating the ultimate strength of a repaired angle specimens.

In additional to strength results, the analytical model was used to obtain load-strain distributions. These were compared to the experimental results to verify the reliability of the finite element modeling. The load-strain curves for both the experimental and the analytical results for all specimens are plotted in Figures 5-6 to 5-11. The results indicate that the finite element program gives good results. For the

L1-EOR-10CS specimen, the analytical strains shown in Figure 5-11 deviate a little from the experimental results only for the repaired leg, otherwise the results are satisfactory.

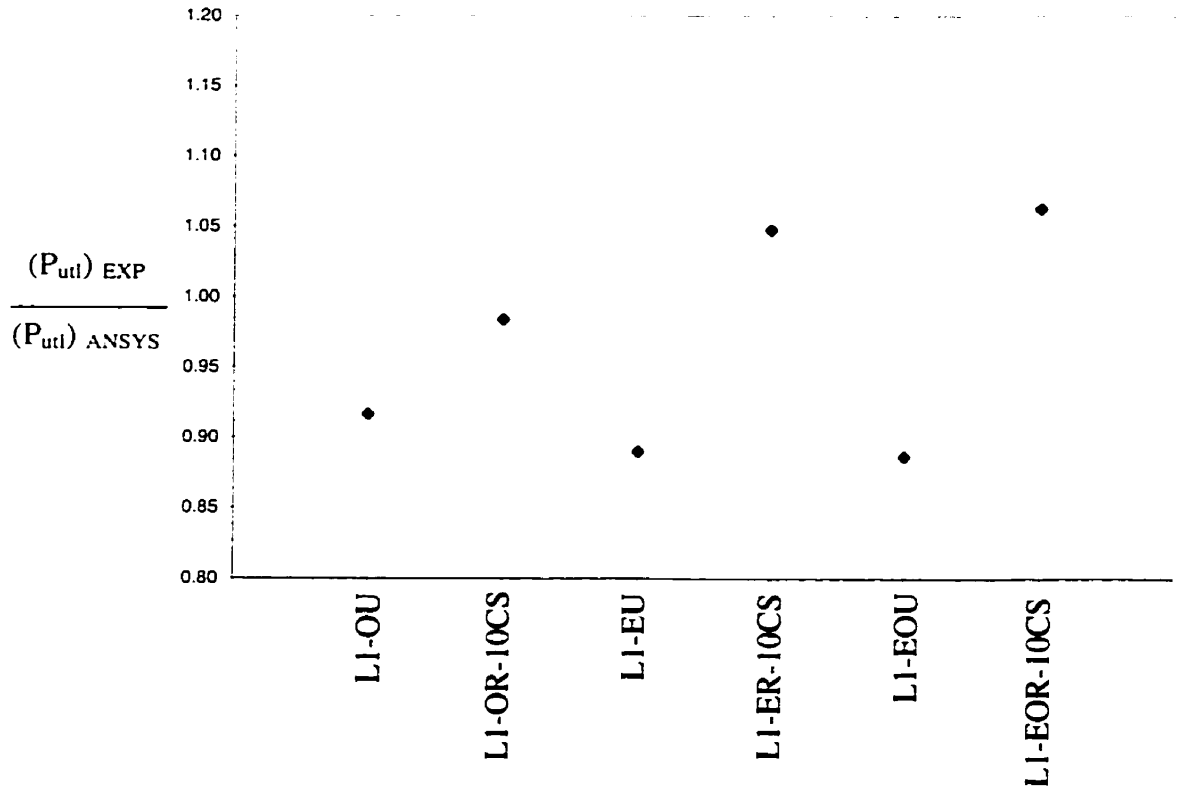

Figure 5-5: Ratio of Experimental to Analytical ultimate strength results

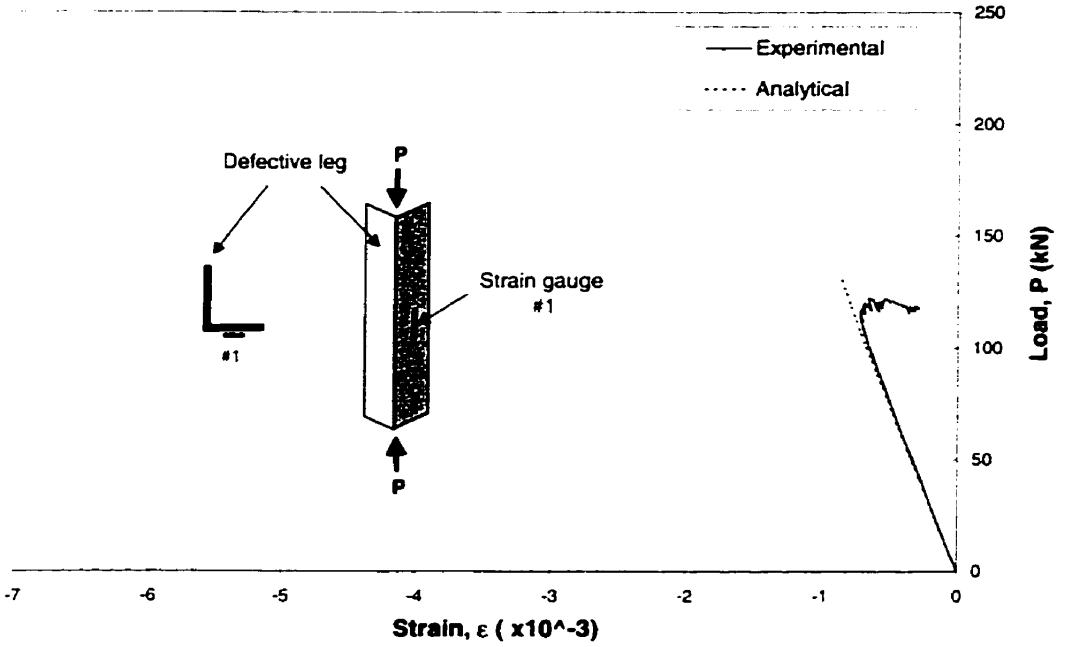

Figure 5-6: Experimental and analytical load-strain curves for L1-OU specimen

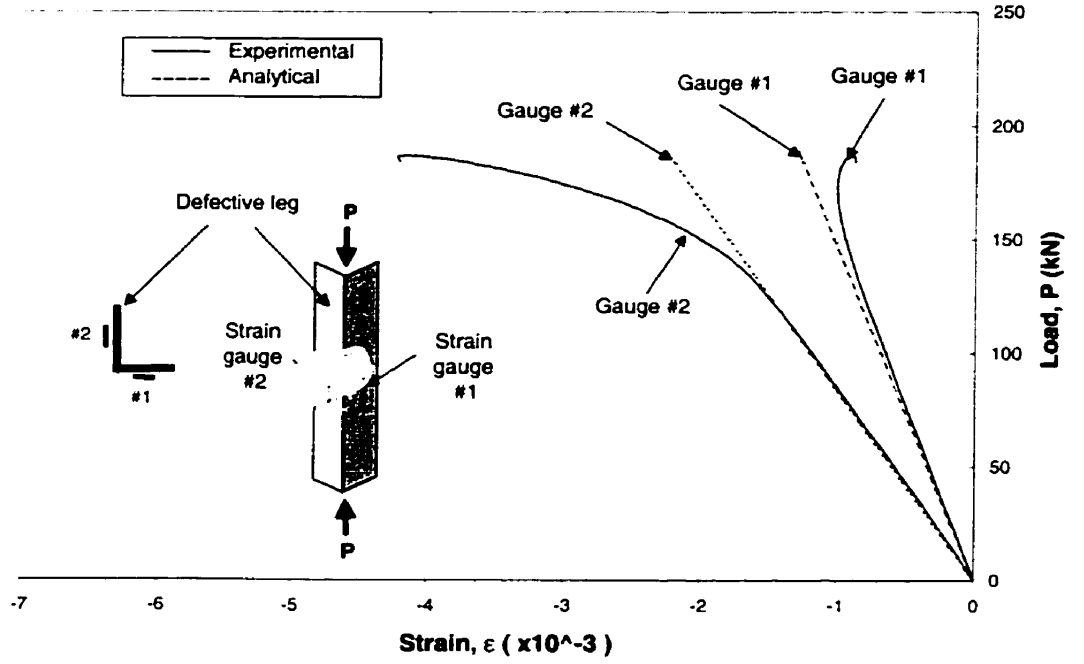

Figure 5-7: Experimental and analytical load-strain curves for L1-OR-10CS specimen

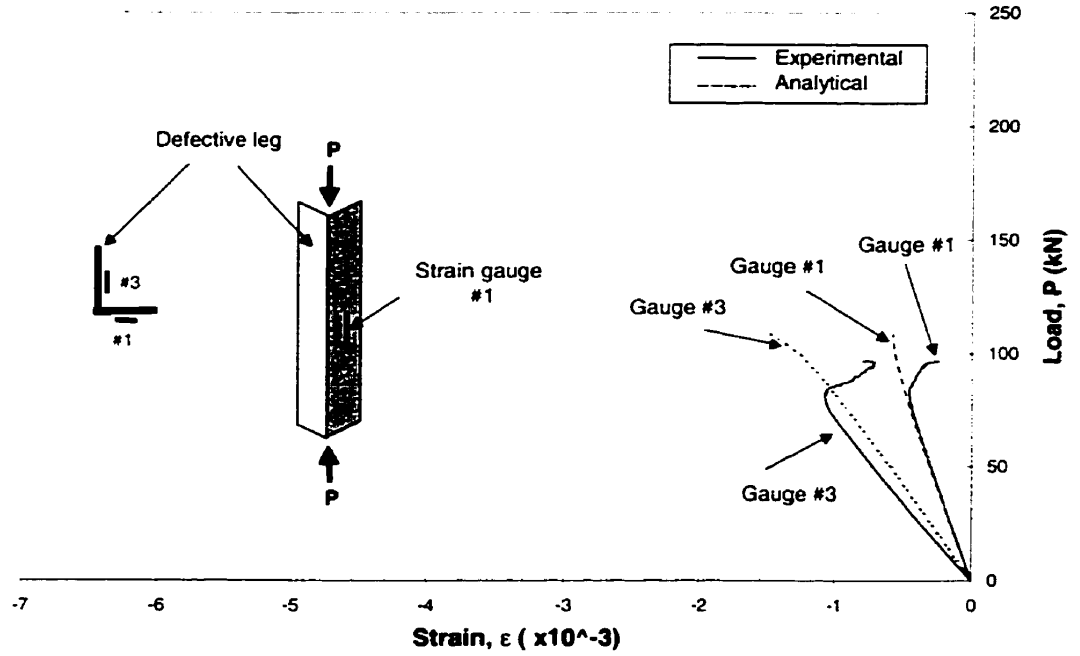

Figure 5-8: Experimental and analytical load-strain curves for L1-EU specimen

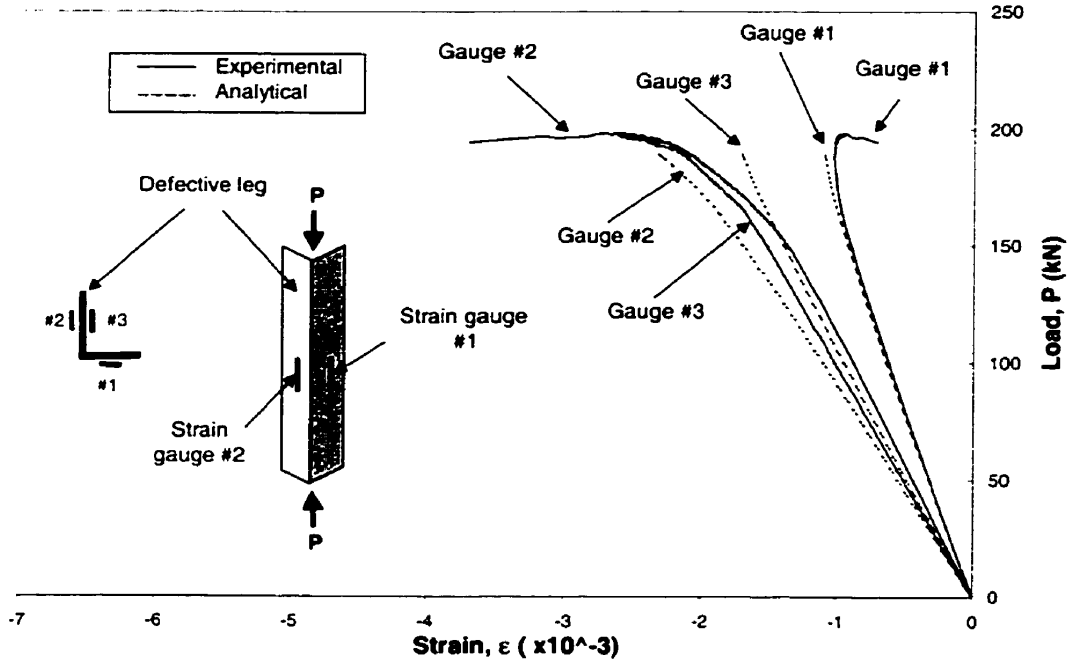

Figure 5-9: Experimental and analytical load-strain curves for L1-ER-10CS specimen

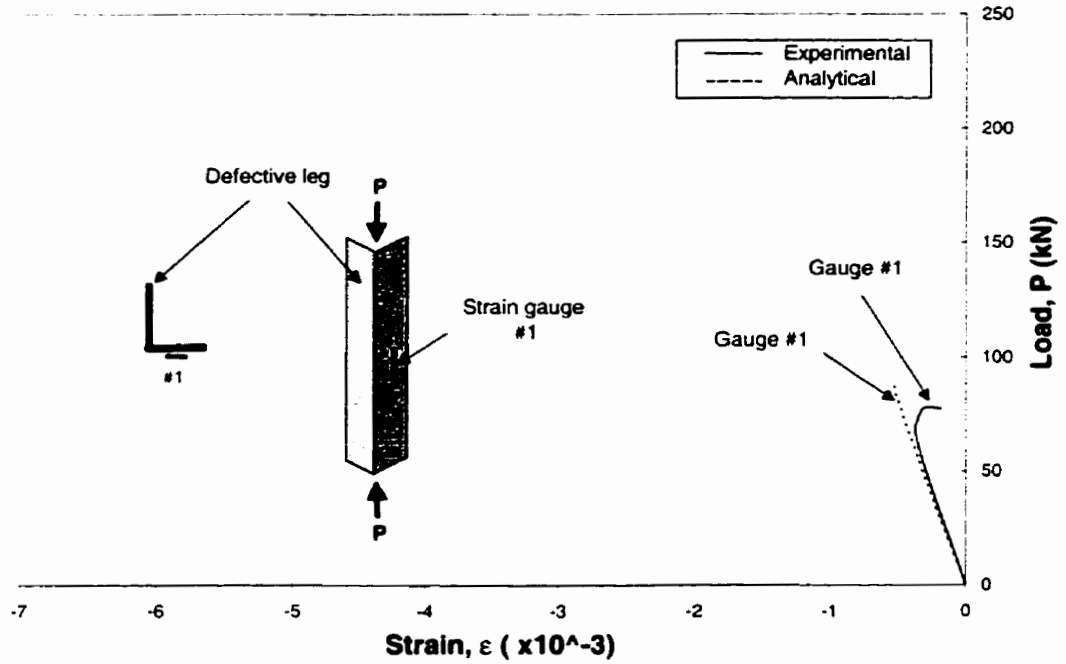

Figure 5-10: Experimental and analytical load-strain curves for L1-EOU specimen

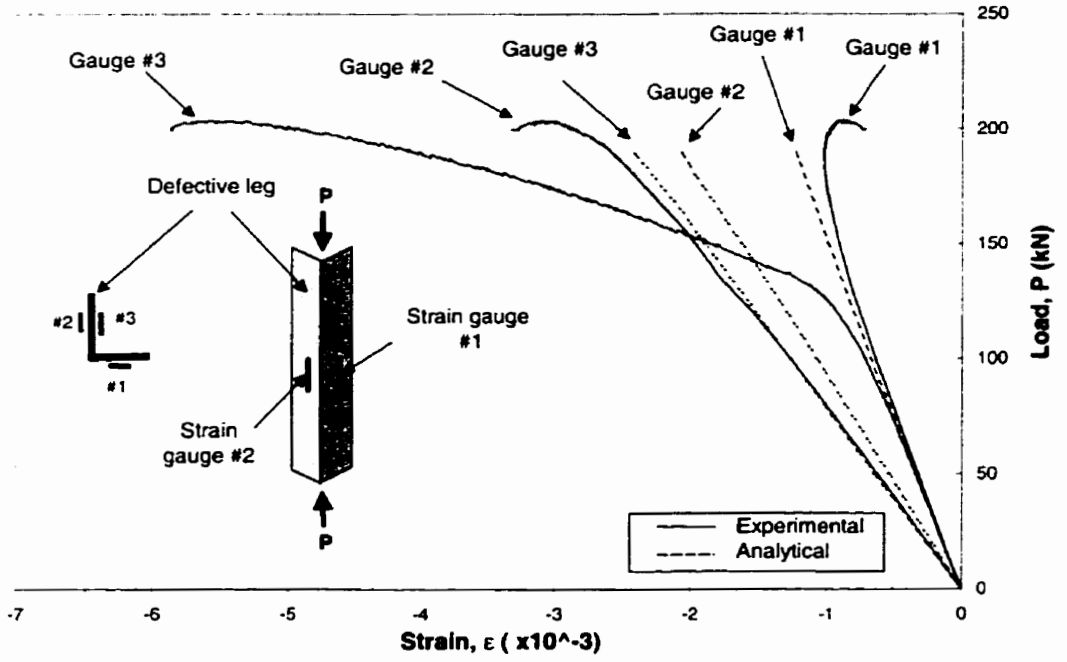

Figure 5-11: Experimental and analytical load-strain curves for L1-EOR-10CS specimen

CHAPTER 6

SUMMARY AND CONCLUSIONS

6.1 Summary

The use of the thermal spraying technique for strengthening corroded steel structures was the focus in this research project. The performance of thermal spray coatings was investigated through experimental testing involving standard coupons, steel angle and steel plate specimens. Based on the experimental results, a finite element model was developed using the ANSYS program to predict the buckling strength of defective angle sections that were either unrepaired or repaired with spray material.

Four phases of testing were conducted in this research program:

Phase 1 - A total of 15 standard coupons with and without spray coating were tested under static tension. Three identical specimens of each type were fabricated using Zinc, Aluminum, and $Zinc^{85}Aluminum^{15}$ alloy as the spray coating applied to a steel substrate. The objective of the testing in this phase was to investigate the tensile properties of the spray materials.

Phase 2 - Three groups of specimens consisting three specimens each were tested to investigate the compressive properties of the spray materials. In the first group of specimens, cylindrical steel specimens were tested. In the second group, cylindrical specimens that were machined to reduce their cross-sectional area were tested. Both of these groups of specimens were used as the control specimens and represented the original and the defective specimens. The third group of specimens involved specimens similar to that of the second group, but coated with thermal spray material. Based on the findings in Phase 1 testing, the spray materials of Zinc and Aluminum were not used in Phase 2. $Zinc^{85}Aluminum^{15}$, 10-carbon steel, and 40-carbon steel were the spray coating materials used in this phase.

Phase 3 - Fourteen steel angle sections, with and without spray coating, were tested under static compression in this phase. Three types of defects simulating corrosion patterns were imposed on the angles: a circular hole, an elliptical defect with a depth equal to 83% of the thickness of the angles, and combination of elliptical and a circular hole. Two identical specimens for each simulated defect were fabricated. One of those was unrepaired and the other was repaired with spray materials. The spray material of $Zinc^{85}Aluminum^{15}$ was eliminated because of its low compressive strength. However, 10-carbon steel and the 40-carbon steel were used as the repair materials in these angle sections. The objective of this testing was to

investigate the strength improvement in repaired specimens under compression.

Phase 4 - Seven steel plate specimens were tested under static tension in this phase. The specimens were fabricated with a reduced cross section to control the failure location. Similar substrate thickness and defect configurations as in Phase 3 specimens were used in the specimens of Phase 4. Based on the results of the investigation in Phases 1, 2, and 3, 10-carbon steel was used to repair the tension specimens in Phase 4. The objective of this testing was to investigate the improvement in the tensile strength for steel plate specimens repaired with thermal spray coatings.

6.2 Conclusions

This study has shown that the thermal spray technique using 10-carbon steel is an effective repair technique for strengthening compression sensitive members subjected to serious corrosion deterioration. This technique, however, did not improve the tensile resistance of steel members. More specifically, this research program showed that:

1. The failure mode of spray materials under tension depends on their ductility. Ductile spray materials (Zinc, Aluminum, and $Zinc^{85}Aluminum^{15}$) have low tensile strength and crack under tension. On the other hand, brittle spray materials exhibit debonding from the substrate before cracking.

2. The brittle spray coatings, 10-carbon steel and 40-carbon steel, in the compression coupons failed suddenly by first debonding and then by crushing. The strength of the repaired specimens coated with the 10-carbon steel and 40-carbon steel improved significantly. However, 10-carbon steel exhibited a better performance compared to 40-carbon steel in repairing steel angles.

3. The ultimate strength of compression steel angle specimens repaired with 10-carbon steel, improved by at least 87%. The strength of steel angle specimen repaired with 40-carbon steel improved by at least 78%.

4. Tension plate specimens repaired with 10-carbon steel showed no strength improvement.

5. In general, the spray materials (Zinc, Aluminum, Zinc-Aluminum, 10-carbon steel, and 40-carbon steel) have low tensile strength. Thus, these spray materials are not suitable for repairing members under tensile loads.

6. The finite element model that was developed predicted a lower strength (2% to 6%) for the repaired specimens, but a higher strength (9% to 13%) for the unrepaired specimens. This model would be ideal for predicting the strength of repaired members with defects that have been cleaned and machined to produce rounded corners prior to metallizing.

6.3 Recommendations for Future Research

In order to achieve a more comprehensive understanding on the behavior of steel structures repaired through the thermal spray technique, further research is recommended in the following areas:

1. Performance of spray coating as repair material under cyclic and dynamic loading;

2. Effect of temperature changes on the performance of spray material in service loading;

3. Material characterization of spray coatings for shear strengthening of steel members;

4. Development of better spray materials with stronger bond strength and higher moduli of elasticity;

5. Effect of preheating process on spray substrate to reduce the residual stresses of spray material

6. Effect of bond coat on increasing the bonding of spray material and the spray substrate

APPENDIX A

FINITE ELEMENT MODELING
OF
STEEL ANGLES

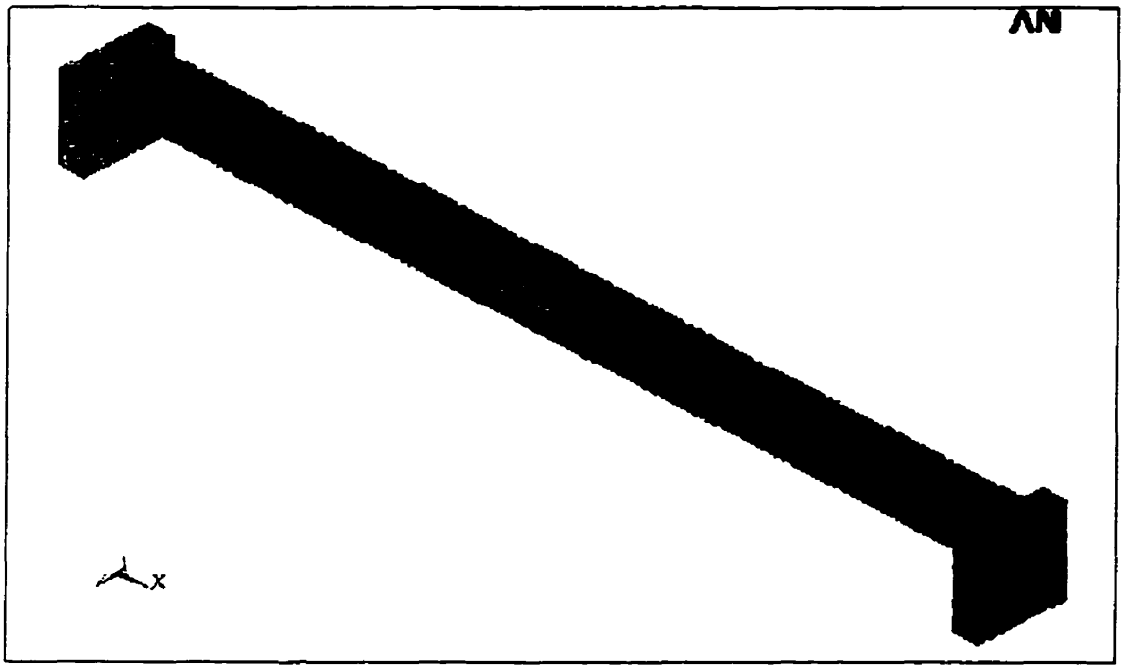

Figure A-1: The L1-OU model before failure

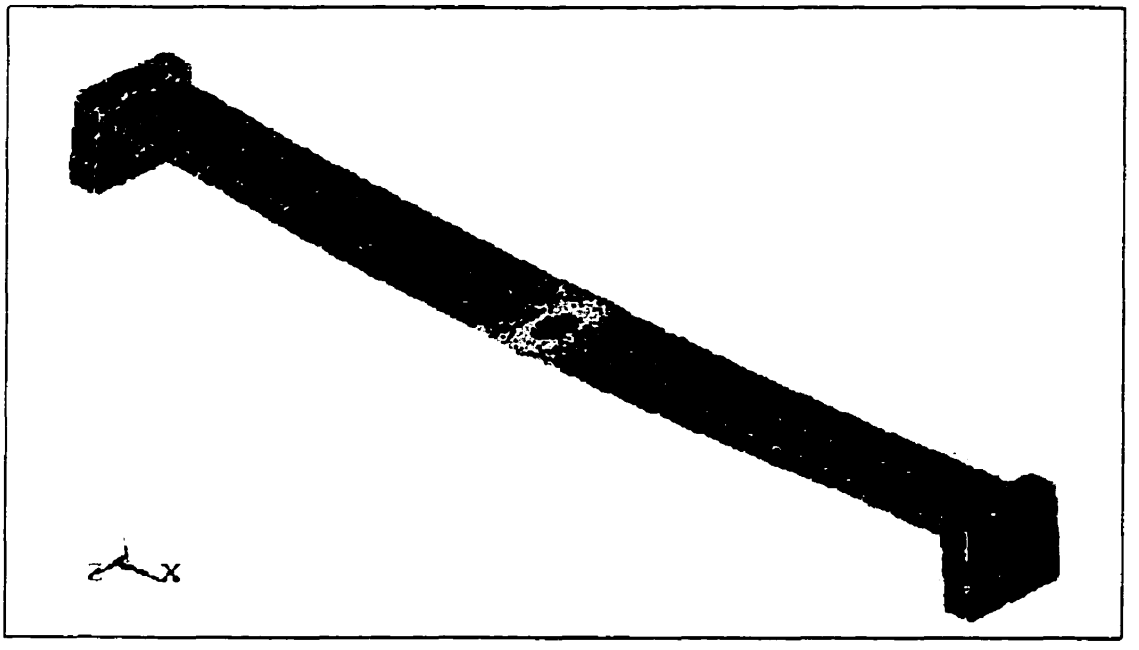

Figure A-2: The L1-OU model after failure

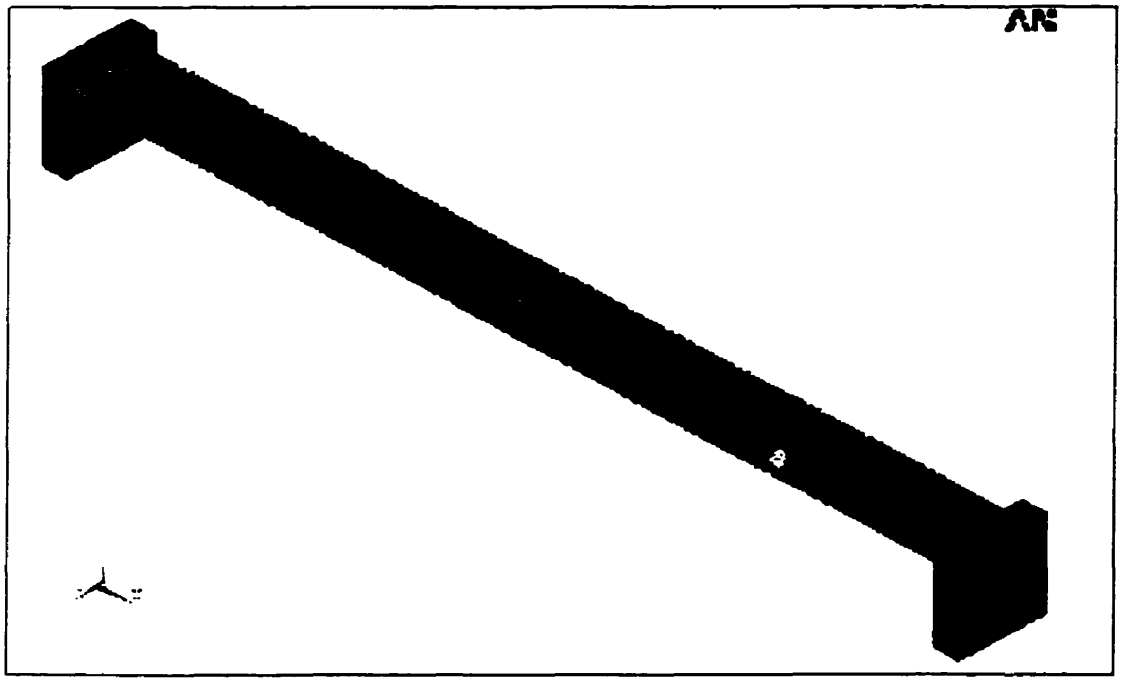

Figure A-3: The L1-OR-10CS model before failure

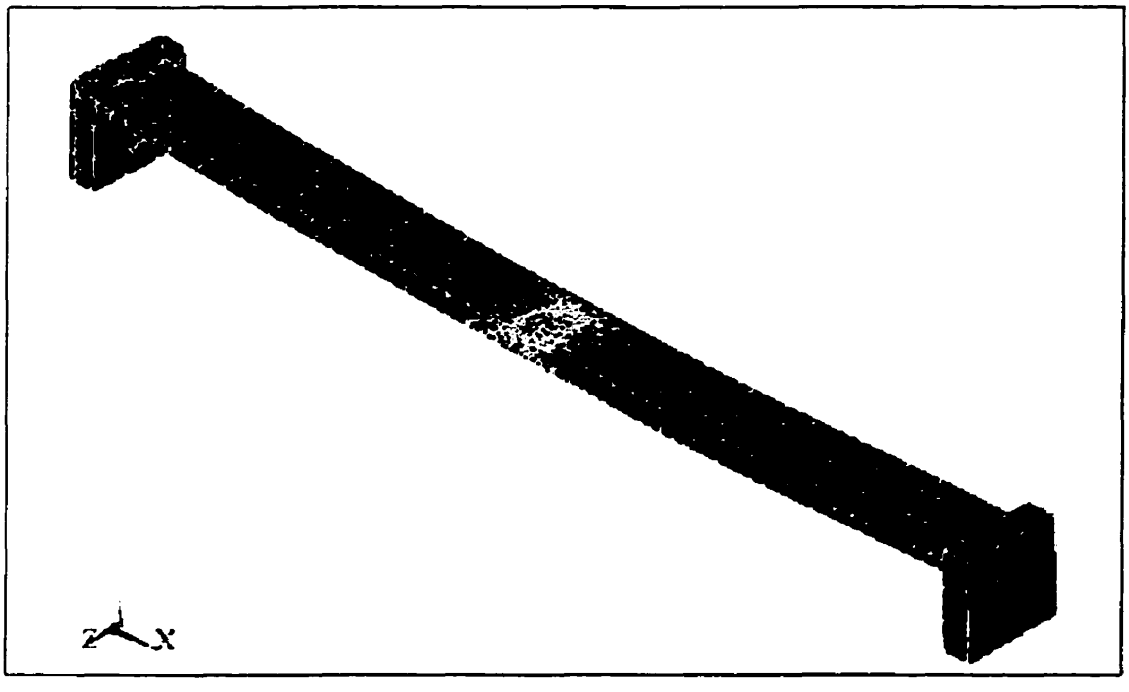

Figure A-4: The L1-OR-10CS model after failure

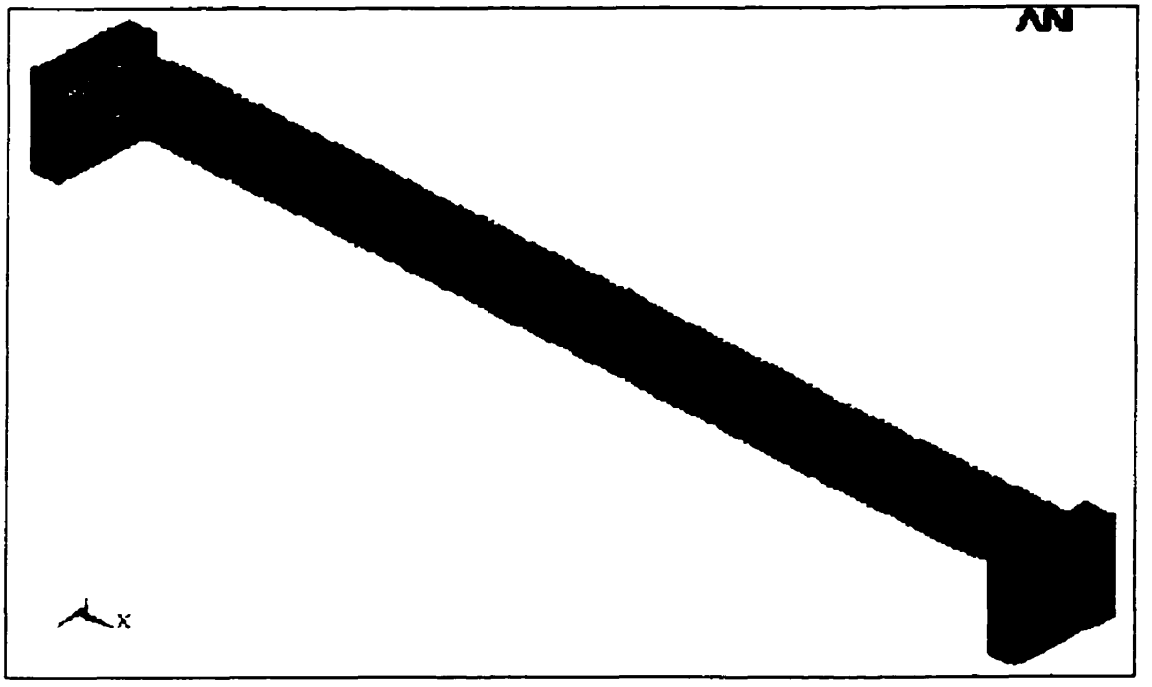

Figure A-5: The L1-EU model before failure

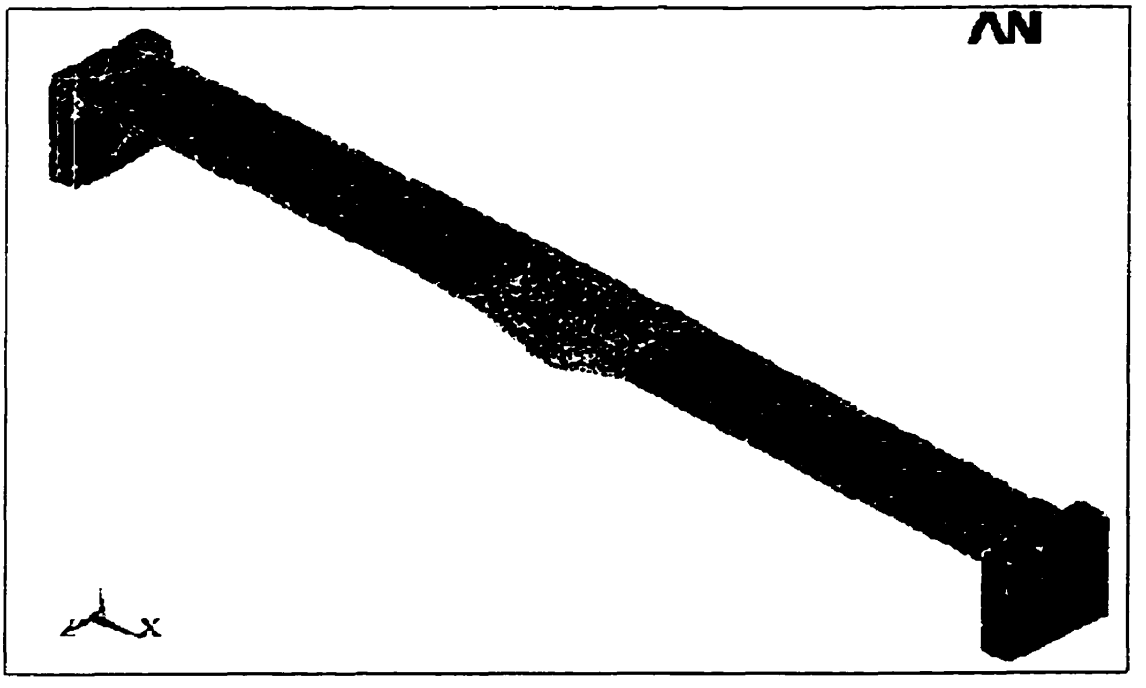

Figure A-6: The L1-EU model after failure

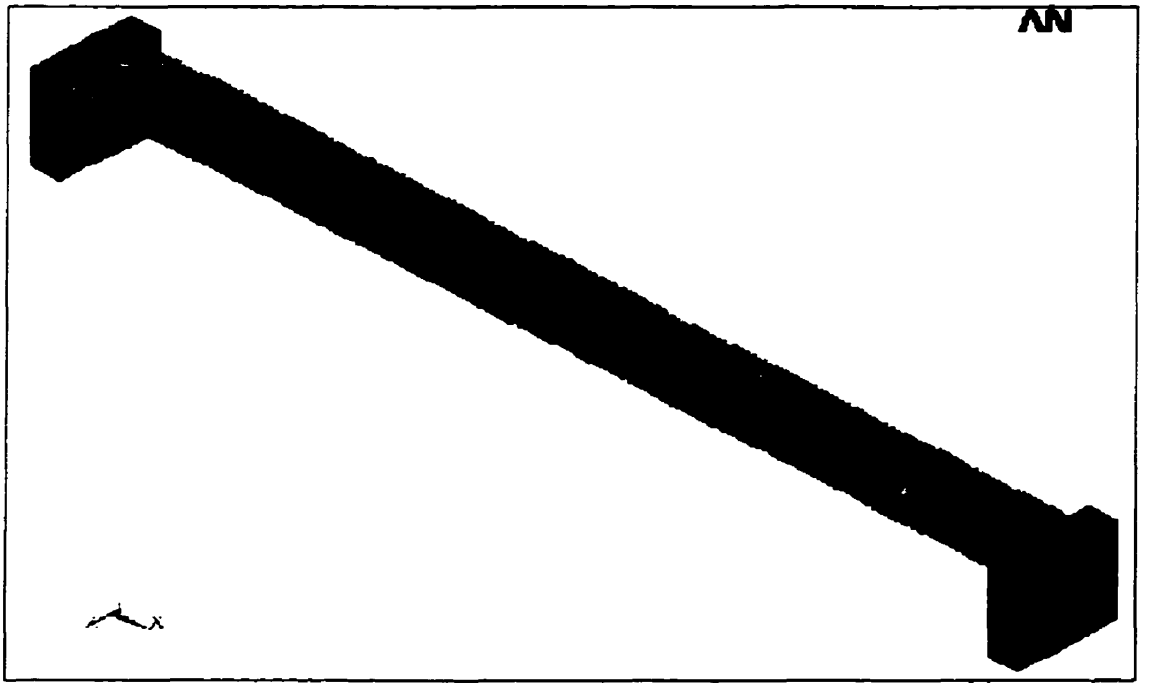

Figure A-7: The L1-ER-10CS model before failure

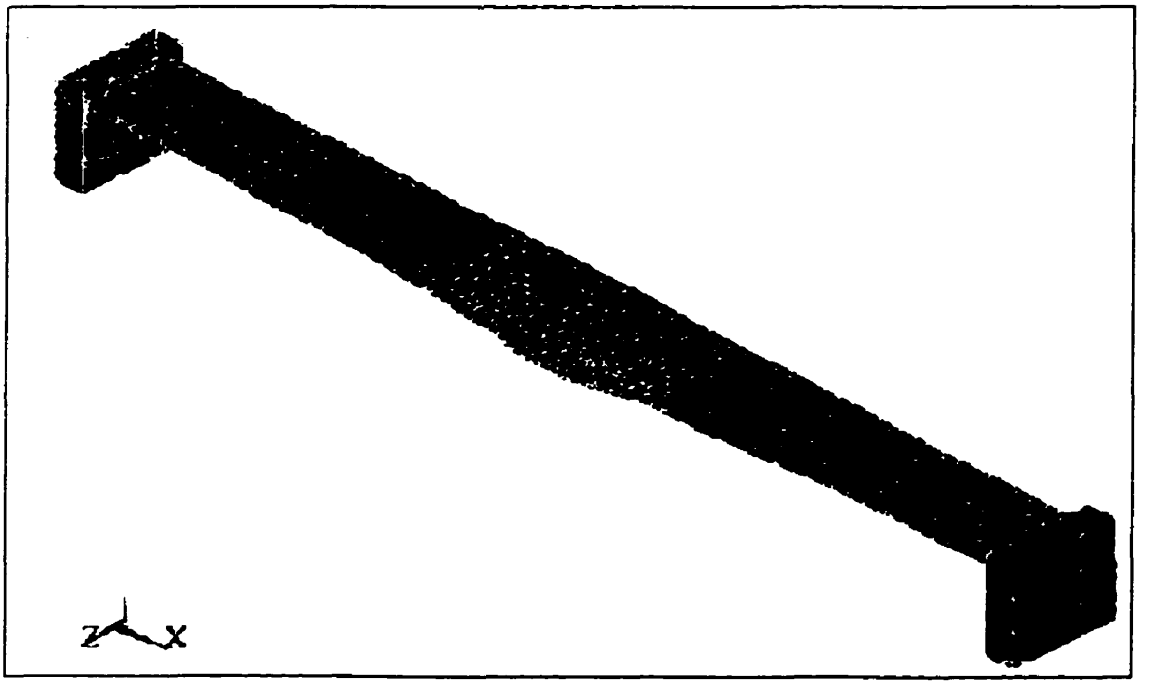

Figure A-8: The L1-ER-10CS model after failure

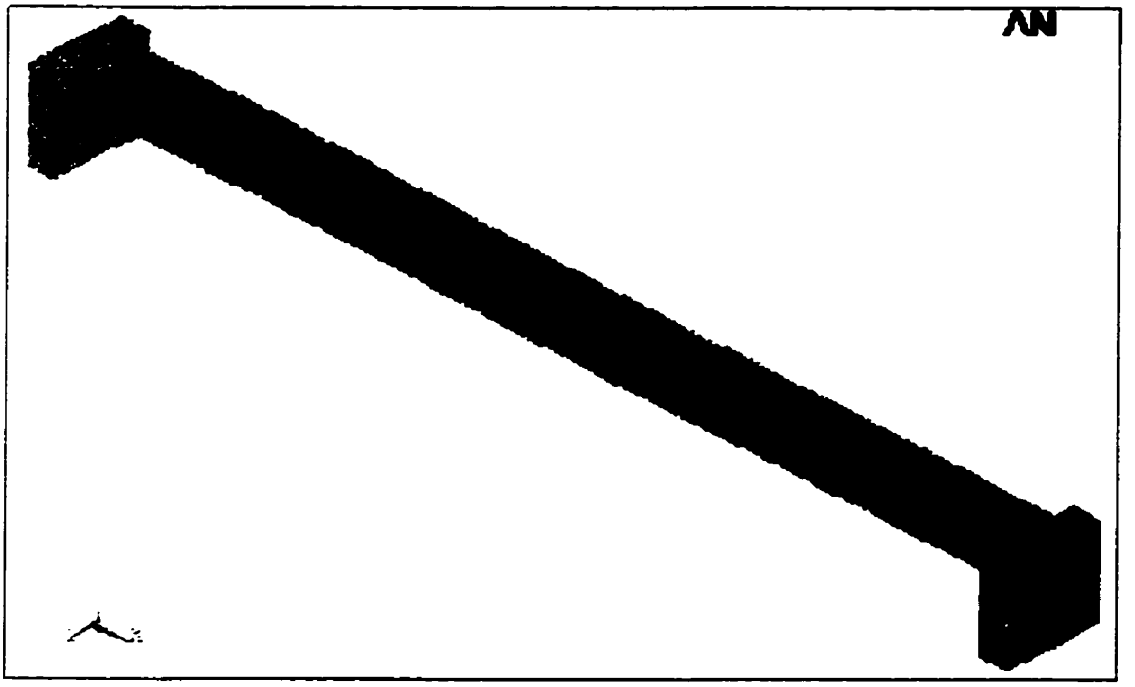

Figure A-9: The L1-EOU model before failure

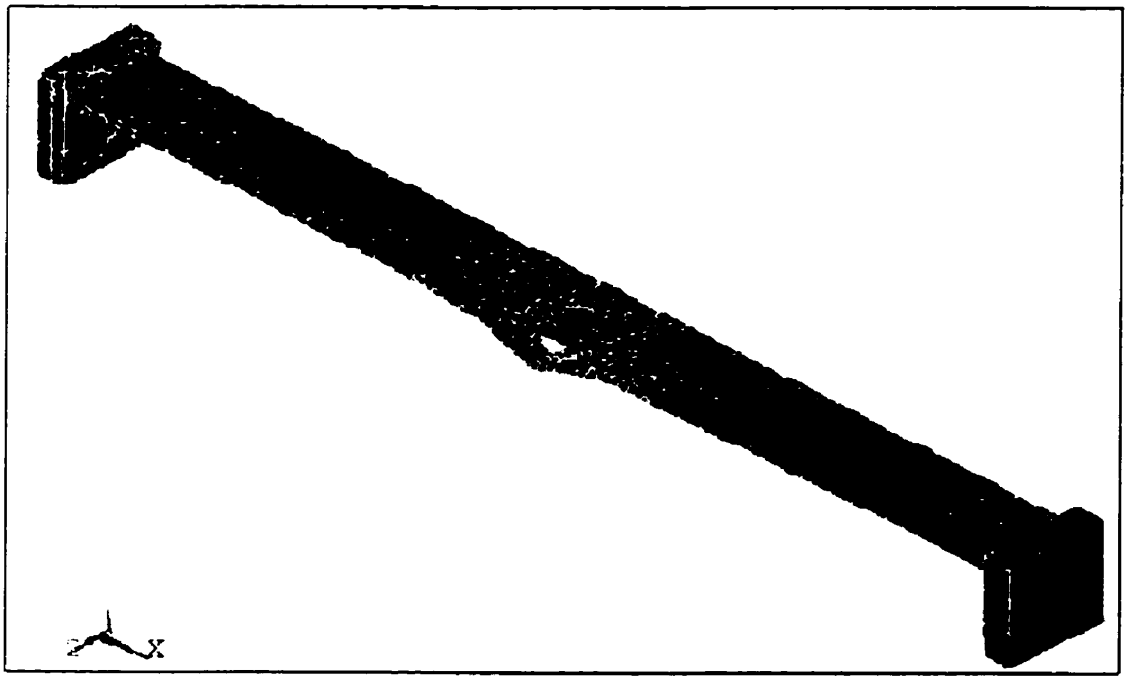

Figure A-10: The L1-EOU model after failure

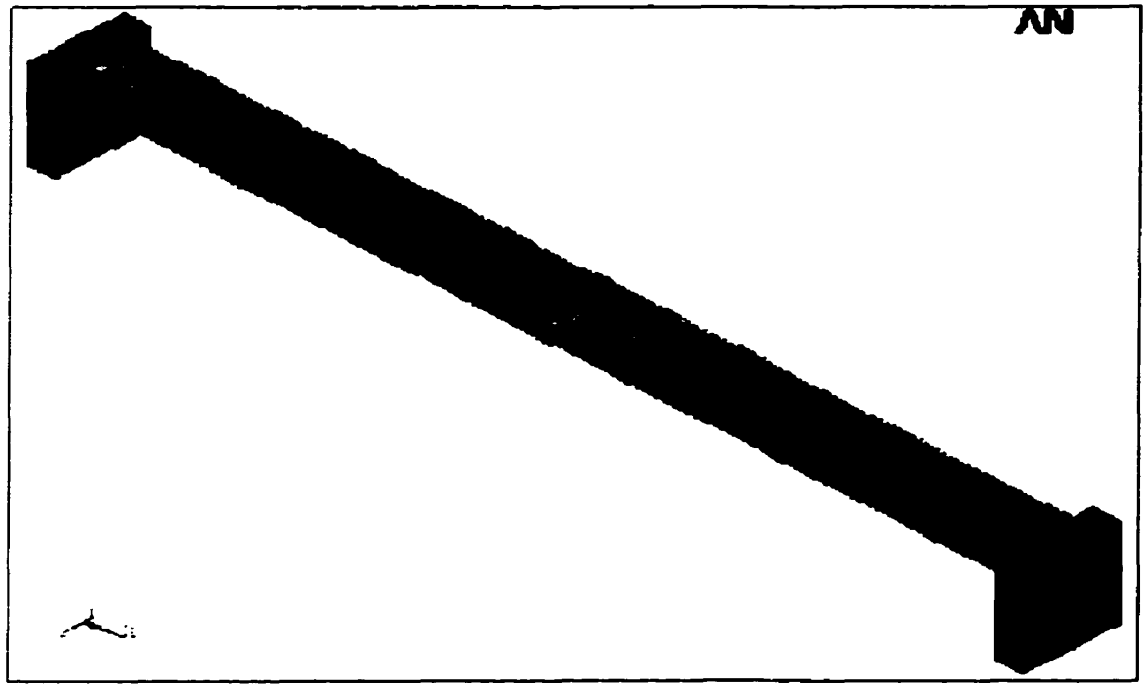

Figure A-11: The L1-EOR-10CS model before failure

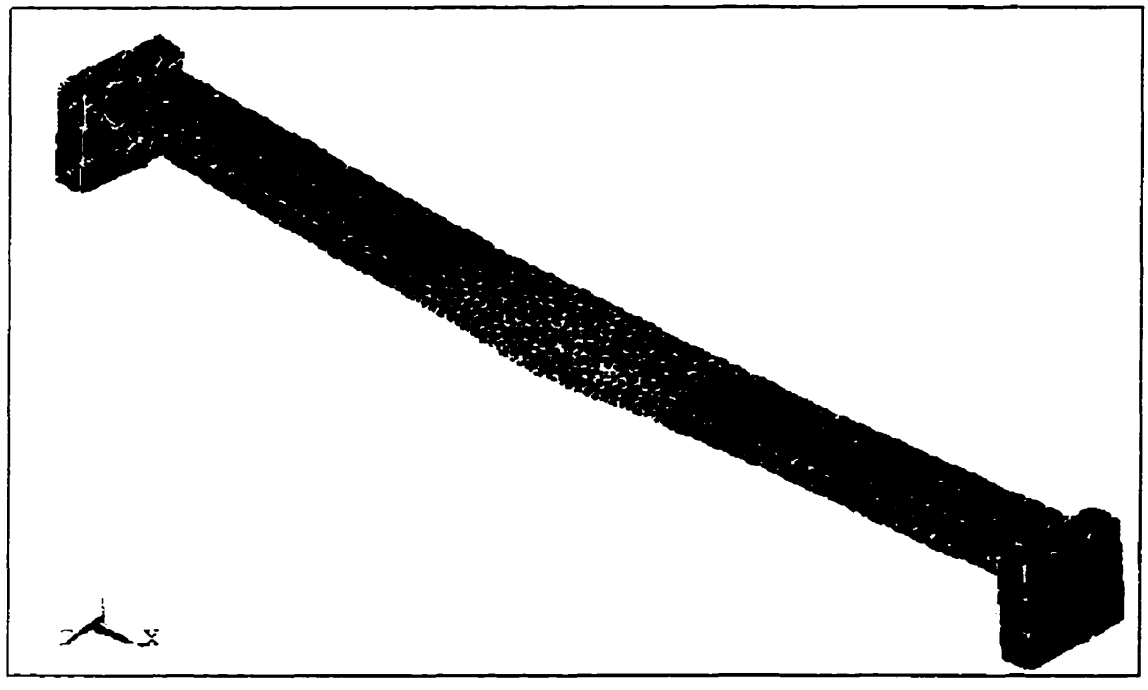

Figure A-12: The L1-EOR-10CS model after failure

REFERENCES

1. W. B. Meyer, "Metal Spraying in the United State : A JTST Historical Paper", Journal of Thermal Spray Technology, Vol. 5(1), pp. 79-83, March 1996

2. Robert H. Unger, "Thermal Spray Coatings", Metals Handbook, Vol. 13 Corrosion, 9th edition, pp. 459-462, 1987

3. Gordon England, "Nature of Thermal Spray Coatings", http://members.aol.com/getscc/tsc.htm

4. E.R. Sampson, Thermal Spray Coatings for Corrosion Protection : An Overview, Material Performance, Vol 36 n 12, Dec 1997, pp. 27-30

5. B. Towler, "Flame Deposition", Engineering Design Guides 25, Oxford University Press, pp. 1-18, 1978

6. Mr. B. Fitzsimons, "Thermal Spray Metal Coatings for Corrosion Protection", Barrier Technical News, "http://www.corrosion.com/thermal.htm", Sept 1993,

7. Charles P. Howes, Jr., "An Overview of Thermal Spray Processes", Materials Technology, vol. 11, n 5, pp. 188-194, Sept-Oct 1996

8. Elliott R. Sampson, "Thermal Spray Coatings for Corrosion Protection : An Overview", Materials Performance, vol. 36, n 12, pp. 27-30, Dec 1997

9. P. Fauchais, M. Vardelle, A. Vardelle, L. Bianchi, "Plasma spray : Study of The Coating Generation", Ceramics International, vol. 22, n 4, 1996, pp. 295-303

10. Kerri M. Howell, "Evaluating Bond Strength of Metal Coatings over Concrete Surface", Materials Performance, vol. 31, n 7, pp. 29-32, Jul 1992

11. "Standard Test Method for Adhesion or Cohesive Strength of Flame-Sprayed Coatings", ASTM Standard, pp. 150-168, 1993

12. T. A. Cruse, B. P. Johnsen, and A. Nagy, "Mechanical Properties Testing and Results for Thermal Barrier Coatings", Journal of Thermal Spray Technology, vol. 6 (1), pp. 57-66, March 1997

13. T. W. Clyne and S. C. Gill, "Residual Stresses in Thermal Spray Coatings and Their Effect on Interfacial Adhesion: A Review of Recent Work", Journal of Thermal Spray Technology, vol. 5 (4), pp. 401-418, Dec 1996

14. D. J. Greving, J. R. Shadley, and E. F. Rybicki, "Effects of Coating Thickness and Residual Stresses on the Bond Strength of ASTM C633-79 Thermal Spray Coating Test Specimens", Journal of Thermal Spray Technology, vol. 3 (4), pp. 371-378, Dec 1994

15. E. F. Rybicki, D. W. Schmueser, and J. Fox, "An Energy Release Rate Approach for Stable Crack Growth in the Free-Edge Delamination Problem", Journal of Composite Materials, vol. 11, pp. 470-487, Oct 1977

16. G. Montavon, S. Sampath, C. C. Berndt, H. Herman, and C. Coddet, "Effect of the Spray Angle on Splat Morphology During Thermal spraying", Surface & coatings Technology, vol. 91, n 1-2, pp. 107-115, May 1997

17. CSA Standard G189-1966, "Sprayed Metal Coatings for Atmospheric corrosion Protection", Canadian Standards Association, pp. 7-10, July 1966

18. H. S. Ingham and A. P. Shepard, "Flame Spray Handbook : Volume 1 - Wire Process", METCO Inc., pp. A136-A146

19. Surface Preparation Standards, http://www.corrosion.com/prep.htm, pp. 1-4

20. P. Grenon, Steel Structures Coating with Zinc Metallizing, National Association of Corrosion Engineers, Paper Number 427, March 1987, pp. 1-13

21. Karl P. Fischer, William H. Thomason, Trevor Rosbrook and Jay Murali, "Performance History of Thermal-Sprayed Aluminum Coatings in Offshore Service", Materials Performance, vol. 34, n 4, April 1995, pp. 27-35

22. Thomas F. Bernecki, George M. Nichols, David Prine, Gary Shubinsky and Alan Zdunek, "Issue Impacting Bridge Painting : An Overview", U.S. Department of Transportation Federal Highway Administration Research and Development, Chapter 5, Aug 1995

23. Anon, "Heat is on - Protecting Steel with Thermal Sprayed Zinc Coatings", Welding and Metal Fabrication", vol. 65, n 4, Apr 1997, pp. 12-13

24. F.S. Rogers, "Thermal Spray for Commercial Shipbuilding" Journal of Thermal Spray Technology, vol. 6, n 3, Sept 1997, pp. 291-293

25. Michael Hankirk and Dean S. Hansen, "Metallized Coatings for Pressure Vessel Corrosion", vol. 33, n 9, Sept 1994, pp. 31-34

26. Robert. Clarke, Andrew R. Nicoll, "Prolonged Service Life Improved Economics", Sulzer Technical Review, Vol. 77, n 2, 1995, pp. 30-33

27. U. Geurreschi, E. Rebora, and E. Gandini, "A New Technique to Repair Localised Coating Defects for Gas Turbines Blades and Vanes", American Society of Mechanical Engineers (Paper), pp. 1-10, Jun 1995

28. Eric. C. Lohrey, "Metallizing Steel Bridges in the Field", Journal of Protective Coatings & Linings, pp. 39-50, May 1995

29. John R. Birchfield, "Zinc Metallizing Protects a Bridge", Welding Design & Fabrication, Oct 1986

30. T. Mohandas, G. Madhusudan. Reddy, B. Satish. Kumar, "Heat-affected zone softening in high-strength low-alloy steels", Journal of materials Processing technology, Vol. 88, n 1, 1999, pp. 284-294

31. "Standard Test Methods for Tension Testing of Metallic Materials [Metric] (E 8M - 93)", ASTM Standard, pp. 150-168, 1993

32. "Standard Test Methods of Compression Testing of Metallic Materials at Room Temperature (E 9 - 89a) ", ASTM Standard, pp. 169-176, 1993

33. Harmer E. Davis, George Earl Troxell and George F. W. Hauck, "The Testing of Engineering Materials", By McGraw-Hill, Inc. , 4th Edition, pp. 152-161, 1982

34. "Handbook of Steel Construction", Canadian Institute of Steel Construction, 6th edition, pp. 6-80 to 6-81, Dec 1995

35. ANSYS Structural Analysis Guide, "Nonlinear Structural Analysis", ANSYS inc., Release 5.5, 3rd edition, Sept 1998, pp. 8-1 to 8-30

36. Charles G. Salmon and John E. Johnson, "Steel Structures Design and Behavior", Harper & Row, Publishers, 2nd edition, 1980, pp. 251-274